University of Alberta

Cadmium Tungstate Scintillators in Contact with Silicon Photodiodes as Detectors for Megavoltage Computed Tomography

by

Thalat Theresa Monajemi

©

A thesis submitted to the Faculty of Graduate Studies and Research in partial fulfillment of the requirement for the degree of Doctor of Philosophy

in

Medical Physics

Department of Physics

Edmonton, Alberta

Fall 2007

Library and Archives Canada

Published Heritage Branch

395 Wellington Street
Ottawa ON K1A 0N4
Canada

Bibliothèque et Archives Canada

Direction du Patrimoine de l'édition

395, rue Wellington
Ottawa ON K1A 0N4
Canada

Your file Votre référence
ISBN: 978-0-494-33032-6
Our file Notre référence
ISBN: 978-0-494-33032-6

NOTICE:
The author has granted a non-exclusive license allowing Library and Archives Canada to reproduce, publish, archive, preserve, conserve, communicate to the public by telecommunication or on the Internet, loan, distribute and sell theses worldwide, for commercial or non-commercial purposes, in microform, paper, electronic and/or any other formats.

The author retains copyright ownership and moral rights in this thesis. Neither the thesis nor substantial extracts from it may be printed or otherwise reproduced without the author's permission.

AVIS:
L'auteur a accordé une licence non exclusive permettant à la Bibliothèque et Archives Canada de reproduire, publier, archiver, sauvegarder, conserver, transmettre au public par télécommunication ou par l'Internet, prêter, distribuer et vendre des thèses partout dans le monde, à des fins commerciales ou autres, sur support microforme, papier, électronique et/ou autres formats.

L'auteur conserve la propriété du droit d'auteur et des droits moraux qui protège cette thèse. Ni la thèse ni des extraits substantiels de celle-ci ne doivent être imprimés ou autrement reproduits sans son autorisation.

In compliance with the Canadian Privacy Act some supporting forms may have been removed from this thesis.

While these forms may be included in the document page count, their removal does not represent any loss of content from the thesis.

Conformément à la loi canadienne sur la protection de la vie privée, quelques formulaires secondaires ont été enlevés de cette thèse.

Bien que ces formulaires aient inclus dans la pagination, il n'y aura aucun contenu manquant.

Canada

Abstract

The general goal was to investigate the use of segmented scintillation crystals in contact with photodiodes in megavoltage computed tomography (MVCT) for day to day patient set-up verification and tumour imaging during fractionated radiotherapy. We worked with an eighty element array of $CdWO_4$ (2.75 x 8 x 10 mm^3) in contact with photodiodes, placed on an arc with a radius of 110 cm. A rotary stage was coupled to the detector on which a phantom can be placed and rotated. The pre-sampling modulation transfer function, MTF_{pre}, was strongly affected by the large pitch of the detector. The measured detective quantum efficiency, *DQE* at zero spatial frequency was 18.8 % for 6 MV photons. The detector showed a less than 2% reduction in response for a large dose of 24.5 Gy accumulated in 2 hours. The imaging experiments were carried out mainly in a Co^{60} teletherapy unit to avoid the radiation damage to the electronics caused by the high dose per pulse in a typical clinical linear accelerator. Persistent ring artifacts, caused by air gaps at the ends of the 8-element detector blocks, were removed by using a calibration procedure. A low contrast target with a diameter of 6 mm and a nominal contrast level of 1.5% was resolved with a radiation dose of 2.1 cGy in the Co^{60} beam. The spatial resolution in the Co^{60} beam was limited to 1 line pair per cm mainly due to the size of the Co^{60} source. We also used both *x*-ray and optical photon transport Monte Carlo simulations to analyse the effects of scintillation crystal height, septa material, beam divergence and beam spectrum on the *MTF* and *DQE(0)* a theoretical area detector. Increasing the crystal height above 10 mm did not result in an improvement in the *DQE(0)* if the reflection coefficient of the septa was less than 0.8. Employing a 3.5 MV beam without a flattening filter increased the *DQE(0)* for 20 mm tall crystals by 9%

compared to a typical 6 MV beam with a flattening filter. The severe degradations due to the beam divergence on *MTF(f)* were quantified and reinforced the suggestion made by several other investigators regarding the use of focused detectors in MV imaging.

Acknowledgments

I would like to express my extreme gratitude to my supervisor, Dr. Satyapal Rathee, whose expertise, hard work, attention to detail, and patience, added considerably to my graduate experience.

I would like to thank Dr. Gino Fallone for his constant encouragement and financial assistance when it was needed the most.

I would also like to thank the other members of my committee, Dr. Ron Sloboda, Dr. Don Robinson, Dr. James Pinfold, Dr. Roger Moore for the assistance they provided at all levels of the research project.

A very special thanks goes out to the good friends I have made in the department of Medical Physics. You know who you are. My work and personal life is better because I have met you.

I would also like to thank my family: my parents, Mani, Sina and Alasdair for the support they provide me through my life. Their presence in my life is the biggest gift I could ever ask for.

Table of Contents

Chapter 1: Introduction.....1
A. Radiation Therapy and the Need for Imaging in Treatment Position.....2
B. Available Treatment Position Imaging Modalities.....3
C. History of MVCT.....9
D. Problems with MVCT.....11
E. Solution to the Problems Associated with MVCT.....13
F. History of this Project and the Structure of this Thesis.....14
G. References.....16

Chapter 2: Signal Formation in $CdWO_4$ –Si Photodiodes.....24
A. Scintillation Detectors.....24
B. Scintillation mechanism.....25
i. An Overview of the Scintillation mechanism in inorganic scintillators.....26
ii. Scintillation Mechanism in $CdWO_4$.....28
C. Relevant Properties of $CdWO_4$.....30
i. MV Photon Interactions.....30
ii. Electron Interactions.....34
iii. Optical and Mechanical Properties of $CdWO_4$.....36
D. Photodiodes.....40
E. References.....43

Chapter 3: The Bench-top System: A. Detector Characterization.....45
A. Instrumentation.....46
i. Detector Array.....47
ii. System Overview.....49
iii. Data Acquisition Timing Control (DATC).....51
B. Theory.....52
i. Linear and Shift Invariant (LSI) Systems.....52
ii. MTF_{pre}.....54
iii. *NPS*.....62
iv. *DQE*.....67
C. Materials and Methods.....67
i. Linearity.....67
a. Detector Response to Dose Rate.....67
b. Attenuation Measurement.....68
ii. MTF_{pre}.....68
iii. *NPS*.....71
iv. *DQE*.....75
v. Radiation Damage.....77
D. Results.....78
i. Linearity.....78
a. Detector Response to Dose Rate.....78
b. Attenuation Measurement.....68

ii. MTF_{pre} 80
iii. NPS 81
iv. DQE 83
v. Radiation Damage 83
E. Discussion 85
F. Conclusions 88
G. References 89

Chapter 4: The Bench-top System: B. Image Performance Evaluation 92
A. Materials and Methods 93
i. Imaging Geometry 93
ii. Phantoms 95
iii. Basic Data Processing 96
iv. Reconstruction 98
v. Scan Dose 101
vi. Artefacts 104
a. Beam Hardening 104
b. Ring Artefacts 105
c. Centre of Rotation 107
d. Incorrect Fan Beam Rotation 108
vii. Image Assessment 109
B. Results and Discussion 110
i. Data Processing and Reconstruction 110
a. Beam Hardening 110
b. Ring Artefacts 111
ii. Image Assesment 115
C. Conclusions 121
D. References 122

Chapter 5: Monte Carlo Study: Detector Design 124
A. Introduction 125
i. Imaging Characteristics of the Detector 125
ii. $MTF(f)$: Entire System 127
B. Theory 129
i. Imaging Characteristics of the Detector 129
ii. $MTF(f)$: Entire System 130
C. Materials and Methods 132
i. Imaging Characteristics of the Detector 134
a. Septa Material 134
1. Spatial Resolution 134
2. $DQE(0)$ 138
b. Beam Spectrum 139
c. Divergnece 140
ii. $MTF(f)$: Entire System 140
a. Detector Pitch 141
b. Magnification 143
c. Object Scatter 143

D. Results.....144
i. Imaging Characteristics of the Detector.....144
a. Septa Material.....144
1. Spatial Resolution.....144
2. $DQE(0)$.....148
b. Beam Spectrum.....150
c. Divergnece.....151
ii. $MTF(f)$: Entire System.....153
a. Detector Pitch.....153
b. Magnification.....155
c. Object Scatter.....158
E. Discussion.....160
i. Imaging Characteristics of the Detector.....160
ii. $MTF(f)$: Entire System.....162
F. Conclusions.....163
i. Imaging Characteristics of the Detector.....163
ii. $MTF(f)$: Entire System.....163
F. References.....164

Chapter 6: Summary and Future Directions.....167
A. References.....176

Bibliography.....178

List of Tables

Table 2.1: MV photon interaction coefficients in $CdWO_4$ at two different energies most relevant to this thesis (NIST, 2006).....32

Table 2.2: Characteristics of typical scintillators in kVCT applications (Ishii and Kobayashi, 1991).....37

Table 5.1: Properties of the surface finishes used in DETECT2000 (Levin and Moisan, 1996, Knoll *et al.*, 1988).....133

Table 5.2: Optical Swank noise factors as determined from Monte Carlo simulation.....162

List of Figures

Figure 1.1: Images of the prostate as provided by four clinical modalities; (a) kVCT, (b) MVCT, (c) kV CBCT and (d) EPID.....9

Figure 2.1: Energy band structure in scintillators with activator states (Knoll, 1989).....27

Figure 2.2: Scintillation process in intrinsic inorganic crystals (Ishii and Kobayashi, 1991).....29

Figure 2.3: Crystal structure of $CdWO_4$ (Morell *et al.*, 1980).....29

Figure 2.4: MV photon interaction coefficients in $CdWO_4$ as a function of energy (NIST, 2006).....33

Figure 2.5: Stopping power in $CdWO_4$ as a function of energy (NIST, 2006).....35

Figure 2.6: CSDA range in $CdWO_4$ as a function of energy (NIST, 2006).....36

Figure 2.7: Emission spectrum in $CdWO_4$ (Kinloch *et al.*, 2002).....39

Figure 2.8: Absorption mean free path in $CdWO_4$ (Kinloch *et al.*, 2002).....39

Figure 2.9: The Basis of Operation of Photodiodes: (a) a pn junction. (b)-(d) a photodiode operating in forward-biased, reverse-biased and short-circuited mode respectively. (e) the i-v characteristic curve of a photodiode. 42

Figure 2.10: The sensitivity spectrum of S5668-02 Hamamatsu silicon photodiodes.....43

Figure 3.1: The detector array in a typical imaging geometry.....48

Figure 3.2: Geometry of the detector array: (a) A photograph of the detector array. The 80-element array consists of ten separate bonded 8-element crystal blocks. While the spaces between neighbouring crystals on one block are filled with *gelcoat*, there are air-gaps between separate blocks. (b) Each bonded 8-element crystal block consists of crystals of size 2.75 x 8 x 10 mm^3. Two consecutive crystals are 0.4 mm apart. Each crystal is in contact with two photodiodes. The size of each photodiode is 1.175 x 2 mm^2; the spacing between two photodiodes is 0.4 mm. Each adjacent pair of photodiodes in contact with one crystal is coupled to give one signal per crystal.....49

Figure 3.3: Block diagram showing the five sub-systems and data flow of the prototype MVCT system. The detectors are arranged along an arc at a distance of 110 cm from the source, and the objects to be imaged are placed on the rotary stage.....49

Figure 3.4: The detector electronics for a single element consists of a gated integrator (C_{int} = 1 nF), an amplifier (gain = R_2/R_1) and a sample-and-hold circuit. The gain is set to 1 and 47, respectively for 6 MV and Co^{60} beams.....50

Figure 3.5: The timing diagram of the control signals: $\overline{I}$/D = Integrate-discharge control of the gated integrator; $\overline{S}$/H = sample-and-hold control; Detector Read = convert clock for the A-to-D converter. The trigger signal is either the "Sync" signal of the pulsed radiation (6 MV) or derived from an independent clock for continuous radiation (Co^{60}).....52

Figure 3.6: Steps involved in the formation of the deterministic part of the signal in a homogenous slab of a scintillator sitting atop of a 1D array of photodiodes.....56

Figure 3.7: (a) The geometry used in equations 3.9 to 3.16. (b) In equation 3.13, the nested integral over (x'', y'') represents the spatial integration of optical quanta by the $(n,m)^{th}$ photodiode element and gives the sensitivity profile of that element to a small x-ray beam being scanned across the entire element. The arrows in this figure demonstrate the concept of "a small x-ray beam being scanned across the entire detector" for one element and its surrounding septa material.....60

Figure 3.8: Finding the presampling *LSF* (c) by placing and slanted slit of beam (a) on a 2D detector and reading each row of the detector (b) (Fujita et al., 1992).....61

Figure 3.9: Schematic illustrating the arrangement of the slit beam (arrow) and the detector array for the measurement of the pre-sampling *LSF*. Here the columns represent the absolute locations of seven detector elements. The rows indicate a horizontal shift with respect to the beam. x_0 = detector pitch (3.15 mm), δ = detector translation (0.63 mm) with respect to the slit beam. The data measured at five translated positions of the detector array were interlaced to obtain the pre-sampling *LSF* with an effective sampling distance of δ.....70

Figure 3.10: The photograph shows the experimental set up for the measurement of the pre-sampling *LSF* in a 6 MV beam: the detector array (left) is translated using a linear stage, and long lead blocks (centre) are arranged to obtain the slit-beam of 0.2 mm width. Additional blocks on the right reduce the leakage radiation.....70

Figure 3.11: Plot of the attenuation of 6 MV photons by solid water as measured by detector elements 1 and 40. The straight line fit to the first four points of the detector element 1 data is extrapolated to increased thickness to indicate the amount of spectral hardening. Second order polynomials fit to all data describe the spectral hardening very well. The attenuation data for the remaining elements lies in between elements 1 and 40. The error bars on the measured data points are smaller than the symbols.....79

Figure 3.12: The pre-sampling, aperture and radiation *MTF*s of the detector array. For reference, the Nyquist frequency of the detector array is 0.16 lp/mm. The radiation *MTF* is obtained by dividing the pre-sampling *MTF* by the aperture *MTF*. The error bars on the

crystal *MTF* are larger due to the division. Radiation *MTF* –MC is calculated using Monte Carlo simulation.....80

Figure 3.13: The measured relative detector response $R(n\Delta y)$ as a function of distance of 0.4 mm slit from the center of crystals in the direction perpendicular to the array. The error bars indicate ±1 standard deviation calculated from central 8 elements.....81

Figure 3.14: Measured, normalized noise power spectrum ($NPS(u)/\bar{d}^2$) for the $CdWO_4$ array in a 6 MV beam.....82

Figure 3.15: The measured detective quantum efficiency of the $CdWO_4$ array calculated using the pre-sampling and radiation *MTFs* in 6 MV beam.....82

Figure 3.16: Mean detector signal (per unit integration period = 0.7 msec) as a function of accumulated dose to $CdWO_4$ crystals. The error bars indicate ± standard deviation (< 0.5%) of measurements conducted on four different days and reflect set up uncertainty.....84

Figure 4.1: Third generation CT scanner geometry. *SOD* is the distance from the source to the centre of rotation; X_F is curvilinear distance from centre for elements along the detector arc; φ_F is the fan beam projection angle given by the rotation of the source from the vertical position.....93

Figure 4.2: The experimental set up for imaging in Co^{60} beam. The phantoms were rotated while the γ–ray source and the detector array were held stationary.....95

Figure 4.3: The raw air scan data acquired in (a) 6 MV and (b) Co^{60}.....97

Figure 4.4: Parallel beam data collection geometry: (a) A set of line integrals at a rotation angle θ gives a projection for that angle. (b) The projected center of a pixel (x,y) as $t = x\cos\theta + y\sin\theta$ does not fall on the sampled locations of the filtered projection data $Q_\theta(t)$ in the spatial domain.....99

Figure 4.5: A radiograph of the 80 element detector array.....101

Figure 4.6: The set up for estimating the dose to the phantom: Rectangular slabs of solid water were used in this experiment. The collimators were opened to the same field size as used in the imaging geometry (FS). An ion chamber is placed at a depth of 7.5 cm; the distance from the source to the ion chamber was equal to the one used in the imaging geometry (SDD). The ion chamber reading was then recorded (D_1). The distance from the source to the ion chamber was changed to 80cm for Co^{60} and 100 cm for the linac (SAD). The ion chamber depth was kept at 7.5 cm, while the field size was set to 10 x10 cm^2 at the isocenter. The reading of the ion chamber is recorded again (D_2). For all the readings 100 monitor units were delivered in 6 MV and 2 minutes of radiation in Co^{60}.....103

Figure 4.7: An example of an image with both ring and center-of-rotation artefacts.....108

Figure 4.8: An example of an image with incorrect-fan-beam-rotation artefact.....108

Figure 4.9: The first order, α, and the second order, β, terms of the polynomial fit to the measured attenuation of 6 MV and Co^{60} beams by solid water.....111

Figure 4.10: (a,b,c) The normalized LSFs of three detectors in different locations in one block: 29 (middle of the third block), 25 (left corner of the third block), 24 (right corner of the third block); (d) The result of applying these LSFs to the simulated projections of a uniform phantom; ring artifacts similar to the experimental image (e) are observed.....113

Figure 4.11: Relative intensity profiles through the reconstructed image of the uniform phantom in 6 MV beam after applying various correction steps. Base correction includes the dark current and pulse-to-pulse variation. The beam hardening and calibration factors are described in text.....124

Figure 4.12: The dependence of SNR^2 on dose in MVCT images of the uniform phantom in Co^{60} beam. The best fit line has $R^2 = 0.9977$.....115

Figure 4.13: Images of CTP612 at four different dose levels, (a) 17cGy, (b)8.5 cGy, (c)4.3 cGy, (d)2.1 cGy. Groups A, B and C have experimental contrasts of 2.8%, 1.9% and 2.1% respectively while the cylinder in the middle has a contrast of 1.5% in Co^{60} with respect to the background material in the phantom. All images are windowed and levelled the same way.....117

Figure 4.14: The contrast of the 17cGy scan of CTP612 module is compared with the contrast obtained at more clinically viable doses of 8.5, 4.3 and 2cGy. The largest cylinder in groups A, B and C (see Figure 5.10) as well as the cylinder in the middle were used in this comparison.....118

Figure 4.15: The contrast of objects of different sizes in the CTP612 module at 17cGy. See Figure 4.13 caption for contrast levels in groups A, B and C.....119

Figure 4.16: Image of the spatial resolution phantom at 2.1cGy. The spatial resolution of the system is 1 line pair per cm in Co^{60}.....120

Figure 4.17: Image of our in-house density phantom obtained at a dose of 2.1 cGy. The CT numbers are linear with density with $R^2 = 0.9923$. The key for the arrangement of density plugs is provided in section A.ii.....120

Figure 4.18: Images through slices 6 and 7 of the Rando phantom. The center of the phantom was placed at 80cm from the source in the Co^{60} beam. The dose used to obtain these images was 2.1cGy.....121

Figure 5.1: Different system parameters which have been considered in this study for designing a cone beam MV detector. The cross-sectional view of the detector is shown as a linear segmented array as opposed to being focused on the *x*-ray source to study the effect of beam divergence.....128

Figure 5.2: The 6 MV and 3.5 MV spectra used in this study.....136

Figure 5.3: The detector geometry for studying the complete *MTF(f)*, *NPS(f)* and *DQE(f)* of the detector for a pitch of 1 mm, varying height in studying the effect of crystal height and septa: The size of each crystal is 0.85 mm x 0.85 mm x K mm. Each crystal is surrounded by 0.075 mm thick septa material on four sides. Only the crystals and septa material are modeled for the x ray energy deposition simulation study while the entire detector (crystals + septa material + optical glue + photodiodes) is simulated to study the optical photon transport properties. In DETECT2000, crystal surface except for the -z surface are GROUND (shaded) with 'Q'RC (Q = 0.975 for polystyrene and 0.65 and 0.8 for W in two separate sets of simulations). The -z surface of the crystals as well as the +z surface of the optical glue (white) are GROUND without a reflective coating. The optical glue is a sheet of size 30 mm x 30 mm x 0.075 mm. The -z surface of the optical glue which is in contact with the photodiodes (dark grey) as well as the +z surface of the photodiodes is a POLISH surface. All the other surfaces of the optical glue are METAL (light grey) 1.0RC surface; while all the other surfaces of the photodiodes are DETECT surfaces (black) with the spectral sensitivity of the photodiodes specified. Each crystal is in contact with one photodiode so that each photodiode covers the -z surface of its corresponding crystal entirely.....137

Figure 5.4: The system *LSF* is calculated as a function of detector pitch (δx). The system *LSF* is the convolution of the detector *LSF* and source *LSF* (both scaled to the object plane). The detector *LSF* is first calculated by Monte Carlo simulation of energy deposition in the $CdWO_4$ scintillation crystal for a 6 MV pencil beam using a very small detector pitch (0.01 mm) in x-direction and averaging along y-direction. The focal spot *LSF* is assumed to be a Gaussian function with FWHM of 2 mm. The system *LSF* calculated for δx = 0.01 mm was converted to larger detector pitches of 0.5, 0.7 and 1.0 mm by using the moving average of appropriate number of points.....142

Figure 5.5: The LSF_{sys} is calculated as a function of patient thickness, D. The LSF_{sys} is the convolution of the detector *LSF* and the source *LSF* (both scaled to the object plane). The detector *LSF* is first calculated by Monte Carlo simulation of energy deposition in the $CdWO_4$ scintillation crystal for a 6 MV pencil beam using a very small detector pitch (0.01 mm). The *source LSF* is assumed to be Gaussian function with a FWHM of 2 mm. D=20 and 40 cm. The system *LSF* calculated for δx = 0.01 mm was then re-sampled to larger detector pitch of 1.0 mm.....144

Figure 5.6: LSF of the detector as obtained by the results of energy deposition in DOSXYZnrc for W and polystyrene as the septa material.....145

Figure 5.7: The presampling MTF(f) of the detector for different septa wall material, reflection coefficient and height configurations.....147

Figure 5.8: The DQE(0) for two different fill factors. The effect of optical photons are ignored. The septa material for fill factor of 72% is assumed to be air.....148

Figure 5.9: The DQE(0) of the detector for different septa wall material, reflection coefficient and height configurations.....149

Figure 5.10: The *MTF(f)* of 20 mm tall crystal with polystyrene septa in both 6 MV and 3.5 MV beams shown in Figure 5.2.....150

Figure 5.11: The effect of beam divergence on the *LSF* of the detector. In (a) and (b), an ideal optical photon transport is considered. In (c) and (d) the optical photon transport is considered for different crystal heights and polystyrene septa.....152

Figure 5.12: The effect of beam divergence on the presampling *MTF* of the detector. Polystyrene is the septa material.....153

Figure 5.13: The *MTF(f)* of detector, and the overall system *MTF(f)*. *(a):* Detector *MTF(f)* in the object plane: 1 cm height; pitches = 0.01, 0.5, 0.7 and 1 mm; no optical transport. *(b)*: The system *MTF(f)* in the object plane with a magnification of 1.4 155

Figure 5.14: The effect of increasing the system magnification (M) on the overall system $MTF(f)$ for a realistic focal spot sizes of Gaussian shape with FWHMs of 1 mm and 2 mm with ideal optical photon transport. Crystal height = 1 cm, pitch = 1 mm.....157

Figure 5.15: The effect of the object scatter and system magnification (M) on the overall system *MTF(f)*. D = phantom thickness and pitch = 1mm. The two extra curves in (a) were obtained using 1 mm thick Cu plate on top of the crystal.....159

Figure 6.1: The imaging geometry for MVCBCT investigation. Side view shows the multi-row detector at z = 0 (bolded) and several other z-locations.....172

Figure 6.2: Photograph of 4 photo-diode arrays tiled together. Each photo-diode is a 16 x 16 array with a pixel pitch of 1 mm.....174

Figure 6.3: Block diagram of the proposed system of cone beam data collection and image reconstruction. The detector system and analogic DAS are inside and rest of the hardware outside the treatment room.....174

List of Abbreviations

2DFT.....two dimensional Fourier transform
AED.....absorbed energy distribution
BEV.....beam's eye view
CBCT.....cone beam computed tomography
CR.....computed radiography
CSDA.....continuous slowing down approximation
CT.....computed tomography
DATC.....data acquisition and timing control
DQE.....detective quantum efficiency
DVH.....dose volume histogram
EC-L.....enhanced contrast-localization
EGSnrc.....Electron Gamma Shower (a Monte Carlo Radiation Transport Code), version developed by NRC (National Research Council of Canada)
EPID.....electronic portal imaging device
IMRT.....intensity-modulated radiotherapy
irf.....impulse response function
KV.....kilovoltage
KVCT.....kilovoltage computed tomography
LCR.....low contrast resolution
LSF.....line spread function
MTF.....modulation transfer function
MTF_{pre}.....presampling modulation transfer function
MV.....megavoltage
MVCT.....megavoltage computed tomography
NPS.....noise power spectrum
PMT.....photomultiplier tube
PSF.....point spread function
SNR.....signal to noise ratio
SOD.....source to object distance
WSS.....wide sense stationary

Chapter 1

Introduction

The goal of localization imaging is to ensure correct and precise positioning of a patient with respect to treatment beam(s) during multiple fractions of radiation delivered over several weeks. Megavoltage computed tomography (MVCT) uses the same *x*-ray beam generation system as used for treatment to provide a 3D image of the patient. The first reported MVCT scanner was developed in 1982 at the University of Arizona (Simpson *et al.*, 1982). Since MVCT systems have some clear advantages – as discussed below - over other methods of providing 3D images of patients in the treatment position, and extensive research effort has been devoted to the development of MVCT scanners (e.g. Morton *et al.*, 1991, Nakagawa *et al.*, 1992, Midgely *et al.*, 1998, Mosleh-Shirazi *et al.*, 1998, Ruchala *et al.*, 1999, Ford *et al.*, 2002, Seppi *et al.*, 2003, Poliot *et al.*, 2005, Monajemi *et al.*, 2006). However, to this date, only one commercial MVCT system (Hi-Art II, TomoTherapy Inc., Madison, Wisconsin) is available because the task of imaging patients using a MVCT beam is complicated due to the high energy of photons produced by therapy beam generation systems. We had two main objectives in pursuing this project. The first objective was to test the performance of cadmium tungstate, $CdWO_4$, scintillation crystals in contact with photodiodes in MV imaging. The design and construction of the detector was the topic of another student's thesis (Tu, 2005) in our laboratory. The second objective of this project was to study the effect of different system parameters on the imaging performance of a scintillator based MVCT scanner, and to suggest an optimal scanner design for such detectors based on these parameters.

This chapter provides the reader with a general background on the subject of MVCT. The need for imaging in radiotherapy, different treatment localization and verification imaging modalities currently available, advantages and disadvantages of MVCT in comparison with other modalities, a brief history of MVCT, problems associated with MVCT, and finally an overview of the structure of this thesis are discussed.

A. Radiation Therapy and the Need for Imaging in Treatment Position

The ultimate goal of radiotherapy is to deliver a large (~50-70 Gy of total dose) and homogeneous dose to a tumor while minimizing the dose to the surrounding normal tissue (Suit, 1992). In the conventional method of delivering radiation, the jaws on a treatment unit are opened to a rectangular shape and a nearly uniform beam is delivered in this manner. In order to achieve further conformation to the tumour shape, conformal radiotherapy and intensity modulated radiotherapy (IMRT) have been developed (Suit, 1992).

The object of conformal radiotherapy planning is to determine, in an iterative trial and error manner (forward planning), the optimal combination of beam angles, shapes, weights and modifying devices that provide optimal tumor coverage and normal tissue sparing. Planning for conformal radiotherapy usually involves the use of a beam's eye view (BEV) display of the patient - depicting the treatment beam projections of the tumor and critical organs as outlined in diagnostic CT images of the patient- and calculation of 3D dose distributions and cumulative dose volume histograms (DVH) (Pirzkall *et al.*, 2000).

IMRT is a more specific application of conformal radiotherapy where the intensity (in addition to the change in the shape of the beam which is the hallmark of conformal radiotherapy) of the delivered beam is modified to achieve tumor dose homogeneity and normal tissue sparing (Pirzkall *et al.*, 2000), especially when a critical organ is located close to a concave shaped tumor. The simplest form of IMRT involves finding a limited number of shaped fields by forward planning, where each field consists of several subfields which have different shapes but uniform intensities (DeNeve *et al.*, 1996, Eisbruch *et al.*,

1998). In its most complex form IMRT involves the use of hundreds to thousands of small fields, each with different intensities; the overall pattern of the treatment field is defined with inverse planning (Pirzkall *et al.*, 2000). Inverse planning involves finding the combination of treatment beam shapes and intensities by first defining the desired 3D dose distribution (Spirou and Chui, 1998).There are two general ways of delivering IMRT: (1) Fixed field IMRT (Siochi, 1999, Stein *et al.*, 1994) involves the use of computer driven multi leaf collimators (MLCs) in a static or dynamic manner. In static fixed field IMRT delivery, a total of 4-9 planar or non-coplanar fields are delivered each containing their own subfields and the beam is turned off between the subfields. In dynamic IMRT delivery, the shape of a particular fixed field is modified continuously by the moving MLC while the radiation is on; radiation is turned off while the selection of the orientation of next fixed field in the set is made. (2) IMRT can also be delivered on a slice by slice basis by using special binary MLCs (leaves of a binary MLC can be placed swiftly in and out of the beam) and rotating the beam around the patient in a serial (Carol *et al.*, 1995) or helical (Mackie et al. 1993, Olivera *et al.*, 1999) manner. Currently, fixed IMRT delivery is more prevalent since it is implemented using conventional medical accelerators mounted on an isocentric C-arm gantry.

Whatever the method of delivering radiation may be, by definition conformal radiotherapy and especially IMRT contain high dose gradients at the periphery of the tumor, and thus the accurate and precise positioning of the patient is extremely important. For the purpose of radiotherapy planning, patients are imaged using CT and other imaging modalities prior to the treatment planning process to localize the tumor and critical organs. While these image volumes are used for initial positioning of the patient, positioning errors may arise during the 4-5 week duration of treatment (Hong *et al.*, 2005, Xing *et al.*, 2000). Localization imaging refers to taking images of the patients immediately prior to each treatment so that adjustments to the patient set up can be made if an error in patient position with respect to the collimated beam is indicated. Verification imaging refers to imaging of patients during their treatment so that the treatment can be assessed once it is done and necessary changes to the remaining

treatment sessions can be made accordingly (Antonuk, 2002). In addition to errors in positioning patients, the size and shape of the tumor can change especially if the treatment is delivered in multiple fractions which typically extend over several weeks. Tomographic imaging methods including an optimally designed MVCT, in general, can successfully address the day-to-day changes in patient position and/or changes in tumour volume; however, the position of the tumor within the patient may change during a single fraction due to factors such as breathing. Respiratory motion significantly alters the position of thoracic and abdominal tumours such as in lung and liver (Balter *et al.*, 1996). Even the prostate has been shown to move, more in the prone position than in the supine position due to breathing (Dawson *et al.*, 2000). Real-time imaging with excellent soft-tissue contrast is required to track the tumor shape and position during a fraction (i.e. intra-fraction) or radio-opaque markers that are visible in fluoroscopic images can be used (Rietzel et al., 2004). It should be noted that the issue of real-time imaging for the purpose of intra-fraction tumor tracking is not addressed in this work.

B. Available Treatment Position Imaging Modalities

Historically, imaging in treatment position has been done by using film cassettes that record a megavoltage (MV) projection radiograph of the patient using the treatment beam portal. Thus, this technique is termed as portal imaging. Film cassettes consist of a piece of film sandwiched between a front metal plate and a plastic or metal plate in the back. The front plate converts the high energy radiation to electrons which are more readily absorbed by the film. In addition, the front plate reduces the lower energy scattered radiation produced in the patient. The back plate serves as back scatter material and holds the film in place (Antonuk, 2002). Localization films are used immediately prior to each treatment fraction for the purpose of positioning patients properly. Verification films are used during each treatment fraction such that if an error in positioning the patient is found, it can be compensated for in the upcoming fractions. Localization films require less dose than verification films and therefore are more

sensitive to radiation. Newer versions of film cassettes -enhanced contrast localization (EC-L) systems- employ a fine grain film sandwiched between two phosphor screens with a 1 mm metal front plate. The presence of the phosphor screens increases x-rays detection efficiency by a factor of 2 (Munro et al., 1999). Due to the very fine grain the images are less noisy compared with traditional film cassettes; they also have better contrast resolution properties. Some advantages of films as MV imagers include the fact that they are compact, light weight and easy to handle. However, the process of developing films is time consuming and labour intensive. In addition, films have a limited dynamic range over which they are neither over nor under exposed. (Antonuk, 2002) and film images are less likely to be enhanced using digital image processing techniques.

Computed radiography (CR) is another projection imaging system; this technique employs photostimulable phosphors or storage phosphors (Sonoda et al., 1983). These phosphors are powders which are deposited on a substrate to form the imaging plate. The x-ray energy deposition process in CR plates is identical to conventional film screen and cassettes with the exception that in photostimulable phosphors, energy deposition creates trapped meta-stable charges instead of optical photons immediately following irradiation. Optical photons in the range of blue wavelength are created later on during excitation when the phosphor is read out by raster scanning with a laser. The blue light is collected with a light guide and sent to photomultiplier tubes (PMTs). The PMT signal is digitized on a point by point basis (Fujita et al, 1989). CR plates have a digital nature; they are easy to use and have a higher dynamic range than film cassettes and image enhancement can be performed using digital imaging processing techniques. Even though current CR systems are practical and flexible, they are not optimized for image quality in megavoltage range. The best photostimulable phosphor thus far, $BaFX:Eu^{2+}$, has an atomic number and density lower than conventional phosphors and a gain lower than theoretically possible. (Rowlands, 2002).

Electronic portal imaging devices (EPIDs) are electronic alternatives to portal films. In general, these systems use a radiation detector and an electronic

read out system for the detector that spatially encodes and digitizes the detector signal. Unlike film and cassettes or CR plates, most EPIDs are more mechanically cumbersome systems; and therefore, are typically attached to the gantry of the treatment unit. However, some EPIDs can be easily removed or retracted when they are not in use. Three kinds of EPIDs have been used: matrix ion chamber, a phosphor screen read by a TV camera and a phosphor screen read by an active matrix (flat panel EPID) of amorphous silicon photodiodes (Munro, 1998); most modern medical linear accelerators are equipped with flat panel EPIDs. EPIDs offer the advantages that their images are quick to view and can be enhanced by image processing techniques. Therefore, EPIDs have replaced the screen-film based portal imaging (Stroom *et al.*, 2000, Mubata *et al.*, 1998, Alasti *et al.*, 2001). EPIDs have been used to automatically correct the patient set up by using a "tilt and roll" couch (Hornick *et al.*, 1998).

Despite the fact that 2D projection images from state-of-the art flat panel EPIDs are now widely popular, they have an inherent flaw in that they superimpose the anatomical structures on top of each other (figure 1.1). There is no volume information so that a comparison between planning volume of interest can be compared to same volumes at the time of treatment. To provide similar anatomical information to that obtained in the EPID images, a divergent set of rays are traced through the 3D set of planning CT images of a patient and the attenuation coefficients along each ray are integrated to create digitally reconstructed radiographs (DRRs); these DRRs are then compared with the EPID images to deduce any anatomical changes or set up errors (Goitein *et al.*, 1983, Sherouse *et al.*, 1990). However, when discrepancies between EPID images and DRRs occur, it generally becomes difficult to determine the axes about which the patient has translated or rotated. This is especially true for the rotations that may have occurred out of the plane of projection of a particular beam direction (Balter *et al.*, 1993, Van de Steene *et al.*, 1998, Remeijer *et al.*, 2000). Some groups place radio-opaque markers in organs like the prostate to obtain reference points in EPID images (Vigneault *et al.*, 1997, Bergstrom *et al.*, 1998, Pang *et al.*, 2002); but this procedure is undesirable since it is highly

invasive. A better modality should offer 3D images of patients with reasonable soft-tissue contrast in treatment position.

Ultrasound is a 3D imaging technique which has been used to visulalize patient anatomy at the time of treatment (Lattanzi *et al.*, 1999). Ultrasound image can be compared with planning CT images to examine patients' treatment set up. Ultrasound has been used to determine the position of prostate immediately prior to treatment (Van den Heuval *et al.*, 2003). Although in principal it can also be applied to other (abdominal) disease sites; ultrasound has limited penetration through fat, bone and lung tissues (Mackie *et al.*, 2003) in addition to an inherently inferior imaging quality. Recently, a 3D ultrasound system has been introduced that images the patient both at the time of planning CT imaging and treatment in order to reproducibly position the prostate in treatment beam (RESTITU™, Resonant Medical, Quebec).

Another more conventional (and potentially more useful) 3D treatment position imaging tool is CT. The combination of a linear accelerator and a diagnostic CT scanner, in a single suite, was used by Kuriyama *et al.* in 2003 to provide kilovoltage (kV) CT images in treatment position. This group placed a diagnostic CT scanner on rails where the patient couch is rotated by a half turn between CT imaging and treatment. While the image quality of a diagnostic CT scanner is unparalleled (problems with MVCT are discussed below), this system does incur a much higher cost due to the larger treatment room as well as purchase and regular maintenance of a diagnostic CT scanner.

Cone beam kVCT scanners have been implemented on the gantry of a linear accelerator (Jaffray *et al.*, 2002). An x-ray tube is mounted on the C-arm of the linear accelerator at 90° angle with respect to the treatment beam, and an area detector comprised of an active matrix flat panel array is mounted opposite to the x-ray tube. The x-ray tube and the area detector are slowly rotated around the patient using the iso-centric motion of the linear accelerator to collect cone beam projections of the patient. The image quality of kV cone beam CT (kV CBCT) has been shown to be adequate for the purpose of patient position verification; however, this system requires an x-ray tube and an additional flat

panel imager. In addition, cone beam kVCT scanners are known to show significant scatter artefacts due to the large scatter angles in the kV energy range (Kwan *et al.*, 2005, Ning *et al.*, 2004, Endo et al., 2001) and artefacts due to respiratory motion in thoracic and abdominal imaging studies (Sonke *et al.*, 2005).

The use of a megavoltage beam either in fan beam (Simpson *et al.*, 1982, Swindell *et al.*, 1983, Lewis *et al.*, 1992, Nakagawa *et al.*, 1992, Ruchala *et al.*, 1999) or cone beam (Mosleh-Shirazi *et al.*, 1998, Ford *et al.*, 1992, Midgely *et al.*, 1998,Guan *et al.*, 1998, Hesse *et al.*, 1998, Seppi *et al.*, 2003, Groh *et al.* 2002, Pouliot *et al.*, 2005, Morin *et al.*, 2006) configuration are present examples of implementing MV 3D CT imaging in treatment position. Although –as discussed below - a megavoltage cone beam CT (MV CBCT) has relatively poor image quality and uses a relatively larger radiation dose, it is a simple and inexpensive solution for CT imaging in the treatment position. MVCT uses the same beam generation system as that used for treatment. The detector system used for MVCT can also be utilized for portal imaging and dose reconstruction (Partridge *et al.,* 2002). MVCT images do not suffer from artefacts due to metallic objects found in dental fillings, prosthesis and brachytherapy applicators, although post processing techniques have been developed to reduce the metallic artefacts in kVCT (Yazdia *et al.*, 2005). The reason for less pronounced metal artefacts in MV images as compared to kV is that Compton interactions, which are highly dependent on the electron density, dominate over photoelectric absorption, which is highly dependent on atomic number, in the MV energy range. Treatment planning systems use the 3D distribution of electron density of the patients to accurately calculate the radiation dose distribution. MVCT numbers are linearly related to electron density, due to the dominance of Compton interactions- (Ruchala *et al.*, 2000), whereas kVCT numbers deviate from a single linear curve for high atomic number objects, due to the presence of both Compton and photoelectric interactions. Although a piecewise linear curve is generally used for kVCT calibration (Constantinou *et al.* , 1992) to partially compensate for this

behaviour, the dense bone kVCT numbers can vary up to 6.4% depending on the location and the size of the phantom used (Ruchala *et al.*, 2000).

For the sake of comparison, typical images acquired from a diagnostic kVCT, MVCT, kV cone beam CT and EPID shot of a prostate are shown in figure 1.1. It is obvious that 2D EPID images lack the anatomical information provided in the tomographic images. The kV CBCT images show significant streak artefact due to abdominal motion and darkening in anterior side due to scattered radiation; MVCT images are characterized by poorer contrast compared to both diagnostic kVCT and kV CBCT images while the best image is offered by diagnostic kVCT.

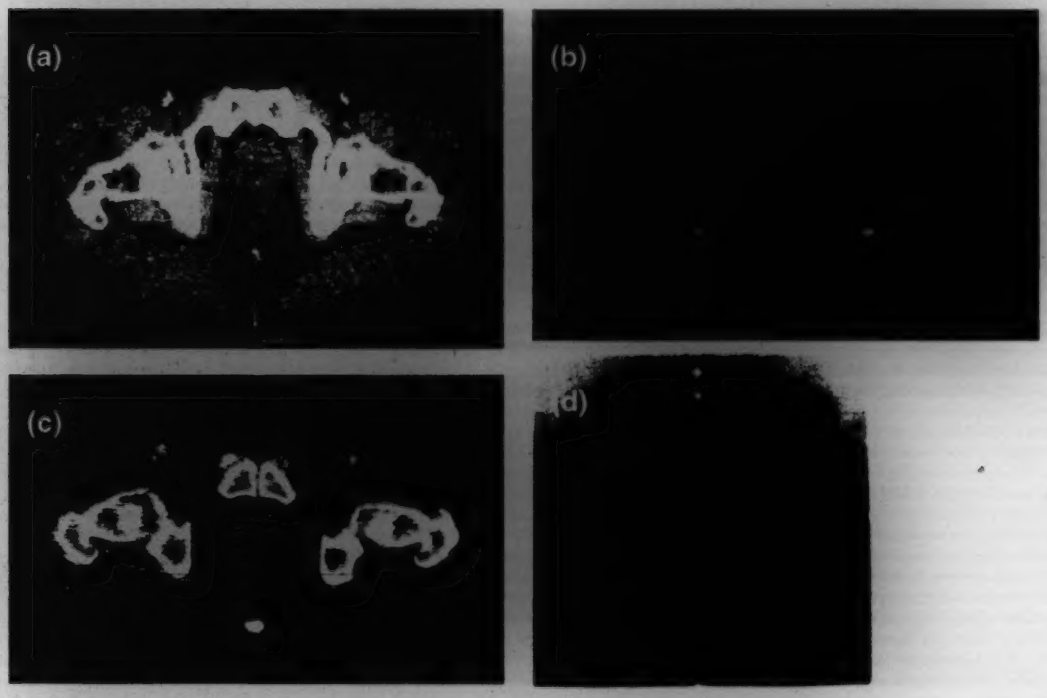

Figure 1.1: Images of the prostate as provided by four clinical modalities; (a) kVCT, (b) MVCT, (c) kV CBCT and (d) EPID.

C. History of MVCT

Fan beam MVCT was first studied by Simpson *et al.* (1982) using plastic scintillation detectors and a 4 MV beam from a linear accelerator. The estimated

signal to noise ratio (SNR) of 100 was obtained in the CT image using an image forming dose of 12 cGy; however, a direct measurement of low contrast resolution (LCR) was not provided. Modification to this system was reported by Swindell *et al.* (1983) using thick BGO scintillators. The authors reported that a large circular disc with an electron density difference of 1% from the background was visible in the images obtained using a 4 MV beam at 10 cGy. Lewis *et al.* (1992) used a similar system and obtained 5% LCR with a radiation dose of 1 cGy in a 6 MV beam. Brahme *et al.* (1987) built a test system consisting of a single 5 mm tall BGO detector mounted on the axis of a stationary elementary bremsstrahlung beam. The objects were translated and rotated instead of moving the beam and the detector. The mean energy of the photon beam used was 20 MeV. The authors reported that they provide the first tomographic images of a thorax phantom with contrast level comparable to that of 300 kV *x*-rays mainly because of the considerable influence of pair production. Nakagawa *et al.* (1992) used 5 mm thick $CdWO_4$ crystals in fan beam geometry, and reconstructed MVCT images using 4 MV and 6 MV beams. The estimated doses delivered per scan in 4 MV and 6 MV beams were 1.4 cGy and 2.8 cGy respectively; however, a direct measurement of the dose delivered in MVCT experiments was not reported. Moreover, a polystyrene pin of -41 Hounsefield Unit* was not visible in the images amounting to a poorer than 4.1% LCR. Ruchala *et al.* (1999) used a xenon gas detector in fan beam geometry and a 4 MV Orion linear accelerator. Using this system, large circular discs of 2% LCR were visible in images obtained using a radiation dose of 8 cGy. Other investigators (Guan *et al.*, 1998, Hesse *et al.*, 1998) have used commercially available EPIDs and fan beam collimation (1 cm x 25 cm) with 6 MV photon beams to obtain CT images. The radiation dose in these investigations is larger than 50 cGy and hence compromises the utility of such an approach.

Several investigators have used commercially available EPIDs to reconstruct MV CBCT images. Midgley *et al.* (1998) used liquid filled ionization chamber EPID in a 6 MV photon beam to obtain CT images showing 4% LCR at

---

* Hounsefield Unit = 1000 (Tissue Attenuation – Water Attenuation)/Water Attenuation

a radiation dose of 90 cGy. An active matrix flat panel imager (aS500, Varian Medical Systems, Palo Alto, CA) was used to obtain cone beam projection data in a 6 MV photon beam by Ford *et al.* (1992). The CT images produced a LCR of 2% using a very high image dose of 200 cGy. Groh *et al.* (2002) used another flat panel imager (RID 256-L, PerkinElmer Optoelectronics) and obtained LCR of 5% and 2% respectively using 6 cGy and 32 cGy per scan. Mosleh-Shirazi *et al.* (1998) used a video based MV CBCT/portal imaging system using an array of optically isolated 3 mm x 3 mm x 10 mm CsI(Tl) crystals and a CCD camera. The CT images obtained with this system showed a LCR of 2% using a radiation dose of 40 cGy. A very high resolution flat panel imager (PaxScan 4030A, Varian Medical Systems, Palo Alto, CA) was also used in contact with an array of optically isolated 0.38 mm x 0.38 mm x 8 mm CsI (Tl) scintillator (Seppi *et al.*, 2003) in an attempt to build a combined MV CBCT and EPID. This system provided CT images with an *estimated* LCR of 1% using a radiation dose of 16 cGy. More recently a high resolution PerkinElmer flat panel imager was used in the cone beam geometry by Pouliot *et al.* (2005) These investigators used a linac dose per pulse control mechanism that allowed cone beam projection data to be collected using radiation dose ranging from 5 cGy to 15 cGy; however, basic performance metrics such as LCR and SNR using the standard phantoms were not reported. The same system was modified further to give images of the prostate with 7 cGy (Morin et al., 2006).

D. Problems with MVCT

The problems associated with MVCT are not specific to this modality but extend to all megavoltage imaging techniques. The root of the problems is that one is trying to image patients with a photon beam which is optimized for treating tumors and not imaging them, as opposed to the case with a diagnostic imaging beam.

Generally MV images suffer from poor low contrast and limited spatial resolution. At kV photon energies, a small fraction (<10%) of photons interacts through the photoelectric process in the soft tissue. The photoelectric cross section in a material depends approximately on the fourth power of its atomic

3number; therefore, despite very small differences in atomic numbers of soft tissue components, some enhancement in soft tissue contrast does occur. At MV energies, photons interact mainly through Compton interactions; Compton interaction in a material depends only on the electron density. Soft tissue contrast also depends on the absolute value of the linear attenuation coefficient of the materials. Although, the ratio of the Compton fraction of linear attenuation coefficients for two materials should be approximately constant from kV to MV energies (Ruchala *et al.,* 1999), the absolute difference among attenuation coefficients of tissue types will be larger at KV energies compared to MV energies. There is not a large difference among different tissue materials in electron density (Ruchala *et al.*, 2000). Hence, loosely speaking, poor low contrast resolution is inherent to low dose megavoltage imaging. There are two main reasons for poor spatial resolution in MV imaging. Firstly, the detector resolution is poorer at MV energies due to Compton scattering within the detector and, in case of scintillation detectors, due to optical spreading within the detector. Secondly, the current linear accelerators have relatively large x-ray focal spots, ~2-3 mm (Munro *et al.*, 1988), which is larger than diagnostic CT scanner focal spots.

Besides poor low contrast resolution and poor spatial resolution, MV images also suffer from high noise or low SNR. X-rays in the range of therapeutic energies have a significantly lower probability of interaction with materials than photons in the diagnostic energy. Groh *et al.* (2002) have performed a detailed comparison of the use of MV and kV photon energies for CBCT. The authors conclude that kV CBCT offers significantly better LCR and SNR per unit patient dose compared to MV CBCT. Groh *et al.* also state that the poor SNR performance is mainly the result of low x-ray quantum efficiency (QE) of the current active matrix flat panel detectors at MV photon energies. For example the QE for film and cassettes is only ~1% (Herman *et al.*, 2001), and ~1.5% and ~2% to ~4% for currently used EPIDs which use a metal plate in contact with either a liquid ionization medium or with a phosphor screen, respectively (Antonuk, 2002).

If the use of MVCT is limited to patient position verification in fractionated radiotherapy involving alignment of bony landmarks, lung tissue and other inherently high contrast anatomical regions and structures, then MVCT systems that provide LCR less than 2% using 1-2 cGy will prove to be extremely useful. However, the majority of systems discussed above tend to use a large radiation dose to obtain useful contrast resolution in CT images. Hence, the performance of MVCT imaging systems can be significantly improved if highly efficient detectors are used. Therefore, the search for high quantum efficiency MV detectors is underway as evidenced by the recent theoretical and experimental developments (Pang and Rowlands, 2002 and 2004, Mei *et al.*, 2005, Sawant *et al.*, 2005, 2006, Monajemi *et al.*, 2004).

E. Solution to the Problems Associated with MVCT

As mentioned above the solution to the main problems associated with MV imaging lies in finding better and more efficient detectors. Detectors used in CT imaging are divided into two general groups: gas detectors and scintillation detectors.

Gas detectors use xenon gas at high pressures usually about 25 atmosphere. The gas is placed in long thin cells between two collecting electrodes. An external electric field is applied to the electrodes. The gas creates ionic charges in response to the energy deposited by x-ray photons. The ionic charge is collected by the electrodes and current is created in the front end electronics (Bushberg *et al.*, 2002). Due to the lower density of the gas relative to solid state detectors, the quantum efficiency is very low. To compensate for poorer detector efficiency, the detectors are made longer in the beam direction. Also the septa plates can be made very thin to reduce the dead spaces between sensitive elements. The quantum efficiency of the xenon gas is even poorer at MV photon energies unless the septa plates serve as the energy converter as is the case for the detector studied by Keller *et al.* for the bench-top MVCT (2002).

A scintillator basically absorbs a fraction of the energy from an incident high energy beam and converts it to optical photons. Since this thesis is based

on $CdWO_4$ scintillators, the first part of the next chapter is dedicated to explaining the signal formation process in scintillators and particularly in $CdWO_4$. Consequently, a detailed description of these processes will not be provided here. It will suffice for now to state that scintillation detectors show significant potential to become the detector of choice for 3D MV imaging.

In designing a detector for an imaging task, one needs to consider all components of the imaging system. In MVCT these components include the x-ray (or γ-ray in the case of Co^{60}) source, the beam spectrum, the distance from the source to both the patient bed and the detector planes and finally the detector itself. The treatment unit is not optimized for imaging, though it is possible to modify some of its components in order to improve the treatment environment for the task of imaging, while imaging the patient. An example of such an approach is replacing the linear accelerator target with a low-Z target (Ostapiak *et al.*, 1998), removing the flattening filter and reducing the energy of the x-ray beam for low contrast MV CBCT (Pouliot et al., 2005). Since we are working in a clinical institute where we have very limited freedom to make any modifications to the treatment units, our approach to MV imaging is to make the smallest possible change to the treatment unit. Therefore, of all the parameters mentioned above, the only component that we can modify freely is the detector itself.

The parameter that best quantifies the performance of a detector is the detective quantum efficiency, DQE. This parameter is discussed extensively in the following chapters. Employing a detector with a high DQE ensures high SNR and LCR in the resulting images. Therefore, using a detector with a high DQE is the key in improving MV image quality.

F. History of this Project and the Structure of this Thesis

In the first step of this project (Monajemi *et al.*, 2004) –which was the focus of the author's MSc thesis- a Monte Carlo model describing the signal acquired from a scintillation detector was developed which contained two steps: (1) the calculation of the energy deposited in the crystal due to MeV photons using the EGS*nrc* (Kawarakow and Rogers, 2002) Monte Carlo code; and (2) the transport

of the optical photons generated in the crystal voxels to photodiodes using the optical Monte Carlo code DETECT2000 (Levin and Moisan, 1996) . The measured detector signals in single $CdWO_4$ and CsI(Tl) scintillation crystals of base 0.275 x 0.8 cm^2 and heights 0.4, 1, 1.2, 1.6 and 2 cm were, generally, in good agreement with the signals calculated with the model. A prototype detector array which contained 8 $CdWO_4$ crystals each 0.275 x 0.8 x 1 cm^3 in contact with a 16-element array of photodiodes was built. The frequency dependent modulation transfer function ($MTF(f)$), noise power spectrum ($NPS(f)$), and $DQE(f)$ were measured for 1.25 MeV photons (in a $Cobalt^{60}$ beam). For 6 MV photons, only the $MTF(f)$ was measured from a linear accelerator, where large pulse-to-pulse fluctuations in the output of the linear accelerator did not allow the measurement of the $NPS(f)$ and the $DQE(f)$. The $DQE(0)$ of the detector array was found to be 26% and 19% for 1.25 MeV and 6 MV photons, respectively. In the next step of this project –which was the focus of the MSc thesis of another student in this department (Tu, 2005)- the eight element detector was expanded to an eighty element array and placed on an arc; a rotary stage was added and in this manner a bench-top CT scanner was created.

Since we are working with $CdWO_4$ scintillators in contact with Si photodiodes, the second chapter of this thesis is dedicated to describing in overview the signal formation process in scintillators, the x-ray/γ-ray interaction and transport properties in $CdWO_4$, the optical photon interaction and transport properties of $CdWO_4$, and the signal formation process in Si photodiodes.

In chapter 3, we focus on quantifying the imaging characteristics of the eighty element detector array. The instrumentation of the eighty element array with which the experiments in chapters 3 and 4 were carried out, is presented in this chapter. A detailed discussion of the concepts of $MTF(f)$, $NPS(f)$ and $DQE(f)$ is provided. We present how these parameters were measured for the eighty element detector. The stability of the response of the detector after prolonged exposure to radiation is also quantified in this chapter.

In chapter 4, a detailed description of the production of CT images from acquired projection data is presented. It was found that the raw CT images contained a number of artefacts including beam hardening and ring artefacts. Efforts to correct or minimize these are detailed. The resulting images are analyzed and the imaging performance of the detector is quantified in this manner.

In chapter 5, we return to the two step Monte Carlo method that we had previously developed to answer some questions regarding the best detector design for these scintillators and photodiodes for cone beam MV imaging. The crystal dimensions, septa material, beam spectrum, beam divergence, distance of the detector from both the source and the patient and scatter from the patient are all considered in this section.

Chapter 6 presents a summary of the project thus far and outlines some future directions for this project.

G. References

H. Alasti, M. P. Petric, C. N. Catton and P. R. Warde, " Portal imaging for evaluation of daily on-line setup errors and off-line organ motion during conformal irradiation of carcinoma of the prostate," Int. J. Radiat. Oncol. Biol. Phys. **49**, 869–884 (2001).

L. E. Antonuk, "Electronic portal imaging devices: a review and historical perspective of contemporary technologies and research," Phys. Med. Biol. **47**, R31-65 (2002).

J. M. Balter, G. T. Y. Chen, C. A. Pelizzari, *et al.*, "On-line repositioning during treatment of the prostate: A study of potential limits and gains," Int. J. Radiat. Oncol. Biol. Phys. **27**,137–143 (1993).

J. M. Balter, R.K. Ten Haken, T. S. Lawrence, *et al.*, "Uncertainties in CT-based radiation therapy treatment planning associated with patient breathing," Int. J. Radiat. Oncol. biol. Phys. **36**, 167-174 (1996).

P. Bergstrom, P. O. Lofroth and A. Widmark, "High-precision conformal radiotherapy (HPCRT) of prostate cancer—a new technique for exact positioning of the prostate at the time of treatment," Int. J. Radiat. Oncol. Biol. Phys. **42**, 305–311 (1998).

J. T. Bushberg, J. A. Seibert, E. M. Leidholdt and J. M. Boone, *The Essential Physics of Medical Imaging*, (Lippincott Williams & Wilkins, Philadelphia, 2002).

M. P. Carol, " Peacock™: a system for planning and rotational delivery of intensity modulated fields," Int. J. Img. Sys. Tech. **6**, 56-61 (1995).

C. Constantinou, J. C. Harrington and L. A. DeWerd, "An electron density calibration phantom for CT-based treatment planning computers," Med. Phys. **19**, 325-327 (1992).

L. A. Dawson, D. W. Litzenberg, K. K. Brock, *et al.*, " A comparison of ventilatory prostate movement in four treatment position," Int. J. Radiat. Oncol. Biol. Phys. **48**, 319-323 (2000).

W. DeNeve, C. DeWagter, K. DeJaeger, *et al.* "Planning and delivering high doses to targets surrounding the spinal cord at the lower neck and upper mediastinal levels: Static beam segmentation technique executed with a multileaf collimator," Radiother. Oncol. **40**, 271–279 (1996).

A. Eisbruch A, L. H. Marsh, M. K. Martel, *et al.* "Comprehensive irradiation of head and neck cancer using conformal multi segmental fields: Assessment of target coverage and noninvolved tissue sparing," Int. J. Radiat. Oncol. Biol. Phys. **41**, 559–568 (1998).

M. Endo, T. Tsunoo, N. Nakamori, and K. Yoshida, "Effect of scattered radiation on image noise in cone beam CT," Med. Phys. **28**, 469-474 (2001).

E. C. Ford, J. Chang, K. Mueller, *et al.*, "Cone-beam CT with megavoltage beams and an amorphous silicon electronic portal imaging device: Potential for verification of radiotherapy of lung cancer," Med. Phy. **29**, 2913-2924 (2002).

H. Fujita, K. Ueda, J. Morishita, *et al.*, "Basic imaging properties of a computed radiographic system with photostimulable phosphors," Med. Phys. **16** , 52-59 (1989).

M. Goitein, M. Abrams, D. Rowell, *et al.*, "Multidimensional treatment planning: II. Beam's-eye-view, back projection, and projection through CT sections," Int. J. Radiat. Oncol. Biol.Phys. **9**, 789–797 (1983).

B. A. Groh, J. H. Siewerdson, D. G. Drke, *et al.*, "A performance comparison of flat-panel imager-based MV and kV cone-beam CT," Med. Phys. **29**, 967-975 (2002).

H.Guan and Y. Zhu, "Feasibility of megavoltage portal CT using an electron portal imaging device (EPID) and multi-level scheme algebraic reconstruction technique (MLS-ART)," Phys. Med. Biol. **43**, 2925-2937 (1998).

M. G. Herman, J. M. Balter, D. A. Jaffray, *et al.*, "Clinical use of electronic portal imaging: Report of AAPM radiation therapy committee task group 58," med. Phys. **28**, 712- 737 (2001).

B. M. Hesse, L. Spies, and B. A. Groh, "Tomotherapeutic portal imaging for radiation treatment verification," Phys. Med. Biol. **43**, 3607-3616 (1998).

D. C. Hornick, D. W. Litzenberg, K. L. Kam, *et al.*, "A tilt and roll device for automated correction of rotational setup errors," Med. Phys. **25**, 1739–1740 (1998).

T.S. Hong, W. A. Tome, R. J. Champell, *et al.*, "The impact of daily setup variations on head-and-neck intensity-modulated radiation therapy," Int. J. Radiat. Oncol. Biol. Phys. **61**, 779-88(2005).

D. A. Jaffray, J. H. Siewerdsen, J. W. Wong, and A. A. Martinez, "Flat panel cone-beam computed tomography for image guided radiation therapy," Int. J. Radiat. Oncol. Biol. Phys. **53**, 1337-1349 (2002).

I. Kawrakow and D.W.O. Rogers, "The EGSnrc code system: Monte Carlo simulation of electron and photon transport," NRCC Report PIRS-701 (2002).

H. Keller, M. Glass, R. Hinderer, *et al.*, "Monte Carlo study of a highly efficient gas ionization detector for megavoltage imaging and image-guided radiotherapy," Med. Phys. **29**, 165-175 (2002).

K. Kuriyama, H. Onishi, N. Sano, T. Komiyama, *et al.*, "A new irradiation unit constructed of self-moving gantry-CT and linac," Int. J. Radiat. Oncol. Biol. Phys. **55**, 428-435 (2003).

L. C. Kwan, J. M. Boone, and N. Shah, "Evaluation of x-ray scatter properties in a dedicated cone-beam breast CT scanner," Med. Phys. **32**, 2967 (2005).

A. J. Lattanzi, S. McNeeley, W. Pinover, *et al.*, "A comparison of daily CT localization to a daily ultrasound-based system in prostate cancer," Int. J. Radiat. Oncol. Biol. Phys. **43**, 719–725 (1999).

A. Levin and C. Moisan, "A more physical approach to model the surface treatment of scintillation counters and its implementation into DETECT," IEEE Trans. Nucl. Sci. Symposium of Anaheim, 702-706 (1996).

D. G. Lewis, W. Swindell, E. J. Morton, *et al.*, "A megavoltage CT scanner for radiotherapy verification," Phys. Med. Biol. **37**, 1985-1999 (1992).

T. R. Mackie, T. Holmes, S. Swerdloff, *et al.*, "Tomotherapy: a new concept for the delivery of dynamic conformal radiotherapy," Med. Phys. **20**, 1709-1719 (1993).

T. R. Mackie, J. Kapatoes, K. Ruchala , *et al.*," Image guidance for precise conformal radiotherapy," Int. J. Radiat. Oncol. Biol. Phys. **56**, 89-105 (2003).

S. Midgley, R. M. Miller, and J. Dudson, "A feasibility study for megavoltage cone beam CT using a commercial EPID," Phys. Med. Biol. **43**, 155-169 (1998).

T.T. Monajemi, *Modeling Scintillator-Photodiodes as Detectors for Megavoltage Computed Tomography*, MSc Thesis, University of Alberta (2004).

T. T. Monajemi, S. Steciw, B. G. Fallone, and S. Rathee, "Modeling scintillator-photodiodes as detectors for megavoltage CT," Med Phys. **31**, 1225-34 (2004).

T.T. Monajemi, D. Tu, S. Rathee and B.G. Fallone, "A bench-top megavoltage fan-beam CT using $CdWO_4$-photodiode detectors: II- Image performance evaluation," Med. Phys. **33**, 1090-1100 (2006).

O. Morin, A. Gillis, J. Chen, *et al.*, "Megavoltage cone-beam CT: system description and clinical applications.," Med. Dosim. **31**, 51-61 (2006).

E.J. Morton, W. Swindell, D.G. Lewis, and P. M. Evans," A linear array, scintillation crystal-photodiode detector for megavoltage imaging," Med. Phys. **18**, 681-691 (1991).

M. A. Mosleh-Shirazi, P. M. Evans, W. Swindell, *et al.*, "A cone-beam megavoltage CT scanner for treatment verification in conformal radiotherapy," Radiotherapy and Oncology **48**, 319-328 (1998).

M. A. Mosleh-Shirazi, W. Swindell, and P. M. Evans, "Optimization of the scintillation detector in a combined 3D megavoltage CT scanner and portal imager," Med. Phys. **25**, 1880-1890 (1998).

C. D. Mubata, A. M. Bidmead, L. M. Ellingham, *et al.*, "Portal imaging protocol for radical dose-escalated radiotherapy treatment of prostate cancer," Int. J. Radiat. Oncol. Biol. Phys. **40**, 221–231 (1998).

P. Munro, J. A. Rawlinson and A. Fenster, "Therapy imaging: source sizes of radiotherapy beam," Med. Phys. **15**, 517-524 (1988).

P. Munro and D. C. Bouius, "X-ray quantum limited portal imaging using amorphous silicon flat-panel arrays," Med. Phys. **25**, 689–702 (1998).

P. Munro, "Megavoltage radiation for treatment verification", in *The Modern Technology of Radiation Oncology* , edited by Van Dyk J. (Medical Physics Publishing, Madison, WI, 1999), 481-508.

K. Nakagawa, Y. Aoki, A Akanuma, *et al.*, "Technical features and clinical feasibility of megavoltage CT scanning", Euro. Radiol. **2**, 184-189 (1992).

R. Ning, X. Tang, and D. Conover, "X-ray scatter correction algorithm for cone beam CT imaging," Med. Phys. **31**, 1195-1202(2004).

G. H. Olivera, D. M. Shepard, K. Ruchala, *et al.*, "Tomotherapy", in *The Modern Technology of Radiation Oncology* , edited by Van Dyk J. (Medical Physics Publishing, Madison, WI, 1999), 521-588.

O.Z Ostapiak, P. F. O'Brien and B. A. Faddegon, "Megavoltage imaging with low Z targets: implementation and characterization of an inverstigational system," Med. Phys. **25**, 1910-1918 (1998).

M. Partridge, M Ebert, and B-M. Hesse, "IMRT verification by three-dimensional dose reconstruction from portal beam measurements," Med. Phys. **29**, 1847-1858 (2002).

G. Pang, D. J. Beachey, P. F. O'Brien, *et al.*, "Imaging of 1.0-mm-diameter radio-opaque markers with megavoltage x-rays: An improved online imaging system," Int. J. Radiat. Oncol. Biol. Phys. **52**, 532–537 (2002).

G. Pang and J. A. Rowlands, "Development of high quantum efficiency flat panel detector: Intrinsic spatial resolution," Med. Phys. **29**, 2274–2285 (2002).

G. Pang and J. A. Rowlands, "Development of high quantum efficiency, flat panel, thick detectors for megavoltage x-ray imaging: A novel direct-conversion design and its feasibility," Med. Phys. **31**, 3004-3016 (2004).

A. Pirzkall, M. Carol, F. Lohr , *et al.*, "Comparison of intensity modulated radiotherapy with conventional conformal radiotherapy for complex shaped tumours," Int. J. Radiat. Oncol. Biol. Phys. **48**, 1371-1380 (2000).

J. Pouliot, A. Bani-Hashemi, J. Chen, *et al.*, "Low dose megavoltage cone beam CT for radiotherapy", Int. J. Radiat. Oncol. Biol. Phys. **61**, 552-560 (2005).

S. Rathee., D. Tu, T.T. Monajemi, *et al.*, "A bench-top megavoltage fan-beam CT using $CdWO_4$-photodiode detectors: I- System description and detector characterization," Med. Phys. **33**, 1078-1089 (2006).

P. Remeijer, E. Geerlof, L. Ploeger, *et al.*, "3-D portal image analysis in clinical practice: An evaluation of 2-D and 3-D analysis techniques as applied to 30 prostate cancer patients," Int. J. Radiat. Oncol. Biol. Phys. **46**, 1281–1290 (2000).

E. Rietzel, S. J. Rosenthal, D. P. Gierga, et al., "Moving targets: detection and tracking of internal organ motion for treatment planning and patient setup," Radiother. Oncol. **73** Suppl 2:S68-72 (2004).

J. A. Rowlands, "The physics of computed radiography," Physics in Medicine and Biology **47**, R123-R166 (2002).

K. J. Ruchala, G. H. Olivera, E. A. Schloesser and T. R. Mackie, "Megavoltage CT on a tomotherapy system," Phys. Med. Biol. **44**, 2597-2621 (1999).

K. J. Ruchala, G. H. Olivera, E. A. Schloesser, *et al.*, "Calibration of tomotherapeutic MVCT system," Phys. Med. Biol. **45**, N27-N36 (2000).

A. Sawant, L.E. Antonuk, Y. El-Mohri, *et al.*, "Segmented phosphors: MEMS-based high quantum efficiency detectors for megavoltage x-ray imaging," Med. Phys. **32**, 553-565 (2005).

A. Sawant, L. E. Antonuk, Y. El-Mohri, *et al.*," Segmented crystalline scintillators: An initial investigation of high quantum efficiency detectors for megavoltage x-ray imaging." Med. Phys. **32**, 3067-83 (2005).

A. Sawant, L. E. Antonuk, Y. El-Mohri, *et al.*, "Segmented crystalline scintillators: Empirical and theoretical investigation of a high quantum efficiency EPID based on initial engineering prototype CsI(Tl) detector," Med. Phys. **33**, 1053-1066 (2006).

E. J. Seppi, P. Munro, S. W. Johnsen, *et al.*,"Megavoltage cone-beam computed tomography using a high-efficiency image receptor," Int. J. Radiat. Oncol. Biol. Phys. **55**, 793-803 (2003).

G. Sherouse, K. L. Novins, E. L. Chaney, "Computation of digitally reconstructed radiographs for use in radiotherapy treatment design," Int. J. Radiat. Oncol. Biol. Phys.**18**, 651–658 (1990).

R. G. Simpson, C. T. Chen, E. A. Grubbs, and W. Swindell, "A 4-MV CT scanner for radiation therapy: The prototype system," Med. Phys. **9**, 574-579 (1982).

R. A. C. Siochi, "Minimizing static intensity modulation delivery time using an intensity solid paradigm," Int. J. Radiat. Oncol. Biol. Phys. **43**,671– 679 (1999).

J. Sonke, L. Zijb, P. Remeijer, and M. Van Herk, "Repertory correlated cone beam CT," Med. Phys. **32**, 1176-1186 (2005).

M. Sonoda, M. Takano, J. Miyahara, and H. Kato, "Computed radiography utilizing scanning laser stimulated luminescence," Radiology **148**, 833-838 (1983).

S. V. Spirou and C. S. Chui, "A gradient inverse planning algorithm with dose-volume constraints," Med. Phys. **25**, 321-333 (1998).

J. Stein, T. Bortfeld, B. Dorschel, *et al.*, "Dynamic X-ray compensation for conformal radiotherapy by means of multi-leaf collimation," Radiother. Oncol. **32**,163–173 (1994).

J. C. Stroom, M. J. J. Olofsen-van Acht, S. Quint, *et al.*,"On-line setup corrections during radiotherapy of patients with gynecologic tumors," Int. J. Radiat. Oncol. Biol. Phys. **46**, 499–506 (2000).

H. D. Suit, "Local control and patient survival," Int. J. Radiat. Oncol. Biol. Phys. **23**, 653– 660 (1992).

W. Swindell, R. G. Simpson, and J. R. Oleson, *et al.*, "Computed Tomography with a linear accelerator with radiotherapy applications," Med. Phys. **10**, 416-420 (1983).

D. Tu, *Bench-top Megavoltage Computed Tomography Scanner with Cadmium Tungstate-Photodiode Detectors*, MSc. Thesis, University of Alberta (2005).

J. Van de Steene, F. Van den Heuvel, A. Bel, *et al.*, "Electronic portal imaging with on-line correction of setup error in thoracic irradiation: Clinical evaluation," Int. J. Radiat. Oncol. Biol. Phys. **40**, 967–976 (1998).

E. Vigneault, J. Pouliot, J. Laverdiere, *et al.*, "Electronic portal imaging device detection of radio-opaque markers for the evaluation of prostate position during megavoltage irradiation—a clinical study," Int. J. Radiat. Oncol. Biol. Phys. **37**, 205–212 (1997).

L. Xing, Z. Lin, S. S. Donaldson, *et al.*, "Dosimetric effects of patient displacement and collimator and gantry angle misalignment on intensity modulated radiation therapy," Radiation Oncol. **56**, 97-108 (2000).

M. Yazdia, L. Gingras and L. Beaulieu, "An adaptive approach to metal artifact reduction in helical computer tomography for radiation treatment planning:experimental and clinical studies", Int. J. Rad. Onc. Biol. Phys. **62**, 1224-1231 (2005).

Chapter 2

Signal Formation in $CdWO_4$ –Si Photodiodes

Since we are working with $CdWO_4$ scintillators and silicon photodiodes throughout this thesis, the present chapter is dedicated to describing the properties of $CdWO_4$ as relevant to our work. An overview of the MV energy detection process by scintillators is provided. The MV and optical photon interaction properties of $CdWO_4$ are presented. In addition, the optical photon detection mechanism in photodiodes and in particular in silicon photodiodes, is discussed along with the detection properties of the silicon photodiodes used in this research.

A. Scintillation Detectors

Scintillators convert excitation energy into light, resulting in luminescence. Luminescence caused by radiation is called scintillation (Ishii and Kobayashi, 1991). A good scintillation detector has high density and high atomic number. High density and atomic number values translate into larger interaction cross sections with MV photons. A good scintillator possesses relatively high light output; the conversion to optical photons is a linear process as a function of deposited energy; it has good optical photon transmission properties as well as a short decay time enabling fast light collection; finally a good scintillator has good resistance to radiation and is easy to manufacture and handle. (Knoll, 1989)

There are three general optical emission processes though which a scintillator can de-excite following the incidence of ionizing radiation. *Fluorescence* refers to the prompt emission of optical photons immediately following excitation. *Phosphorescence* refers to the emission of longer wavelength optical photons with a characteristic time that is slower than fluorescence. *Delayed fluorescence* has the same emission spectrum as prompt

fluorescence but has a much longer emission time following excitation. Prompt fluorescence is the most desirable form of de-excitation in scintillators. (Knoll, 1989) There are other processes of de-excitation which do not involve the emission of light and mainly involve the generation of heat. All these processes are grouped together and referred to as *quenching*.

Scintillators are divided into four general groups: inorganic (e.g. CsI(Tl) , NaI(Tl)), organic based crystals (e.g. Anthracene, Stilbene), organic liquids (e.g. NE 213, NE 260) and organic plastics (e.g. NE 102, NE 105). Inorganic scintillators have the largest light output per unit energy absorbed which is highly linear with the amount of energy absorbed. For example, the average light output of NaI(Tl) at 38,000 photons/MeV is 2.3 times larger than that of Anthracene, which has the highest output among organic scintillators. On the other hand, inorganic scintillators are relatively slow in responding to radiation. Decay time of organic scintillators is in the few nano seconds range compared to a few hundred nano seconds range for inorganic scintillators. Since inorganic scintillators have 4-8 times higher density than organic scintillators with densities around 1.5 g/cm^3, they provide higher interaction cross-section in high energy x-ray and gamma ray detection applications. Organic scintillators are used in beta spectroscopy and fast neutron detection. (Knoll, 1989). Since this thesis is based on work performed with $CdWO_4$ crystals, the rest of this chapter is dedicated to describing the scintillation process and properties of inorganic scintillators and $CdWO_4$ in particular.

B. Scintillation Mechanism

Following is a literature survey of the scintillation mechanism in inorganic scintillators and $CdWO_4$ in particular. The experimentally obtained MV/optical properties are adequate to understand and perform the simulation of imaging properties of CT detectors formed using these crystals. Therefore a detailed discussion of the exact scintillation mechanism is beyond the scope of this thesis. The following section is included for the sake of completeness and better

understanding of our detector, but is not meant as a rigorous explanation of the scintillation mechanism.

i. An Overview of the Scintillation mechanism in inorganic scintillators

The process of scintillation is complicated and is often described by using the band theory of solids. In a pure crystal (see figure 2.1), the *forbidden gap* describes the band of energies between the *valence band* -where electrons are bound at lattice sites- and *conduction band* -where electrons have sufficient energy to move through the crystal. Absorption of energy results in the elevation of electrons from the valence band to the conduction band and leaves a hole in the valence band. There is a possibility that the energy transferred to a valence electron is too small to produce ionization but large enough to elevate the electron above the valence band. This electron will remain electrostatically bound to the hole in the valance band. The electron-hole pair is known as an *exciton*. The exciton states form a thin energy band with an upper end which coincides with the lower edge of the conduction band. In a crystal with no impurities, the process of de-excitation by the return of electrons to the valence band: (a) may be an inefficient process and (b) results in production of photons with energies higher than the range of visible photons. Therefore, typically small amounts of impurities, called *activators*, are added to the crystal (figure 2.1). Activators create energy states in the forbidden gap. The luminescence originates from "*luminescence centres*". Luminescence centres may be intrinsic to the material, or may be extrinsic such as luminescence associated with impurities or defects and additive dopant ions. In the case of an activator, the dopant ion may itself be the luminescence centre or it may promote luminescence as in the case of defect bound exciton emission. (Derenzo *et al.*, 2003)

The general mechanism by which luminescence occurs in scintillators can be divided into three stages (Derenzo *et al.*, 2003):

Stage 1: The ionization event produces an inner shell hole and an energetic primary electron. This process sets off a cascade of energy losses by radiative decay which produces secondary x-rays , non radiative decay through Auger

electrons, and inelastic electron-electron scattering, all in the time domain of 10^{-15} to 10^{-13} s.

Stage 2: When the energy of the resulting electrons is less than the ionization threshold, the electrons and holes thermalize by intra-band transitions and electron-phonon relaxations. These hot charge carriers can become trapped in defects and impurities, become self-trapped by the crystal lattice structure, or form free and impurity bound excitons in the time scale of $\sim 10^{-12}$ to 10^{-11} s. During this time the elevation of a luminescence centre to an excited state may result from the absorption of a photon produced by the decay of an excited state in the conduction band, the capture of a migrating electron and hole, the capture of an exciton, or impact excitation by hot electrons. The elevation of luminescence centres happens in $>10^{-12}$ to $<10^{-8}$ s.

Stage3: The excited luminescence centres return to the ground state by non-radiative quenching processes or by emitting a photon in a time scale of $\sim 10^{-9}$ s. The excited state at the luminescence centre may be a state for which de-excitation to the ground state is forbidden. This excited state needs to acquire additional energy by another means, usually thermal, to get to a state where it can de-excite to the ground state. This results in delayed radiation, or phosphorescence, and is the source of afterglow.

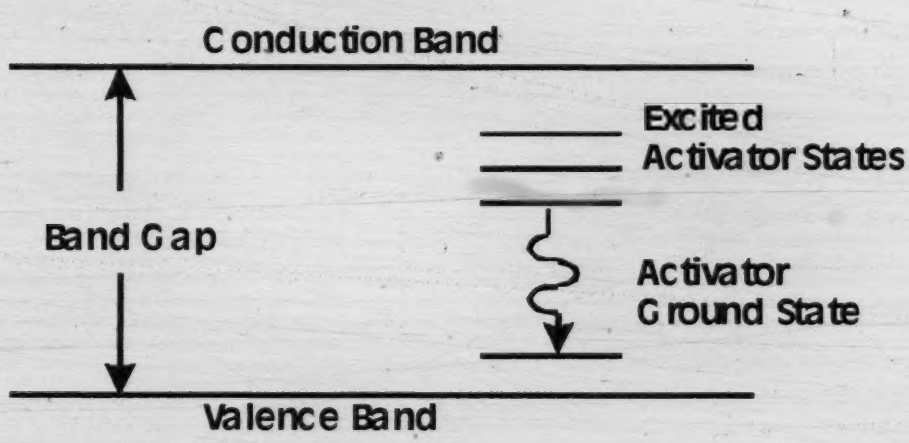

Figure 2.1: Energy band structure in scintillators with activator states (Knoll, 1989).

ii. Scintillation Mechanism in $CdWO_4$

Cadmium tungstate is an example of a scintillator that decays via intrinsic scintillation. This mechanism is shown in figure 2.2. In intrinsic scintillation the incident radiation ionizes constituent atoms or valence band electrons. Hence, electrons break free from their ionic bonds and are raised to the conduction band leaving holes in the valence band. Excitation produces a weakly coupled electron-hole pair, i.e. an exciton with an energy state just below the conduction band. Electrons with energy levels equal to or more than the ionization enegy, drift about in the crystal and are easily captured by positive ions. A photon is emitted in this process and the electron drops down to the valence band (Ishii and Kobayashi, 1991). If the energy of the electrons is less than the ionization threshold, the electrons and holes thermalize by intra-band transitions and electron-phonon relaxations.

$CdWO_4$ crystallizes in the wolframite-type structure and has a monoclinic symmetry with unit cell dimensions of a = 5.029 Å, b = 5.859 Å, and c = 5.074 Å, and β =91.47°. The unit cell consists of two formula units as shown in figure 2.3 (Morell *et al.*, 1980).The first study on the optical properties of cadmium tungstate was done by Kröger in 1948 and an intense blue-green emission peaking near 480 nm (2.58 eV) at 300 Kelvin was reported. This intrinsic "blue" emission has been attributed to transitions within the tungstate molecular unit WO_4^{2-} (Lammers, 1981). The intrinsic blue photoluminescence originating from the tungstate group can be explained as follows: when the crystal is excited with above band gap energy, electron-hole pairs are created. The electrons are attracted only by W^{6+} ions because they are the most highly ionized, and the holes will be attracted by O^{2-} ions. When electrons and holes recombine, the blue luminescence will occur (Chirila, 2000). A second emission band in $CdWO_4$ has been reported near 570 nm at liquid helium temperature for excitation wavelengths longer than 320 nm (Lammers 1981). This second emission band is of no importance in our application.

Upon simple visual inspection, one can see that the optical properties of intrinsic scintillator crystals can be strongly influenced by the presence of

impurities. Cadmium tungstate has superior scintillation characteristics and radiation stability in samples with the smallest content of impurity. For example, a small quantity of impurities, like: Fe, Mg, Cr, Co, or Ni (the most common) will change the water clear or nearly water clear colour of the crystal to red or dark-yellow, light green, brown, blue and pink, respectively, resulting in a decreased light output. (Chirila, 2000)

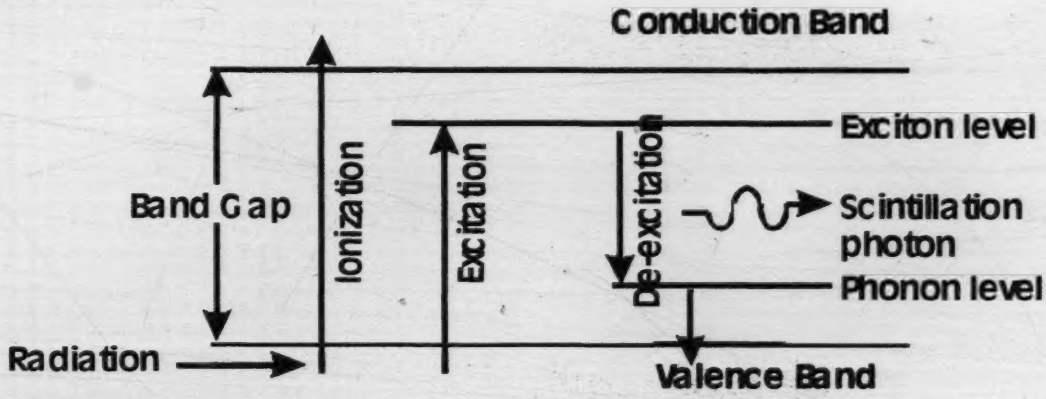

Figure 2.2: Scintillation process in intrinsic inorganic crystals (Ishii and Kobayashi, 1991).

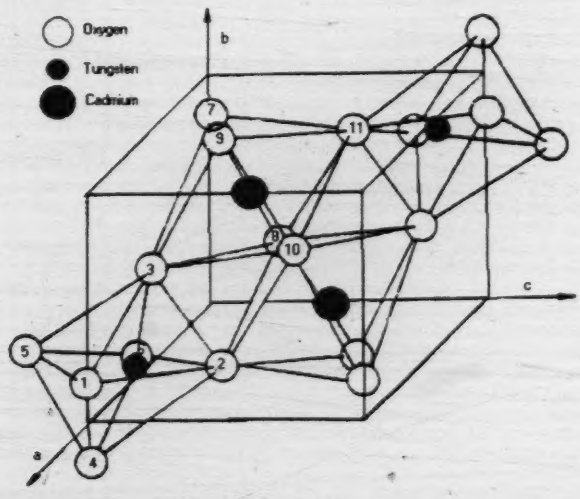

Figure 2.3: Crystal structure of $CdWO_4$ (Morell *et al.*, 1980).

C. Relevant Properties of $CdWO_4$

i. MV Photon Interactions

MV photon interactions form the first step in the transfer of energy from high energy photons to the scintillating material. Four types of MV photon interactions are important in the therapeutic energy range. These four processes are coherent scattering, photoelectric effect, Compton scattering and pair production. Each of these interactions is represented by its own coefficient which depends on the energy of the incoming photon and the atomic numbers of the absorbing materials (Khan, 2003). The total interaction coefficient is the sum of individual coefficients for each process. Table 2.1 gives the interaction coefficients at 1.25 MeV and 2 MeV for $CdWO_4$. These two energies, which are used in this project, are the mean energies of a Co^{60} source and a typical 6 MV beam from a medical linear accelerator. Figure 2.4, shows these coefficients as a function of energy.

Rayleigh or Coherent Scattering: As x-ray photons pass over an atom, the electric field component of their electromagnetic wave momentarily vibrates the electrons in the atom. These electrons then emit radiation with the same wavelength as the incident radiation. Therefore no transfer of energy takes place; only a slight change of direction of the incoming MV beam. The cross section for Rayleigh scattering decreases rapidly as the energy of the incident photons increases and is almost negligible for energies greater than 100 keV in low atomic number materials (Johns and Cunningham, 1983). This process is only important in high atomic number materials and at low photon energies. As shown in table 2.1, it only accounts for less than 1% of interactions at 2 MeV. These interactions do not contribute strongly to the photon scattering processes in the energy range studied in this thesis.

Photoelectric Absorption: In this process, a high energy photon collides with an atom and ejects one of the bound electrons from the K, L, M or N shells.

This ejected electron is called a *photoelectron* and possesses energy equal to the energy of the original photon minus its own binding energy. The atom is left in an excited state and emits characteristic radiation and/or Auger electrons (Auger electrons are mono-energetic electrons which carry away the excess energy of the atom by absorbing the characteristic x-ray) until it is returned to its ground state. In high atomic number materials such as $CdWO_4$, the binding energy is high and therefore the characteristic x-ray will have high energy and is likely to move further than the photoelectron before depositing its energy. The photoelectric cross section varies with photon energy approximately as $Z^3/(hu)^3$, where hu is the photon energy (Johns and Cunningham, 1983). The photoelectric edges seen on figure 2.4 occur at the L_3 edge of W at 1.02E-02 MeV, K edge of Cd at 2.67E-02 MeV and K edge of W at 6.95E-02 MeV (NIST, 2006). The angular distribution of the photoelectron depends on photon energy. At low energies, the photoelectron is emitted at 90 degrees to the direction of the incident photon. As the photon energy increases the photoelectron is emitted more in the forward direction (Khan, 2003). At the K edge of W (maximum energy loss case), this corresponds to 1.18 MeV electrons in a 1.25 MeV beam and 1.93 MeV electrons in a 2 MeV beam.

Compton or Incoherent Scattering: In this process, an incoming photon interacts with a free electron. Here, the term 'free' means that the electron binding energy is much less than the energy of the incoming photon. A fraction of the incident photon energy is transferred to the kinetic energy of the electron and the rest is given to the scattered photon. Both the energy and momentum are conserved at the point of interaction, thus, the initial angle of the electron set in motion (θ) and angle of the scattered photon (ϕ) are easily determined. In soft tissue, Compton scattering is the most dominant form of interaction in the range of 100 keV to 10 MeV (Johns and Cunningham, 1983). As seen in table 2.1 this process accounts for approximately 90% of interactions between 1 and 2 MeV in $CdWO_4$. The Compton interaction cross section is independent of Z and depends only on the number of electrons per gram (Johns and Cunningham, 1983). The importance of Z comes in when we note that to get the same number of electrons/g of

material we can have more compact detectors with high Z scintillators as opposed to low Z ones. In the energy range of interest to this thesis, the mean energy transferred to a recoil electron in the Compton process is close to 50% of that of the interacting photon while the maximum energy transfer to the electron is 90%. It should be noted that the energy given to the recoil electron depends on its recoil angle and thus the electron energy follows a broad spectrum. This spectrum of electrons contributes to the absorbed energy distribution function (AED) in the scintillator. As shown in chapter 5, the DQE of a detector can be calculated by using the AED. For now it suffices to say that, a detector with a narrow AED – meaning that most electrons have the same amount of energy and deposit all of their energy in the detector- have the highest DQE and are most desirable as scintillators.

Pair Production: This process is only possible if the energy of the incident photon is greater than 1.02 MeV. If photons pass near the nucleus of an atom, the photon is absorbed and a positron and an electron are created (an example of conversion of energy into mass). Occasionally, this process occurs in the field of an electron, in which case it is called triplet production. The cross section for pair production process increases as the energy of the incident photon increases. (Johns and Cunningham, 1983). The interaction cross section per unit mass varies with Z. This interaction accounts for 0.41% of interactions at 1.25 MeV and 7.6% at 2 MeV in our detector. The energy transfer in pair production is equal to the energy of the incoming photon minus 1.022 MeV.

Table 2.1: MV photon interaction coefficients in $CdWO_4$ at the two energies most relevant to this thesis (NIST, 2006)

Energy (MeV)	Coherent (cm^2/g)	Compton (cm^2/g)	Photoelectric (cm^2/g)	Pair (nuclear field) (cm^2/g)	Pair (electron field) (cm^2/g)	Total (cm^2/g)
1.25	1.06E-03	4.85E-02	4.82E-03	2.19E-04	0.00E+00	5.35E-02
2	4.17E-04	3.77E-02	2.08E-03	3.28E-03	0.00E+00	4.30E-02

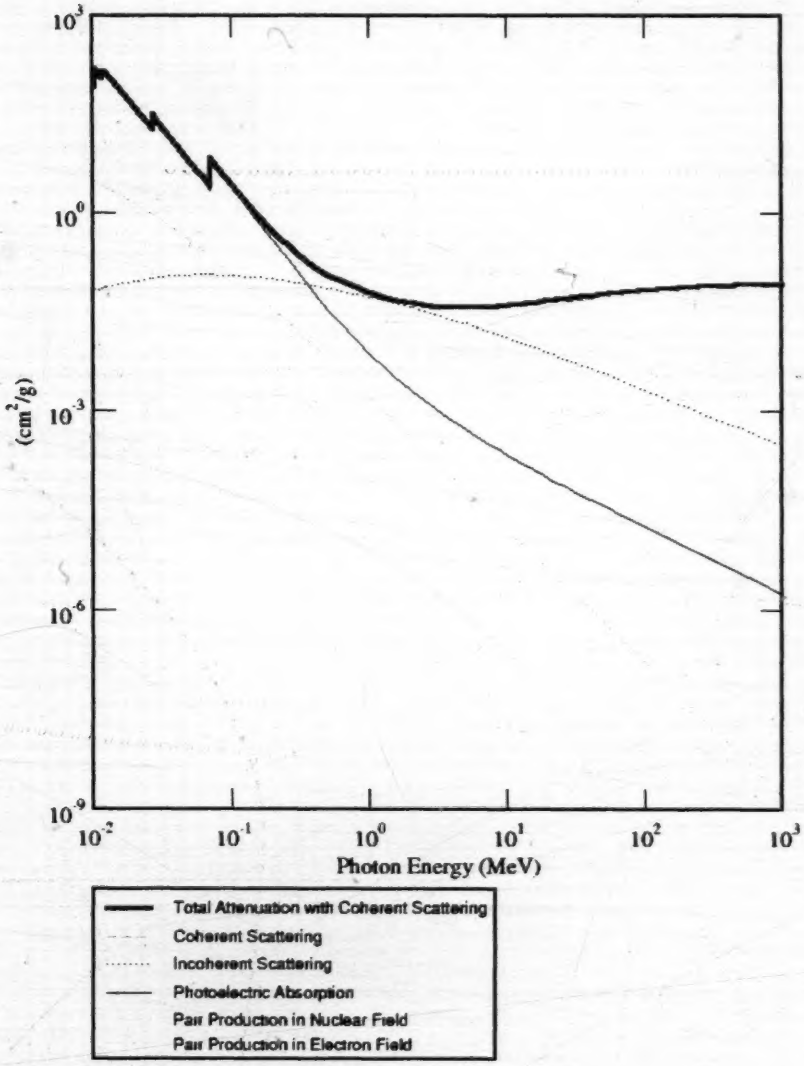

Figure 2.4: MV photon interaction coefficients in $CdWO_4$ as a function of energy (NIST, 2006)

ii. Electron Interactions

While MV photon interactions serve to transfer energy from the incident radiation to electrons in the medium, the actual deposition of energy is accomplished by electron interactions. The four electron interaction processes are inelastic collision with atomic electrons (ionization and excitation), inelastic collision with nuclei (bremsstrahlung), elastic collision with atomic electrons and elastic collision with nuclei (Khan, 1984). Electrons go through many elastic collisions along their paths which lead to frequent direction changes (Kawrakow and Rogers, 2002). The two mechanisms of energy loss described below are responsible for the energy transferred to the scintillator in the first stage of scintillation process described above.

Collisional energy losses: In these interactions, some kinetic energy of fast charged particles is transferred to the electrons in the medium. This transfer of energy leads to the excitation and ionization of atoms. These excited atoms then return to their ground state via the emission of characteristic photons and/or Auger electrons. (Kawrakow and Rogers, 2002).

Radiative energy losses: Radiative energy losses occur in the form of annihilation photons and bremsstrahlung for positrons and bremsstrahlung for electrons. Bremsstrahlung becomes the more important process as the energy of the electrons increases. Bremsstrahlung refers to radiation produced as a result of the deceleration of electrons (Johns and Cunningham, 1983). Once a positron finally comes to rest as a result of multiple Coulombic interactions, it is annihilated by combining with a free electron to produce two photons of 0.511 MeV, that are each ejected in opposite directions from the point of annihilation (an example of mass being converted to energy) (Johns and Cunningham, 1983).

The rate of energy loss per gram per cm^2 for electrons is called the mass stopping power. In low atomic number materials, electrons lose energy mostly though ionizing events with other electrons. In higher atomic number materials, however, the bremsstrahlung process becomes more important. The total

stopping power is the sum of collisional and radiative stopping powers. These quantities are shown for $CdWO_4$ as a function of electron energy in figure 2.5.

A measure of the range of electrons in a medium is given by the continuous slowing down approximation (CSDA) range. In calculating this range all the collisions in the slowing down process are assumed to cause very small energy changes. This means that catastrophic energy transfer events such as the production of a δ-ray (a secondary electron created by Moller scattering of the incoming fast electron) are accounted for by averaging their energy loss as if it were continuous. This quantity is shown for $CdWO_4$ as a function of energy in figure 2.6.

According to figure 2.5 the mass stopping power for a 2 MeV electron (this is higher than fast electrons in our experiments, but we are considering it as an example for the worst case) the mass stopping power is ~1.5 $MeV.cm^2/g$ resulting in a 2 $MeV.cm^2/g$. 8 g/cm^3 = 16 MeV/cm energy loss. The CSDA range for these electrons is no larger than 2 mm according to figure 2.6. This is important and desirable in our application because we know that the dimension of our detector (2.75 x 8 x 10 mm^3) is adequate for stopping most of the the recoiled electrons in one scintillator.

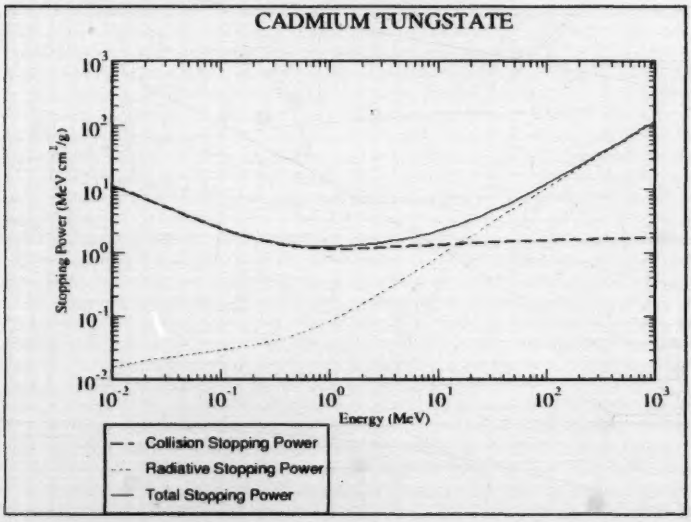

Figure 2.5: Electron mass stopping power in $CdWO_4$ as a function of energy (NIST, 2006).

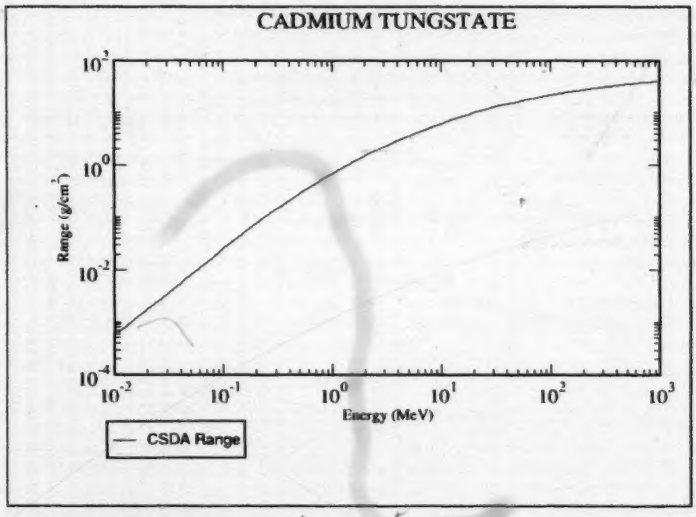

Figure 2.6: Electron CSDA range in $CdWO_4$ as a function of energy (NIST, 2006).

iii. Optical and Mechanical Properties of $CdWO_4$

Characteristics of typical scintillators used in kVCT imaging are shown in table 2.2 (Ishii and Kobayashi, 1991). The afterglow of $CdWO_4$ upon x-ray irradiation is very low, typically less than 0.1% of the useful signal after 3 ms following the end of x-ray exposure (Saint-Globain Ceramics & Plastics, 2002). We measured this value to be 0.02% for our crystals (Monajemi et al., 2004). In diagnostic CT imaging, detector arrays are used to measure the x-ray projections of the scanned object at a very rapid rate (typically > 1000 per second). Therefore, the negligible afterglow in $CdWO_4$ crystals is a highly useful property for CT imaging. For this reason the decay constant of the scintillator is also of importance. The intensity of emission after the end of excitation, $t = 0$, is approximately given by (Ishii and Kobayashi, 1991): $I(t) = I_0 \exp(-t/\tau)$; I_0 is the intensity of emission at $t = 0$ and τ is the decay constant. While the afterglow of $CdWO_4$ is small, the decay constant is relatively large (table 2.2). However a decay constant of 5000 ns is still much shorter than ~0.001s, a typical sampling rate of a CT detector.

Table 2.2: Characteristics of typical scintillators in kVCT applications (Ishii and Kobayashi, 1991).

Quantity	NaI:Tl	CsI:Tl	$CdWO_4$	$ZnWO_4$	$Bi_4Ge_5O_{12}$
Afterglow(%/ms)	0.5-5/3	0.1-0.8/6	0.005/3	0.005/3	0.005/3
Effective atomic number Z_{eff}	51	54	64	65	75
Density (g/cm^3)	3.67	4.53	7.9	7.87	7.13
Decay constant (ns)	230	1050	5000	5000	300
Peak emission (nm)	415	550	470/540	475	480
Light yield (relative)	100	85	38	28	7-10
Index of refraction*	1.85	1.80	2.3	2.1	2.15
Peak excitation (nm)	290	300**	330	320	280
Hygroscopy	strong	slight	no	no	no
Melting point (^{0}C)	651	621	1272	1220	1050
Radiation hardness (rad)	10^5	10^5	10^5	-	10^{4-5}
Hardness (Mohs)	2	2	4-4.5	5	5
Cleavage	(100)	none	(101)	(101)	none

* at 150 keV

** the one with the longest wavelength out of the 6 absorption bands.

The optical emission spectrum of $CdWO_4$ crystals as well as the absorption of light in the emission region is shown in figures 2.7 and 2.8 (Kinloch *et al.*, 2002). Even though there is a shift between the peak excitation and emission in these crystals (table 2.2), self-absorption in $CdWO_4$ is not negligible (figure 2.8); this issue becomes important in designing detectors with tall crystals as discussed in chapter 5.

As mentioned above, the crystallography of $CdWO_4$ is complex. $CdWO_4$ shows monoclinic symmetry, i. e. one of the axes of the unit cell is perpendicular to the other two which in turn are not perpendicular to each other. As a result of the crystal structure, these crystals have a cleavage plane <010> and cannot be fabricated having two sides both less than 1 mm long. The intensity of the

scintillation emission of $CdWO_4$ varies with temperature only slightly near room temperature (300 K) with a change of -0.1%/C°(Saint-Globain Ceramics & Plastice, 2002). Therefore, the calibration of $CdWO_4$ based detector arrays used in diagnostic CT scanners is fairly stable over varying ambient temperature conditions. Light travelling in the crystal normal to the cleavage plane experiences an index of refraction of about 4% less than light whose direction of travel lies in the cleavage plane. The index of refraction is 2.2-2.3 in the emission region (Kinloch *et al.*, 2002). The refractive index of the silicon photodiodes is 1.54 for an epoxy glass window. The index of refraction of the optical glue which we place between the scintillators and photodiodes is 1.47 (Dow Corning glue; Montechi and Ingram, 2001). Since the refractive index of the scintillator is higher than that of the optical glue, total internal reflection occurs between the scintillator and glue with a critical angle of 41°. This situation is not ideal; the high index of refraction of the scintillator is a drawback as it sends photons back into the crystal and increases their probability of absorption.

Radiation damage phenomenon refers to the appearance of absorption bands, caused by colour formation centres in crystals after long exposures to ionizing radiation. These absorption bands reduce the transmission of light through the crystal (Zhu et al., 1995). Radiation hardness of $CdWO_4$ crystals has been studied previously (Kobayashi et al., 1994, Kozma et al., 2000) using a Co^{60} beam for doses of 10^5Gy and 10^8Gy. The conclusion was that degradation in optical transmittance was less than 2%/cm for doses up to 10^8 rad when the measurement was carried out for several tens of hours after irradiation. In the specification sheet for our crystals (Saint-Globain Ceramics & Plastics, 2002) this value is reported to be a 15% decrease in optical transmission after 10^6 rad. $CdWO_4$ scintillation crystals have been used extensively in single slice diagnostic CT systems; the radiation damage to the crystal-photodiode pair is not a significant issue if utilized for MVCT alone. However, the final goal of this project is to create a 2-D detector array that can be utilized both for imaging and exit fluence measurements during radiotherapy treatments. In this situation, the detector array may receive up to 30 Gy per day based on 50% transmission

through thirty patients each receiving a dose fraction of 2 Gy. We report the effect of radiation on our detector system (i.e. detector + photodiodes) in the following chapter.

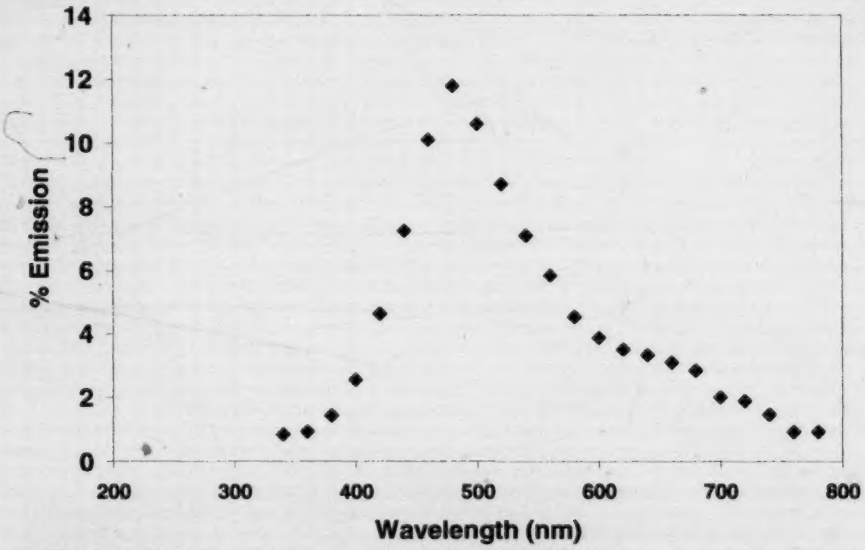

Figure 2.7: Emission spectrum in $CdWO_4$ (Kinloch *et al.*, 2002).

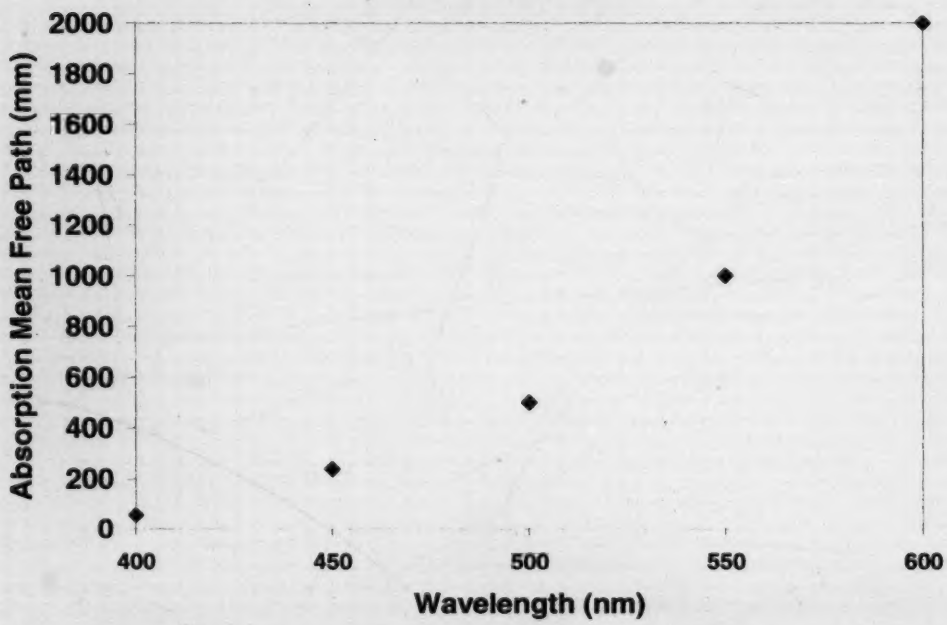

Figure 2.8: Absorption mean free path in $CdWO_4$ (Kinloch *et al.*, 2002).

D. Photodiodes

The function of a photodiode is to convert the incident optical energy into electrical signals. The process by which silicon photodiodes perform this function can be easily understood through the physics of semiconductor electronics. To control the number of charge carriers in semiconductors, they are usually doped with impurities. Elements from column III of the periodic table produce more holes by accepting electrons from semiconductors, whereas elements from column V donate electrons thereby producing an excess of free electrons. The first group of semiconductors is called p-type (acceptors) and the latter, n-type (donors). The point of contact between a p-type and an n-type material is called a p-n junction. In a small region around the p-n junction, electrons and holes come into contact with each other and recombine, leaving neither free electrons nor holes. The lack of free electrons leaves the n-type material positively charged; similarly the lack of holes leaves the p-type material negatively charged. This region is called the depletion region and is shown in figure 2.9 a. In the presence of external voltage, V_B, two types of currents flow in the pn junction material. The first one is diffusion current, I_d, flowing from the p-type material to the n-type material. In order for the diffusion current to occur, the electrons and holes must have enough thermal energy to overcome the depletion region barrier. The second current is called reverse saturation current, I_0, and flows from the positive side of the depletion region to the negative side. If a positive voltage is connected to the p-type semiconductor and a negative voltage to the n-type, the semiconductor circuit is called forward biased; when a negative voltage is connected to the p-type and the positive to the n-type, the circuit is called reversed biased. In a forward-biased circuit, the total current is given by:

$$i_{total} = I_d - I_0 \tag{2.1}$$

In a reverse-biased circuit, the depletion region is too large for the diffusion current to flow. Therefore the total current is given by:

$$i_{total} = -I_0 \tag{2.2}$$

When light hits the depletion region of a p-n junction in a photodiode, photons create electron-hole pairs through a process called photo-ionization. In this case the reverse saturation current is the sum of the drift current and the photocurrent. This phenomenon is the basis for the operation of photodiodes. This additional current is called i_{photo}. In the case of photodiode operation, equations 2.1 and 2.2 still apply with the modification that I_0 is equal to the sum of I_0 and i_{photo}. If no external voltage is provided but optical light is present, the only current going through the photodiode is i_{photo}. The three modes of operation of a photodiode are shown in figure 2.9b-d. The i-v characteristic curve of a photodiode is shown in figure 2.9e. As shown in this figure, the response of the photodiode is linear if it is operated in reverse-biased mode or with no external voltage (Rizzoni, 2000). In these regions, the increase in reverse saturation current is directly proportional to the incident optical energy φ_{light}. Even though operating a photodiode in reverse-bias voltage mode has the advantage of increased sensitivity due to the larger size of the depletion region, the statistical (shot) noise in i_{total} is high. Therefore, our photodiodes were operated with no external voltage. The sensitivity spectrum of the photodiodes used in this study (S5668-02 Hamamatsu Corporation) is shown in figure 2.10.

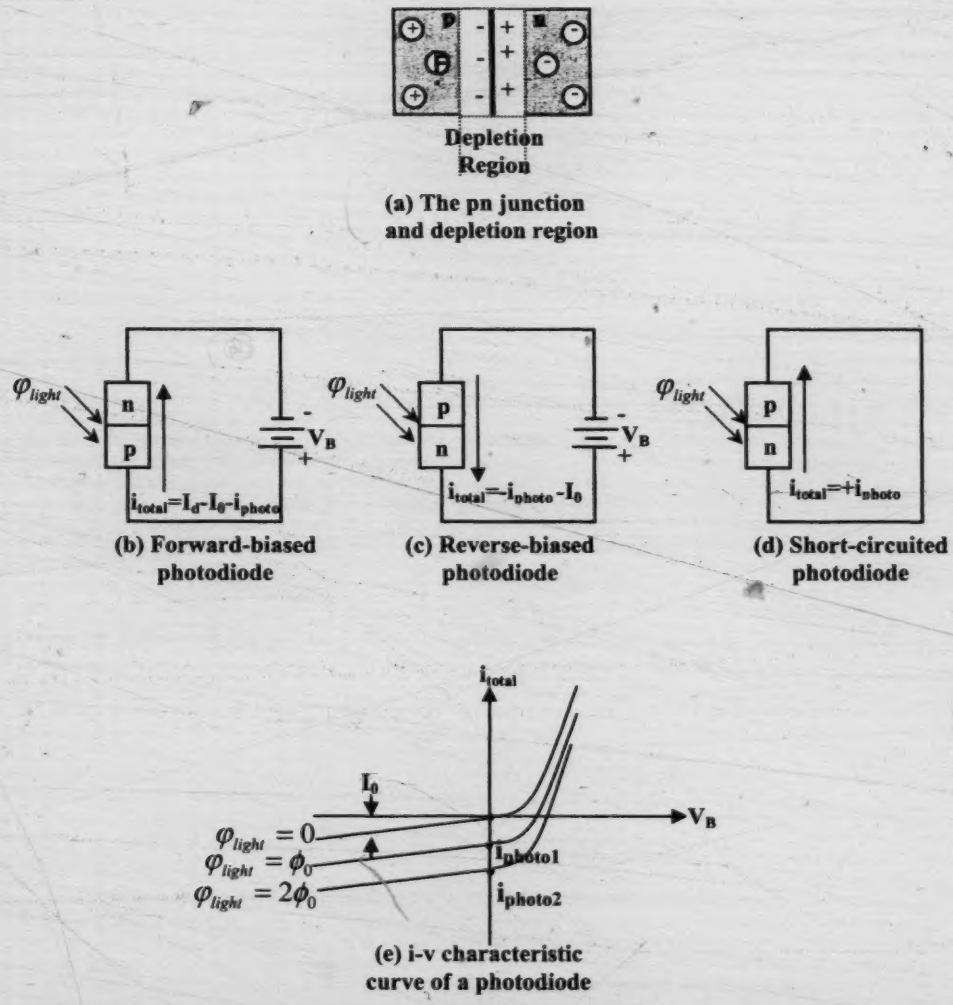

Figure 2.9: The Basis of Operation of Photodiodes: (a) a pn junction. (b)-(d) a photodiode operating in forward-biased, reverse-biased and short-circuited mode respectively. (e) the i-v characteristic curve of a photodiode.

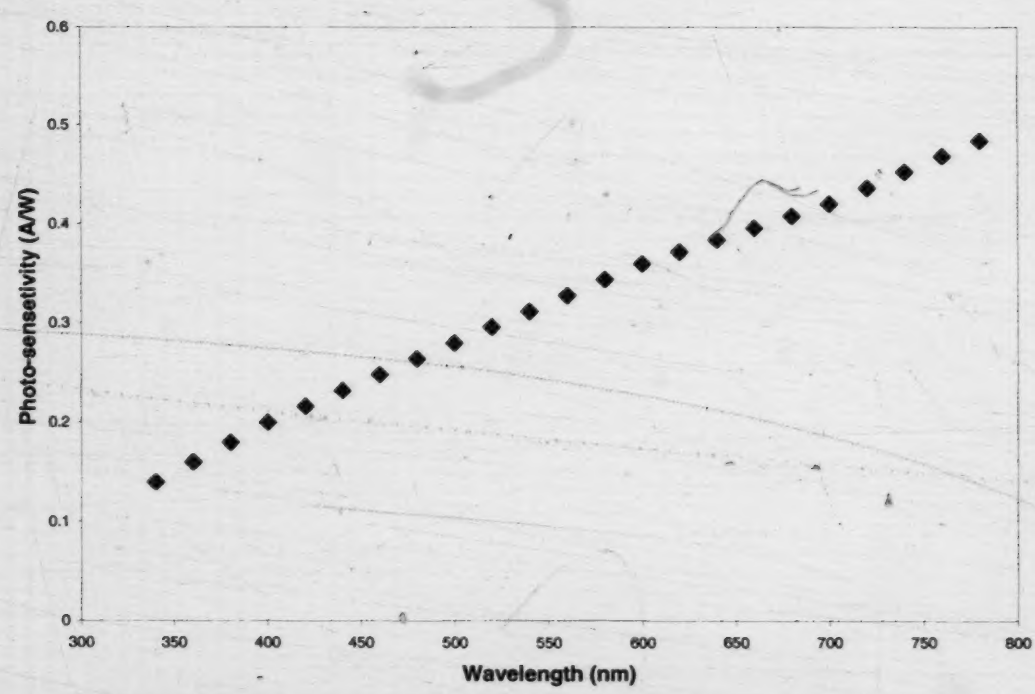

Figure 2.10: The sensitivity spectrum of S5668-02 Hamamatsu silicon photodiodes.

E. References

M. Chirila, *The influence of point defects on the optical properties of cadmium tungstate*, West Virginia University, MSc thesis (2000).

S. E. Derenzo, M. J. Weber, W. E. Bourret-Courchesne and M. K. Klintenberg, "The quest for the ideal inorganic scintillator," Nuclear Instruments and Methods in Physics Research Section A: Accelerators, Spectrometers, Detectors and Associated Equipment, **505**, 111-117 (2003).

M. Ishii and M. Kobayashi, "Single crystals for radiation detectors," Prog. Crystal Growth and Charact. Mater. **23**, 245-311 (1991).

H. E. Johns and J. R. Cunningham, *The Physics of Radiology*, 4th ed. (Thomas, Springfield, IL, 1983).

I. Kawrakow and D.W.O. Rogers, "The EGSnrc code system: Monte Carlo

simulation of electron and photon transport," NRCC Report PIRS-701 (2002).

D. R. Kinloch, W. Novak, P. Raby, and I. Toepke, "New developments in Cadmium Tungstate", IEEE Trans. Nucl. Sci., **41**, 752-754 (1994).

F. M. Khan, *The physics of radiation therapy*, Lippincott Williams & Wilkins, third edition, 2003.

M. Kobayashi, M. Ishii, Y. Usuki and H. Yahagi, "Cadmium tungstate scintillators with excellent radiation hardness and low background", Nucl. Instrum. Meth. Phys. Reasearch. A **349**, 407-411, (1994).

P. Kozma, R. Bajgar, and P. Kozma Jr., "Radiation resistivity of large tungstate crystals", Rad. Phys. Chem., **59**, 377-380, (2000).

G. F. Knoll, *Radiation detection and measurement*, Wiley, second edition, 1989.

F. A. Kroger , *Some Aspects of the Luminescence of Solids*, Elsevier Publ. Co., Amsterdam,1948.

M. J. J. Lammers, G. Blasse and D. S. Robertson, "The luminescence of cadmium tungstate," Phys. Stat. Sol. A- Appl. Research **63**, 569-572 (1981).

T.T. Monajemi, S. Steciw, B. G. Fallone and S. Rathee, "Modelling scintillator-photodiodes as detectors for megavoltage CT," Med. Phys. **31** (5), 1225-1234, (2004).

M. Montecchi and Q. Ingram, "Study of some optical glues for the Compact Muon Solenoid at the large hadron collider of CERN", Nucl. Instrum. Meth. in Phys Res. A **465**, 329-345 (2001).

D. J. Morell, J. S. Cantrell., and L.L. Y. Chang, "Phase-relations and crystal structure of Zn and Cd tungstates," J. American Ceramic Society **63**, 261-264 (1980).

G. Rizzoni, *Principles and Applications of Electrical Engineering,* 3rd Ed. (McGraw-Hill, 2000).

http://sales.hamamatsu.com/; "Photodiode Technical Information"

www.nist .gov/ PhysRefData; "NIST: The National Institute of Standards and Technology website"

R.Y. Zhu, D.A. Ma and H. Newman, "Scintillating Crystals in a Radiation environment," Nuclear physics B(Proc. Supp) **44**, 547-556 (1995).

Chapter 3

The Bench-top System: A. Detector Characterization

In the first phase of this project (Monajemi *et al.*, 2004) we investigated the results of modeling an eight element array of scintillation-photodiode detectors at MV energies and showed that an array of 10 mm thick (in the direction of the incoming beam) $CdWO_4$ scintillation crystals coupled to silicon photodiodes provides ~19% and ~26% $DQE(0)$ in 6 MV and 1.25 MeV beams, respectively. The details of the x-ray/γ-ray and optical Monte Carlo simulations and experiments are provided elsewhere (Monajemi *et al.*, 2004) and are not included here. For the second phase of this project, we have fabricated a 1D array consisting of 80-elements (≡10 of the previously investigated array) containing $CdWO_4$ and Si photodiodes, which are arranged on an arc with a radius of 110 cm. The incident x-ray beam was collimated to a fan beam and a rotary stage was added to create a small bench top third generation CT scanner. In a third generation CT scanner (see figure 4.1), the x-ray source and detectors rotate around the patient simultaneously. The x-ray beam, collimated into a fan, is wide enough to encompass the patient being scanned. For a given source-detector position, detectors provide signals that are used to calculated the beam attenuation along diverging rays from the source. The collection of attenuation measurements at one source position is known as a fan-beam projection. In the prototype system discussed in this work, the source and detectors are held stationary and the objects being scanned are rotated to collect the fan-beam projections around 360°. The system has run reliably except for an initial problem with the detector boards. It was noticed very early in the experimental stage that the analog switches on the detector boards are sensitive to leakage radiation

through the accelerator jaws. Therefore, we manufactured extra shielding blocks to protect the detector board electronics. It should also be noted that the detector boards have a practical limitation in that the change in detector gain required between the 6 MV and Co^{60} experiments was obtained by physically replacing the resistors in the feed back loop of the amplifiers (see figure 3.4). Therefore, experiments could not easily be conducted on both 6 MV and Co^{60} units. Most of the experiments in this chapter were thus performed using a 6 MV photon beam.

The design of the detector electronics, data acquisition timing control, data multiplexer unit, rotary stage control, and data acquisition system of this prototype MVCT are provided in this chapter. In addition, the linear system theory of detector characterization, and the associated experimental investigations, which were performed using pulsed x-ray (6 MV, 600C, Varian Medical Systems, Palo Alto, Ca) radiation, are presented. To characterize the detector we measured the detector linearity with respect to dose rate, attenuation of a 6 MV beam by solid water, the pre-sampling modulation transfer function, MTF_{pre}, noise power spectrum, NPS ,and detective quantum efficiency, DQE. In addition, the effects of a large radiation dose delivered to the detector on its absolute signal were investigated in order to study the combined radiation damage of $CdWO_4$ and photodiodes using a continuous γ-ray beam (Co^{60}, 780E, Nucletron, Kanata, Ontario). It should be noted that MTF_{pre} was not measured in our previous work (Monajemi *et al.*, 2004), and the NPS measurement in the 6 MV beam was not possible for the 8-element array due to the unacceptably large pulse-to-pulse fluctuations.

A. Instrumentation

Designing and building this detector was the focus of the MSc work of D.Tu (2005). For the sake of completeness, a description of the major functional components of the system is presented here. The details of the associated circuitry can be found in D.Tu's thesis (2005).

i. Detector Array

A picture of the MVCT system is shown in figure 3.1. Objects to be imaged are rotated by a precision rotating stage (200RT, Daedal Division, Parker Hannifin Corp, Irwin, PA) that is driven by a stepper motor (ZETA57-83, Compumotor Division, Parker Hannifin Corp, Rohnet Park, CA). The rotary stage makes one complete revolution in 22.5 seconds. The frequency of the data collection cycle is set to 694 and 137 Hz (linear accelerator pulse frequency), resulting in 15617 and 3083 data points for each detector per 360° rotation, respectively for Co^{60} and 6 MV beams. The beam is collimated to a thin fan beam so that at 110 cm (= the radius of curvature of detector arc) away from the source, the beam covers the detector exactly.

The 80-channel detector consists of ten separate circuit boards, each containing an eight-element 10 mm tall $CdWO_4$ scintillator array in contact with a 16-element photodiode array (S5668-02 Hamamatsu Corporation). The active area of each photodiode element is 1.175 x 2 mm^2 with 0.4 mm spacing between neighbouring photodiodes; each crystal (2.75 x 8 mm^2 cross section) illuminates two consecutive photodiode elements (1.175 x 2 + 0.4 = 2.75 mm) as shown in figure 3.2. A reflective foil is placed underneath the crystals within the area that exceeds the area of the two photodiodes in order to reflect some of the light back into the crystal in order to improve signal detection (Berndt *et al.,* 2000). The same eight-element detector blocks were used earlier for an ^{192}Ir brachytherapy source based CT prototype (Berndt *et al.*, 2000). In a given detector block sitting on a single electronic board (see figure 3.2b), eight 2.75 x 8 x 10 mm^3 $CdWO_4$ crystals are bonded together in white gelcoat (Ashland Chemical Type 1 polyester gelcoat), commonly used as the outer coat for fibreglass boats. The crystals were spaced 0.4 mm apart, which is the same as the dead space in-between the photodiode elements. The same distance was also maintained between the ten consecutive detector boards while placing the boards on an arc with a radius of 110 cm, so that the detector pitch is 3.15 mm throughout the 80-element array. There is an air-gap of average width 0.4 mm between

consecutive 8-element detector blocks. The consequences of these air gaps for image artefact creation are discussed in the next chapter.

Figure 3.1: The detector array in a typical imaging geometry.

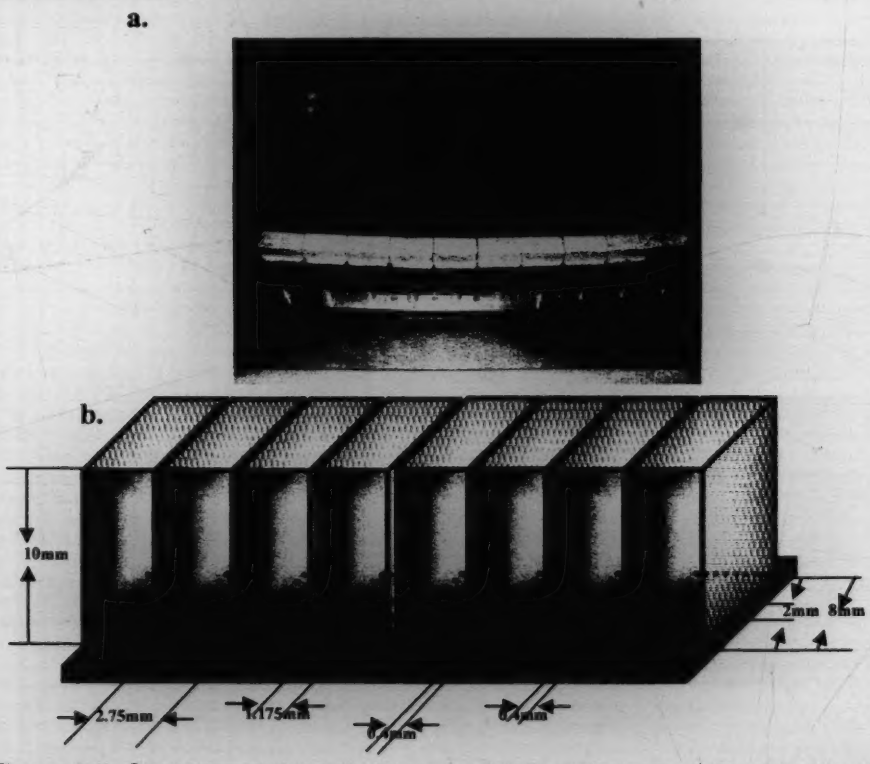

Figure 3.2: Geometry of the detector array: (a) A photograph of the detector array. The 80-element array consists of ten separate bonded 8-element crystal blocks. While the spaces between neighbouring crystals on one block are filled with *gelcoat*, there are air-gaps between separate blocks. (b) Each bonded 8-element crystal block consists of crystals of size 2.75 x 8 x 10 mm^3. Two consecutive crystals are 0.4 mm apart. Each crystal is in contact with two photodiodes. The size of each photodiode is 1.175 x 2 mm^2; the spacing between two photodiodes is 0.4 mm. Each adjacent pair of photodiodes in contact with one crystal is coupled to give one signal per crystal.

ii. System Overview

Figure 3.3 shows the block diagram of the system along with arrows indicating control signals and data flow between five sub-systems: data acquisition timing control; detector electronics; analog multiplexer; precision rotary stage; data acquisition board. The data acquisition board contains a single 16-bit analog to digital (A-to-D) converter. Therefore the data from the 80 element detector array is time-multiplexed on a single data line which is connected to the A-to-D board. The user interface to the data collection, display and storage is implemented in LABVIEW graphical programming language (National Instruments, Austin, TX).

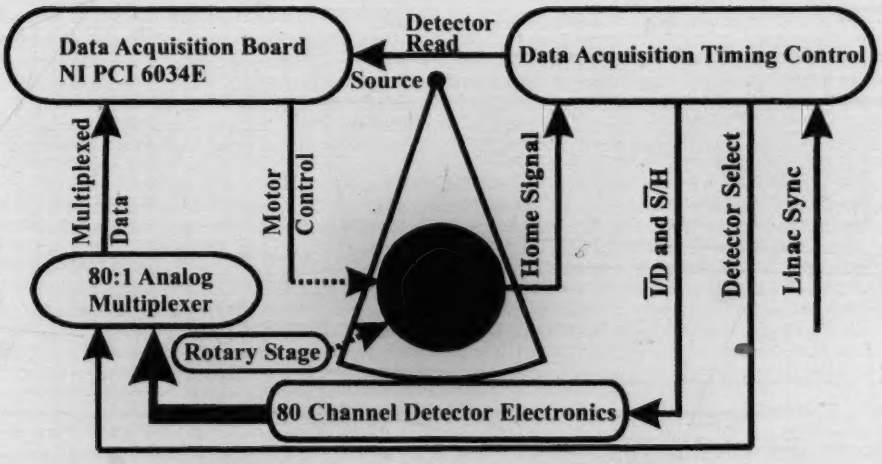

Figure 3.3: Block diagram showing the five sub-systems and data flow of the prototype MVCT system. The detectors are arranged along an arc at a distance of 110 cm from the source, and the objects to be imaged are placed on the rotary stage.

Each eight-element detector array consists of eight parallel analogue signal processing channels, one for each individual detector. Figure 3.4 shows the components of the detector assembly board for one channel. Each channel consists of two photodiodes, a gated integrator (Texas Instruments TL074C op-amp; Temic DG442 analogue switch), a sample and hold ($\overline{S}/H$) circuit (Analog

Devices SMP-04), and an 8-to-1 multiplexer (MUX) (Fairchild semiconductor, CD4501BC) which is not shown in this figure. A fraction of scintillation photons created in the crystals is incident on the photodiodes producing electrical current which is integrated. The integrated circuit accumulates this current for a certain time and produces a voltage signal. The $\overline{S}/H$ circuit will hold the voltage signal for a certain time before routing it to an 8:1 analog multiplexer. During the hold period, the multiplexer in each 8-element detector array multiplexes the data from the channels into a single data line. The multiplexer for the entire system consists of two additional multiplexing steps of 10:2 and 2:1; the three multiplexing levels steps result in 80:1 multiplexing.

The precision rotary stage (200RT, Daedal division, Parker Hannifin Corp, USA) is rotated by a stepper motor (ZETA 57-83, Compumotor Division, Parker, USA). The stepper motor is controlled via the digital port and a programmable pulse generator from the data acquisition board. The home switch on the motor is normally closed. When the motor rotates to the zero position, the home switch is opened which signals the data acquisition board to start collection of data.

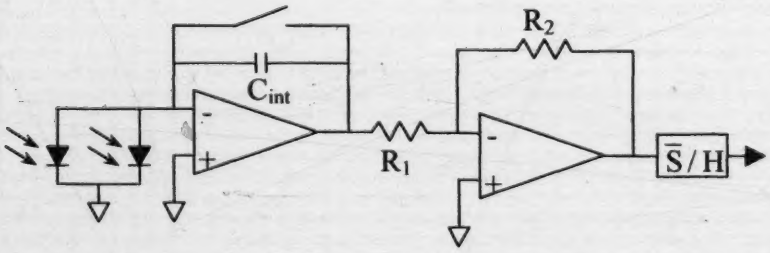

Figure 3.4: The detector electronics for a single element consists of a gated integrator (C_{int} = 1 nF), an amplifier (gain = R_2/R_1) and a sample-and-hold circuit. The gain is set to 1 and 47, respectively for 6 MV and Co^{60} beams.

iii. Data Acquisition Timing Control (DATC)

The timing diagram for the various signals is shown in figure 3.5. The DATC generates timing control signals for the detector electronics ($\overline{I}$/D and $\overline{S}$/H), 80:1 analog multiplexer (a 7-bit binary number for detector selection), and A-to-D conversion clock ("Detector Read" in figure 3.5). Data acquisition is initiated by a home signal generated by a magnetic switch on the rotary stage. The rate of data acquisition is determined by a trigger signal that is the "Sync" signal for the 6 MV linear accelerator (T_{CYCLE} = 7.3 ms) or is derived from an independent clock for Co^{60} (T_{CYCLE} = 1.44 ms). The low voltage "Sync" signal is available at the front of the control console in all Varian linear accelerators outside the treatment room. This signal was connected to our "data acquisition timing control" system through an opto-isolator circuit to reduce interference noise. Immediately following the trigger, $\overline{I}$/D is asserted which opens the analogue switch for T_{INT} = 0.8 ms to integrate the photo-current. The $\overline{S}$/H signal is asserted to hold the integrated signal just prior to discharging the capacitors (by de-asserting $\overline{I}$/D) in the gated integrators i.e. T_{SAMPLE} = 0.7 ms. The integrated signals for all the detector channels are held for T_{HOLD} = 0.64 ms for Co^{60} and 4.0 ms for 6 MV, which allows the A-to-D converter to read the data for all 80 channels at a rate of $f_{A\text{-}to\text{-}D}$ = 125 kHz for Co^{60} or 20 kHz for 6 MV. During this acquisition, the 7-bit binary number is also incremented synchronously with $f_{A\text{-}to\text{-}D}$ to select the multiplexed output for detectors 1 through 80.

Since the data collection is synchronized with sync pulses from the linear accelerator, each data point represents the radiation detected per pulse. In general, the dose rate control mechanism of the C-series linear accelerators from Varian decides if a given "Sync" pulse will produce radiation or not. For example, with a setting of 250 monitor units (MU; 1 MU = unit charge in monitor chambers ≡ 1 cGy of radiation dose to water for 10 x 10 cm^2 field at the depth of maximum dose at 100 cm from the source) per minute, 5 out of 6 "Sync" pulses on average are associated with a radiation pulse. Therefore, the first step in processing the data is to discard the non-radiation pulses. This step is not required for the

continuous Co^{60} radiation case. For all the measurements the average signal of each channel in the absence of radiation, i.e. the dark signal, is subtracted from the collected data.

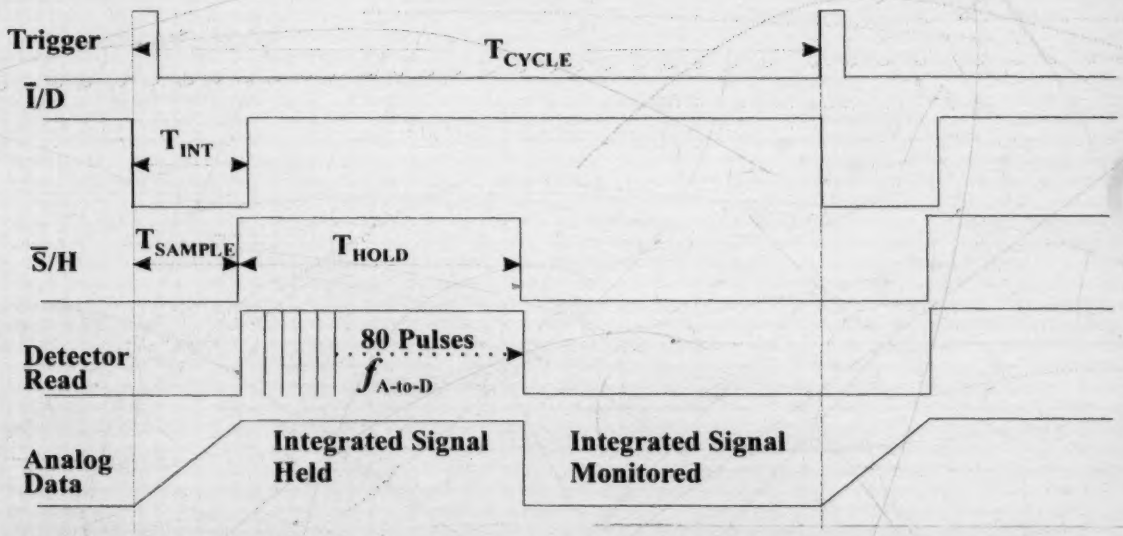

Figure 3.5: The timing diagram of the control signals: $\bar{I}$ /D = Integrate-discharge control of the gated integrator; $\bar{S}$ /H = sample-and-hold control; Detector Read = convert clock for the A-to-D converter. The trigger signal is either the "Sync" signal of the pulsed radiation (6 MV) or derived from an independent clock for continuous radiation (Co^{60}).

B. Theory

i. Linear and shift-invariant (LSI) systems

Analyzing and predicting the response of an imaging system requires the system to be *linear*. This requirement is essentially met when the output of the system is linearly proportional to the input. If a system has a transfer characteristic described by $S\{\}$ so that for an input $h(x)$ the output is $S\{h(x)\}$, then for any two inputs $h_1(x)$ and $h_2(x)$, the system is linear if and only if (Cunningham, 2000):

$$S\{h_1(x)+h_2(x)\} = S\{h_1(x)\}+S\{h_2(x)\}, \tag{3.1}$$

and for any real scalar a,

$$S\{ah(x)\} = aS\{h(x)\}. \tag{3.2}$$

In general real systems are not completely linear. However, with most systems there exists a range of inputs for which the system is either linear or linearizable.

If the delta function, $\delta(x - x_0)$, is presented as an input to a linear system, the corresponding output, which is referred to as the impulse response function (irf) is defined as (Cunningham, 2000):

$$irf(x, x_0) = S\{\delta(x - x_0)\}. \tag{3.3}$$

Linearity also implies that:

$$S\{\delta(x - x_1) + \delta(x - x_2)\} = irf(x, x_1) + irf(x, x_2). \tag{3.4}$$

In two dimensions the irf is referred to as the point spread function (psf).

An imaging system must also be shift-invariant before a Fourier based analysis of image performance can be applied. A system is shift-invariant if the shape of the irf is the same regardless of the location of the input, that is:

$$irf(x, x_0) = irf(x - x_0); \ \ for\ any\ x_0. \tag{3.5}$$

Due to the presence of septa material between the scintillator elements, segmented scintillation detectors are not shift invariant; i.e. the system has a different shaped impulse response function depending on where the input pencil-beam is placed. In the discussion that follows, it is shown that despite the lack of complete shift-invariance in segmented scintillation detectors, Fourier analysis with some reasonable qualifications can still be applied to segmented detectors.

ii. MTF_{pre}

The modulation transfer function is a measure of the spatial resolution of an imaging system and it characterizes the spatial frequency dependent, relative transfer of the deterministic input signal to the output. By definition in an LSI system (Cunningham, 2000):

$$MTF(u,v) = |2DFT\{psf(x,y)\}|, \tag{3.6}$$

where $2DFT$ is the two dimensional Fourier transform and $psf(x,y)$ is the point spread function which is the spatial response in 2D of the detector to a point *x*-ray input as discussed above. In practice, the experimental measurement of MTF is performed in 1D by measuring the line spread function (lsf) from the response of the imaging system either to a long narrow slit object, or by differentiating the response to an abrupt edge in the object. The lsf is obtained from the psf as follows (Cunningham, 2000):

$$lsf(x) = \int_{-\infty}^{\infty} psf(x,y)dy. \tag{3.7}$$

The one dimensional Fourier transform of the lsf gives the MTF in 1D as follows:

$$\left| \int_{-\infty}^{\infty} lsf(x)e^{-2\pi ixu}dx \right| = \left| \int_{-\infty}^{\infty} \int_{-\infty}^{\infty} \{psf(x,y)dy\}e^{-2\pi ixu}dx \right| \tag{3.8}$$
$$= |2DFT\{psf(x,y)\}|_{v=0}$$
$$= MTF(u,0)$$

Therefore, $MTF(u) = |FT\{lsf(x)\}|$.

The formation of the deterministic part of the signal in a 1D LSI detector is shown in figure 3.6. A relevant example of such a detector is a homogeneous sheet of a scintillator, placed on top of an array of photodiodes with elements of

size a_x in x-direction. The photodiode elements all have identical sensitivity and amplification value; the centers of the photodiodes are placed at a distance of x_0 in x-direction from each other. Since the fill factor of the photodiodes is generally less than unity, i.e. there is a small space in between consecutive photodiode elements that is not optically sensitive, $a_x \leq x_0$. In the spatial domain, the incoming distribution of quanta , $h(x)$, is convolved with the impulse response function of the scintillator $irf(x)$ to produce a continuous optical signal distribution $q(x)$ incident on the photodiodes. This continuous signal in turn is convolved with the aperture function of the photodiodes which, in this figure, is assumed to be a perfect rectangle with height k and width a_x. The signal $d(x)$ is referred to as the pre-sampling signal, and, by definition, it is the signal formed in the detector immediately prior to sampling. The pre-sampling MTF_{pre} is defined as the Fourier transform of the pre-sampling signal $d(x)$ in response to $h(x) = \delta(x)$ and it is given as the product of the scintillator MTF, $T(u)$ which is the Fourier transform of $irf(x)$, and the photodiode sampling aperture MTF which for the case of the detector shown above equals $ka_x \sin c(\pi a_x u)$. Sampling is represented by multiplying the pre-sampling signal by the comb function with spacing x_0 in the x direction of the spatial domain.

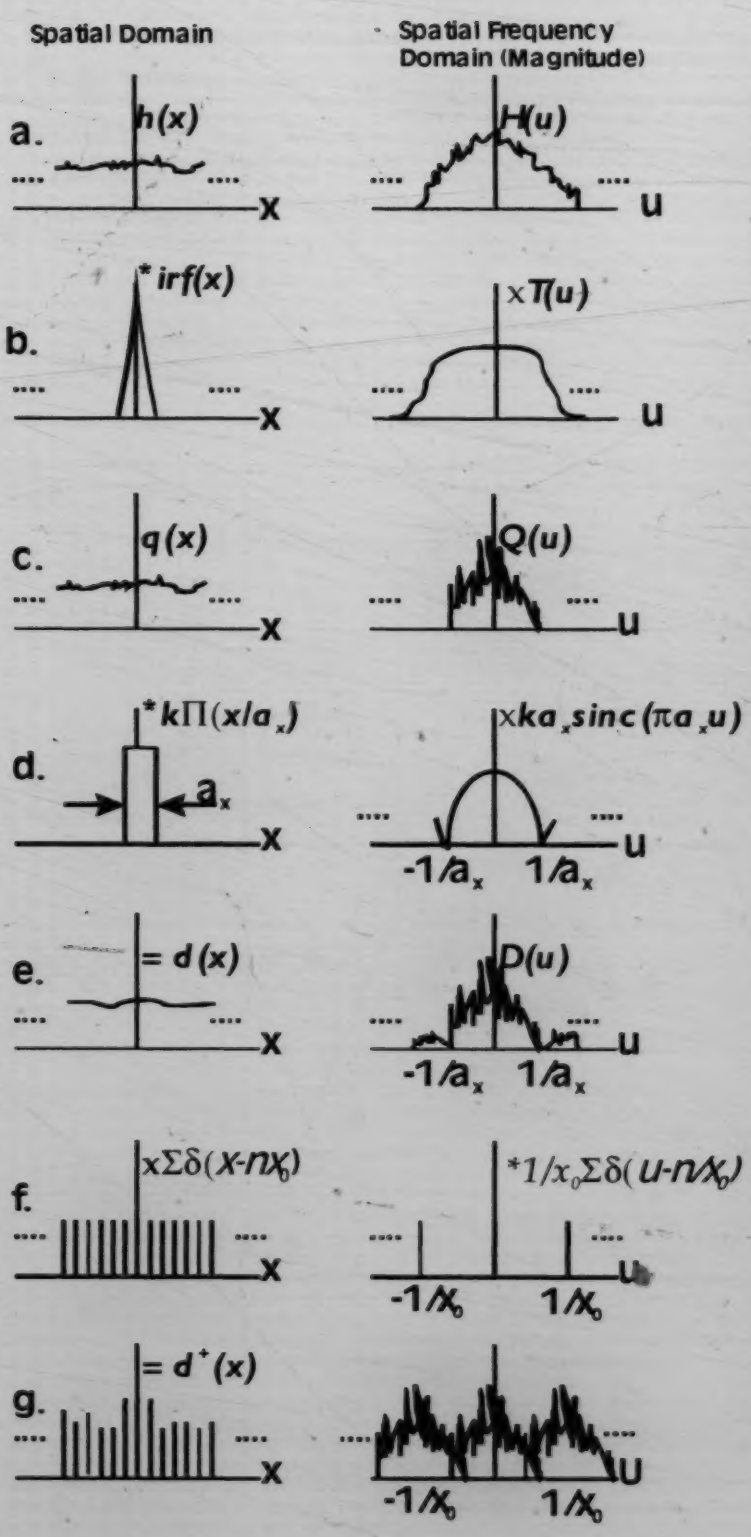

Figure 3.6: Steps involved in the formation of the deterministic part of the signal in a homogenous slab of a scintillator sitting atop a 1D array of photodiodes.(a)-(c): In the spatial domain, the incoming distribution of quanta , $h(x)$, is convolved with the impulse response function of the scintillator $irf(x)$ to produce a continuous optical signal distribution $q(x)$ incident on the photodiodes.(c)-(e) This continuous signal in turn is convolved with the aperture function of the photodiodes which in this figure is assumed to be a perfect rectangle with height k and width a_x. The signal $d(x)$ is referred to as the pre-sampling signal, and, by definition, it is the signal formed in the detector immediately prior to sampling. The pre-sampling MTF_{pre} is defined as the Fourier transform of the pre-sampling signal $d(x)$ in response to $h(x) = \delta(x)$ and it is given as the product of the scintillator MTF, $T(u)$ which is the Fourier transform of $irf(x)$, and the photodiode sampling aperture MTF which for the case of the detector shown above equals $ka_x \sin c(\pi a_x u)$. (e)-(g) : Sampling is represented by multiplying the pre-sampling signal by the comb function with spacing x_0 in the x direction of the spatial domain.

As mentioned above, a problem arises when applying the concept of MTF_{pre} to segmented detectors. Due to the presence of septa material between the scintillator elements, the system is no longer shift invariant; i.e. the system gives a different signal depending on where the input beam is placed. It has been shown (Sawant *et al.*, 2005) that as long as each scintillator element is exactly registered to the underlying photodiode array, MTF_{pre} is still shift invariant under certain conditions explained below. The signal in the $(n,m)^{th}$ photodiode element, $d_{n,m}$, is equal to the amplification value, *k*, which we choose to represent the combination of the electronic gain (signal per electron) and the sensitivity of the photodiode element (electrons per optical photon), multiplied by the total number of optical photons incident on that photodiode element, $q_{n,m}$:

$$d_{n,m} = kq_{n,m}, \tag{3.9}$$

where $q_{n,m}$ is equal to the integral -over the area of the photodiode element- of the distribution of optical quanta exiting the corresponding scintillator element at (x'', y''), i.e. $q_{opt}(x'', y'')$ as follows:

$$q_{n,m} = \int_{x''=nx_0-a_x/2}^{nx_0+a_x/2} \int_{y''=my_0-a_y/2}^{my_0+a_y/2} q_{opt}(x'', y'')dx''dy''. \tag{3.10}$$

If $h(x', y')$ represents the spatial distribution of x-ray quanta incident on the detector, and $p(x'', y''; x', y')$ is the probability that unit x-ray quanta incident at(x', y'), on average, results in *L* optical photons exiting from the scintillator at (x'', y''), the spatial distribution of optical quanta exiting the scintillator can be written as:

$$q_{opt}(x'',y'') = L\int_{-\infty}^{\infty}\int_{-\infty}^{\infty} h(x',y')p(x'',y'';x',y')dx'dy', \tag{3.11}$$

Equation (3.11) combines a number of steps into a single superposition integral. In practice, an incident x-ray quanta results in a 3D energy deposition within the scintillation material. Only a fraction of optical photons, created due to the x-ray energy deposition at each point in the 3D crystal, exits the scintillation material depending upon the optical self-absorption within the crystal bulk, and opacity and reflectivity of the septa material. The signal from the *(n,m)*th photodiode element is therefore given by:

$$d_{n,m} = kL\int_{x''=nx_0-a_x/2}^{nx_0+a_x/2}\int_{y''=my_0-a_y/2}^{my_0+a_y/2}\int_{x'=-\infty}^{\infty}\int_{y'=-\infty}^{\infty} h(x',y')p(x'',y'';x',y')dx'dx''dy'dy''. \tag{3.12}$$

The equation above can be rewritten as:

$$d_{n,m} = kL\int_{x'=-\infty}^{\infty}\int_{y'=-\infty}^{\infty} h(x',y')\int_{x''=nx_0-a_x/2}^{nx_0+a_x/2}\int_{y''=my_0-a_y/2}^{my_0+a_y/2} p(x'',y'';x',y')dx''dy''dx'dy'. \tag{3.13}$$

The nested integral over (x'',y'') represents the spatial integration of optical quanta by the *(n,m)*th photodiode element and gives the sensitivity profile of that element to a small x-ray beam irradiating across the entire detector (figure 3.7). Since all the scintillation elements are identical and exactly registered to the photodiode array, the profile is a function of the distance between (x',y') and the element centers only. Therefore this sensitivity profile can be expressed as follows:

$$p_a(nx_0-x',my_0-y') = \int_{x''=nx_0-a_x/2}^{nx_0+a_x/2}\int_{y''=my_0-a_y/2}^{my_0+a_y/2} p(x'',y'';x',y')dx''dy''. \tag{3.14}$$

Therefore,

$$d_{n,m} = kL \int_{x'=-\infty}^{\infty} \int_{y'=-\infty}^{\infty} h(x',y') p_a(nx_0 - x', my_0 - y') dx'dy'$$
$$= d(x,y)\Big|_{x,y=nx_0,my_0} = kL \int_{x'=-\infty}^{\infty} \int_{y'=-\infty}^{\infty} h(x',y') p_a(x-x', y-y') dx'dy'. \tag{3.15}$$

The double integral is recognized as the convolution operator and $d(x,y)$ is the detector pre-sampling signal. The pre-sampling signal is continuous only for virtual detector elements that are centered at a continuum of (x,y) locations and yet have a finite aperture area $a_x a_y$. Therefore, this function only has a physical meaning for (x,y) locations equal to (nx_0, my_0). The pre-sampling detector line spread function in the x direction is defined as:

$$LSF_{pre}(x) = \int_{y=-\infty}^{\infty} p_a(x,y) dy. \tag{3.16}$$

The $MTF_{pre}(f)$ is the Fourier transform of $LSF_{pre}(x)$ described above. In practice the LSF_{pre} in 2D detectors is usually obtained by using the "slanted slit method" (Fujita *et al.*, 1992). In this method, a narrow beam is placed on the x-y entrance face of the detector with a slight angle with respect to one of the axes. Figure 3.8 shows how by using this method LSF_{pre} is assembled. In the Materials and Methods section we show how this method was modified slightly and applied to our 1D detector.

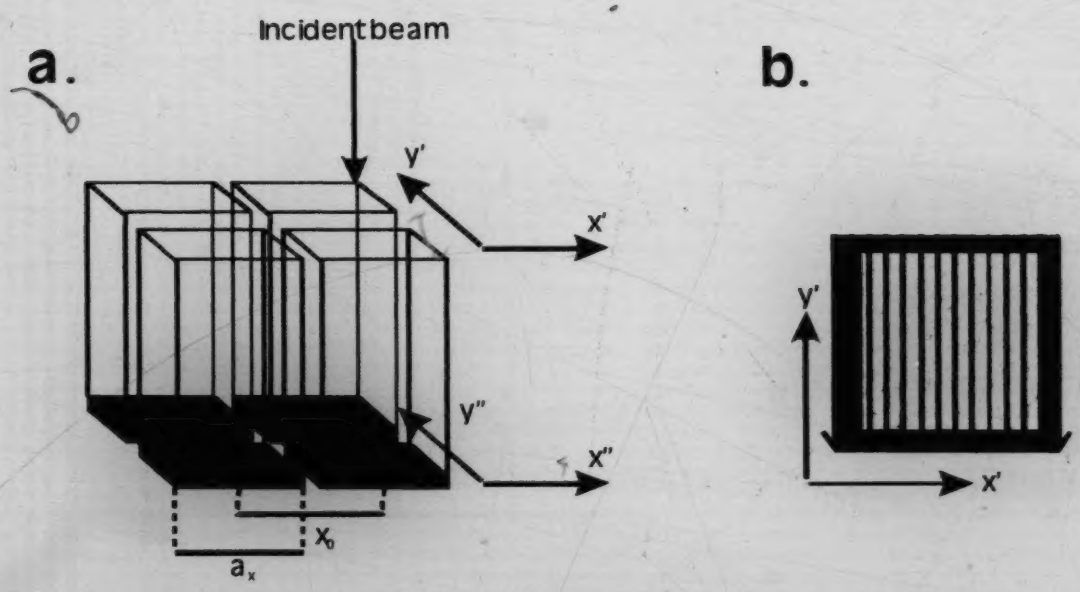

Figure 3.7: (a) The geometry used in equations 3.9 to 3.16. (b) In equation 3.13, the nested integral over (x'', y'') represents the spatial integration of optical quanta by the $(n,m)^{th}$ photodiode element and gives the sensitivity profile of that element to a small x-ray beam irradiating across the entire element. The arrows in this figure demonstrate the concept of "a small x-ray beam being scanned across the entire detector" for one element and its surrounding septa material.

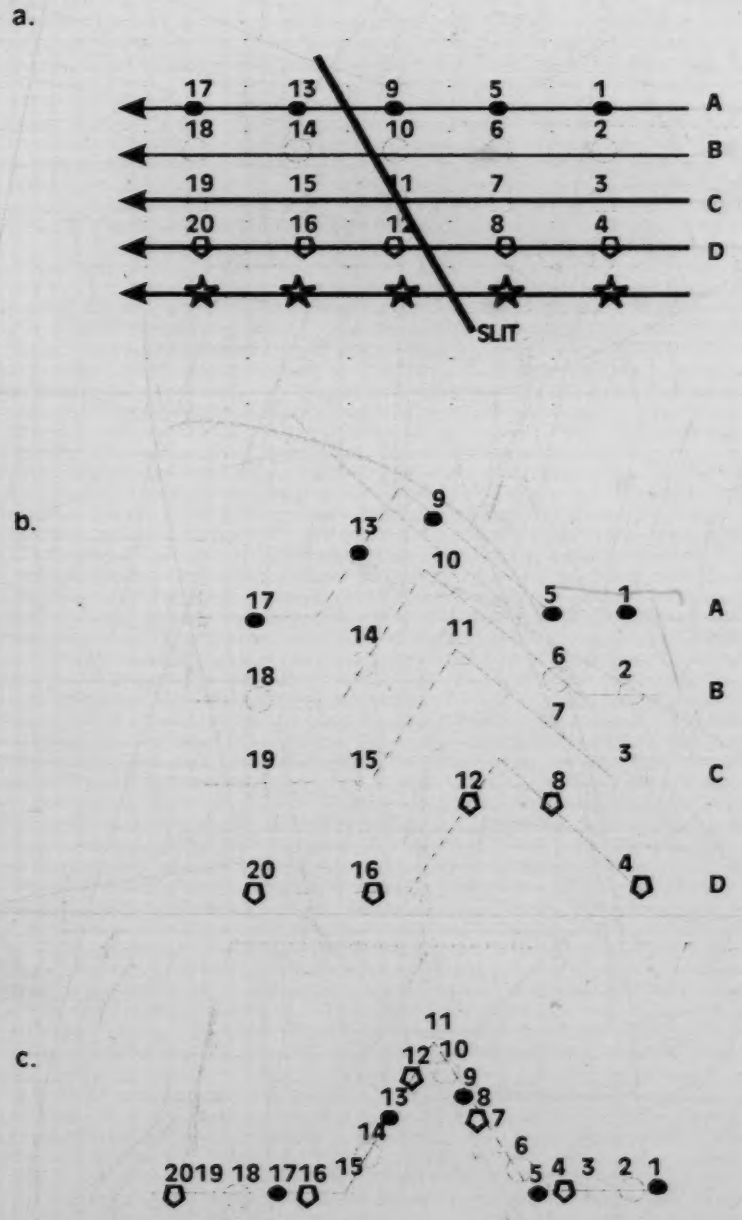

Figure 3.8: Finding the presampling *LSF* (c) by placing a slanted slit of beam (a) on a 2D detector and reading each row of the detector (b) (Fujita et al., 1992).

iii. *NPS*

The *MTF* describes how the deterministic part of the input is transferred to the output, similarly the *NPS* describes how the stochastic part of the input is transferred to the output. The noise power spectrum is defined as the Fourier transform of the autocorrelation function. The autocorrelation function, $C(x)$, defined over a length L for a linear, wide sense stationary (i.e. a random process which has at least the mean and the autocorrelation invariant in x) and continuous random process is written as follows (Williams *et al.*, 1999; Dainty and Shaw, 1974):

$$C(x) = \lim_{L\to\infty} \frac{1}{L} \int_{-L/2}^{L/2} d(x+\tau) d^*(\tau) d\tau, \tag{3.17}$$

where $d(x)$ is the intensity value in an image at position x, and $d^*(x)$ is its complex conjugate which, since $d(x)$ is real, is equal to $d(x)$. The Fourier transform of $C(x)$ is given by (Williams *et al.*, 1999; Dainty and Shaw, 1974):

$$\begin{aligned} S(u) &= \int_{-\infty}^{\infty} C(x) e^{-2\pi i x u} dx = \lim_{L\to\infty} \frac{1}{L} \int_{-L/2}^{L/2} d^*(\tau) e^{+2\pi i \tau u} \int_{-\infty}^{\infty} d(x+\tau) e^{-2\pi i x u} dx [e^{-2\pi i \tau u}] d\tau \\ &= \lim_{L\to\infty} \int_{-L/2}^{L/2} d^*(\tau) e^{+2\pi i \tau u} \int_{-\infty}^{\infty} d(\sigma) e^{-2\pi i \sigma u} d\sigma d\tau = \lim_{L\to\infty} \frac{1}{L} \int_{-L/2}^{L/2} d^*(\tau) e^{+2\pi i \tau u} d\tau \, D(u) \end{aligned} \tag{3.18}$$

Where $D(u)$ is the Fourier transform of $d(x)$. Therefore,

$$S(u) = FT\{C(x)\} = \lim_{L\to\infty} \frac{1}{L} |D(u)|^2. \tag{3.19}$$

Extending the equation to two dimensions X and Y we get:

$$S(u,v) = FT\{C(x,y)\} = \lim_{X,Y\to\infty} \frac{1}{XY}|D(u,v)|^2. \tag{3.20}$$

where the Cartesian coordinates in the spatial frequency domain are represented as (u,v).

In equation 3.20 we are assuming that $C(x,y)$ is the "true" autocorrelation function of the underlying noise process in 2D detector output. Assume that we use a *linear* aperture with a *PSF* of $a(x,y)$ (or $T(u,v)$ in the Fourier domain) to measure the "true" autocorrelation function (e.g. using a densitometer to read optical density fluctuations of film). In this case $d(x,y)$ is the "true" pixel value and the "measured" pixel value $d'(x,y)$ is equal to (Williams *et al.*, 1999; Dainty and Shaw, 1974):

$$d'(x,y) = \int_{-\infty}^{\infty}\int_{-\infty}^{\infty} d(x_1,y_1)a(x-x_1,y-y_1)\, dx_1 dy_1, \tag{3.21}$$

and at another location:

$$d'(x+\xi,y+\eta) = \int_{-\infty}^{\infty}\int_{-\infty}^{\infty} d(x_2,y_2)a(x-x_2+\xi,y-y_2+\eta)\, dx_2 dy_2. \tag{3.22}$$

Thus the measured autocorrelation function is written as:

$$C'(\xi,\eta) = \lim_{X,Y\to\infty} \int_{-X/2}^{X/2}\int_{-Y/2}^{Y/2} d'(x,y)d'(x+\xi,y+\eta)\, dxdy. \tag{3.23}$$

From equations 3.21-3.23 it follows that the measured autocorrelation function is equal to the "actual" autocorrelation function convolved twice with the *PSF* of the measuring system. In the Fourier domain this statement is expressed as (Williams *et al.*, 1999; Dainty and Shaw, 1974):

$$S'(u,v) = S(u,v)|T(u,v)|^2. \tag{3.24}$$

Since the "measured" autocorrelation function and the "measured" noise power spectrum $S'(u,v)$ are Fourier pairs, we have:

$$C'(x,y) = \int_{-\infty}^{\infty}\int_{-\infty}^{\infty} S(u,v)|T(u,v)|^2 e^{+2\pi i(ux+vy)} du dv. \tag{3.25}$$

Measured along $v = 0$ the above equations becomes:

$$C'(x) = \int_{-\infty}^{\infty}\left(\int_{-\infty}^{\infty} S(u,v)|T(u,v)|^2 dv\right) e^{+2\pi i ux} du. \tag{3.26}$$

We already know that in 1-D:

$$C'(x) = \int_{-\infty}^{\infty} S'(u) e^{2\pi i ux} du \tag{3.27}$$

Comparing equations 3.26 and 3.27 yields:

$$S'(u) = \int_{-\infty}^{\infty} S(u,v)|T(u,v)|^2 dv. \tag{3.28}$$

Equation 3.28 relates the "measured" 1D NPS to the "true" 2D *NPS*.

Characterization of $S(u,0)$, i.e. a slice through the "true" 2D *NPS*, is usually done by the synthesized slit method. Assume that the noise pattern is scanned with a slit which is infinitely long perpendicular to the scan and infinitely narrow in the scan direction, i.e. an ideal slit. The scanning aperture can be described by the delta functions (Dainty and Shaw, 1974):

$$a(x,y) \equiv \delta(x); \qquad T(u,v) \equiv \delta(v). \tag{3.29}$$

From equation 3.28 it follows that:

$$S'(u) = S(u,0). \tag{3.30}$$

In practice a long narrow slit is scanned in steps in one direction over the image. The average of pixel values over the length of the slit is recorded to create a1D data series. The synthesized slit *NPS* for an infinitely long 1D data series in the x direction is calculated according to equation 3.28 (Williams et al., 1999):

$$S_{SS}(u) = \int_{-\infty}^{\infty} S(u,v)|T(u,v)|^2 \, dv, \tag{3.31}$$

where $|T(u,v)|^2$ is the transfer function of the slit, and $S_{SS}(u)$ is the 1D *NPS* measured by using the synthesized slit method. If the slit is rectangular with x-dimension w and y-dimension L, then the point spread function of this practical slit is:

$$a(x,y) = \left(\frac{1}{w} rect \frac{x}{w}\right)\left(\frac{1}{L} rect \frac{y}{L}\right) \tag{3.32}$$

$$T(u,v) = FT\{a(x,y)\} = sinc(wu)\, sinc(Lv). \tag{3.33}$$

Therefore,

$$S_{SS}(u) = sinc^2(wu) \int_{-\infty}^{\infty} S(u,v) sinc^2(Lv) dv. \tag{3.34}$$

If the slit width is narrow, then $\sin c(wu) \approx 1$. Even if the slit width is not narrow enough, the correction for this factor is straightforward. In a digital system, the synthesized slit is comprised of 1 x N_L pixels which sample the *NPS* using a line of N_L delta functions which are placed at an interval in the scan direction equal to x_0. Thus, in digital systems, w = 1 pixel and $\sin c(wu) = 1$. Also, as $L \to \infty$, $sinc^2(Lv)$ becomes narrow so that $S(u,v)$ is approximately constant over the range of v near v=0 where $sinc^2(Lv)$ is nonzero:

$$\begin{aligned} S_{SS}(u) &= \int_{-\infty}^{\infty} S(u,v) sinc^2(Lv) dv \\ &\cong S(u,0) \int_{-\infty}^{\infty} sinc^2(Lv) dv = \frac{S(u,0)}{L}. \end{aligned} \tag{3.35}$$

Therefore, the true1D *NPS* is $S(u,0) = L\, S_{SS}(u)$.

Up to now, we have assumed that the detector is a wide sense stationary (WSS) detector. However, a digital detector such as a segmented detector, is no longer WSS. Hence, as was done in the case of MTF_{pre}, we need to justify the use of *NPS*. In a segmented detector such as ours where the scintillator is exactly registered to the underlying photodiode, the pre-sampling signal is invariant to a shift of nx_0; therefore this process represents a wide sense cyclostationary process (WSCS) meaning that the mean and autocorrelation are invariant with shifts of nx_0. For such a WSCS *discrete* random process (Williams et al., 1999):

$$S_d(u) = S(ju_0)$$
$$= \lim_{Nx_0 \to \infty} \frac{1}{Nx_0} \left| x_0 \sum_{n=0}^{N-1} d'(nx_0) e^{-2\pi i[(ju_0)(nx_0)]} \right|^2 \tag{3.36}$$

where N is the total number of pixels in the x direction and u_0 is the distance between two points in the frequency domain.

iv. *DQE*

The detective quantum efficiency gives the effective fraction of incident Poisson-distributed quanta contributing to image signal to noise ratio (SNR). In a digital system it is defined as:

$$DQE(u) = \frac{MTF_{pre}{}^2(u)}{(NPS\ (u)/\bar{d}^2)\varphi} \tag{3.37}$$

where φ is the photon fluence (quanta per mm^2) impinging on the detector and $\bar{d}$ is the average detector signal.

C. Materials and Methods

i. Linearity

a. Detector Response to Dose Rate

This experiment was designed to measure the linearity of the detector with respect to dose rate in a 30.0 x 2.2 cm^2 6 MV photon beam. Since the timing mechanism of the detector is designed to measure the signal proportional to the incident radiation for every pulse, it would have been easier if the beam output per pulse could be varied. However, clinical linear accelerators (600C, Varian Medical Systems, Palo Alto, CA) do not provide the means for varying the dose per pulse in the normal operating mode. In order to vary the dose rate per pulse, the inverse square law was utilized and the source to detector distance (SDD) was varied from 100 cm to 150 cm in 5 cm steps. At each SDD, 2000 data points were collected per detector channel. The mean signal for each detector was

calculated after discarding the non-radiation pulses. The mean detector signal as a function of $(100/SDD)^2$ was fit by linear regression.

b. Attenuation Measurement

The fundamental requirement for a CT detector is to measure the attenuation produced by the scanned object in an accurate and linear manner. Thus, we used our detector array to measure the attenuation of a 6 MV photon beam by solid water. Slabs of solid water (12 slabs each 2 cm thick) were placed on top of the treatment couch in the path of a narrowly collimated 6 MV photon beam (25 x 2.2 cm^2) while the detector was placed under the treatment couch at a SDD of 110 cm. The solid water was placed on the tennis racket part of the couch that negligibly attenuates the 6 MV beam. For each thickness of solid water, one thousand readings per detector channel were acquired and the mean values calculated. The entire experiment was repeated 5 times. The attenuation factor for each solid water thickness was calculated using the following:

$$\lambda = -ln\left(\frac{I_i}{I_0}\right) \tag{3.38}$$

where λ is the attenuation, I_i is the attenuated signal and I_0 is the non-attenuated signal.

A second-order polynomial fit was used to study the effects of spectral hardening (Beam hardening is discussed in the following chapter). A straight line was fit to the first four data points and extrapolated to greater solid water thickness while a second order polynomial was fit to all data points. If these measurements were carried out in a broad beam, the scattered radiation created in the solid water phantom would have introduced non-linearity in the attenuation measurements. We have carried out these measurements using a relatively narrow beam (25 x 2.2 cm^2) which also protects the electronic hardware from radiation damage.

ii. MTF_{pre}

As discussed in the theory section, the shift-invariance of segmented scintillator detectors is maintained for shifts that are integer multiples of pitch as long as crystals and photodiodes are registered which is true for this detector since a crystal covers exactly two photodiodes. Therefore, the classical Fourier techniques can be used for detector system analysis. The *MTF* (not MTF_{pre}) measured previously (Monajemi *et al.*, 2004; Monajemi, 2004) for the 8-element prototype array suffered from significant aliasing due to the large detector pitch of $x_0 = 3.15$ mm. Therefore, the pre-sampling *LSF* and the resulting *MTF* for the 80-element array was measured using the theory described by Fujita *et al.* (1992). With our approach, the *LSF* was over-sampled by a factor of five to minimize aliasing. The measurement procedure is depicted in figure 3.9. A slit beam was centered on one detector element (indicated by co-ordinate '0' in figure 3.9) and the average signal for each detector element was obtained from 10,000 measured pulses. The detector array was then translated to four other positions indicated by -2δ, $-\delta$, δ and 2δ ($\delta = x_0/5$) with respect to the slit beam location, and the data acquisition was repeated. The resulting data were interlaced to give the pre-sampling *LSF*, which was Fourier transformed to obtain the pre-sampling *MTF*.

The experimental setup for measuring the pre-sampling *LSF* is shown in figure 3.10. The detector assembly is placed on a stage that can linearly translate the entire detector assembly with a manual control knob in steps of 0.375 mm. The long lead blocks are placed on their own stage to facilitate the collimation of a slit beam. Extra lead blocks near the source are used to reduce the leakage radiation from the secondary jaws of the accelerator. The slit beam of 0.2 mm width was collimated (accelerator field size = 4 x 4 cm^2) using two 25 cm x 5 cm x 10 cm lead blocks separated by a 0.2 mm thick aluminum shims. The width of the slit was verified by taping an XV film at the detector end of the lead blocks and irradiating for 100 monitor units (MU). The film was then scanned (VXR-16, Vidar Systems Corporation, Herndon, VA) and the full width at half maximum of

the slit image determined to be 0.25 mm. Initially, the slit was placed approximately at the center of detector element '36' and then the translation stage was moved in very small increments until the measured (and corrected) signals in detector elements '35' and '37' were the same; this was taken as the zero position of the slit on detector element '36'. The measured data was divided by the mean signal for each detector obtained in open beam measurements to correct for the element-to-element sensitivity variations. The detector array was moved in 0.63 mm increments by a manually operated translation stage. The entire experiment was repeated six times to determine the experimental uncertainty.

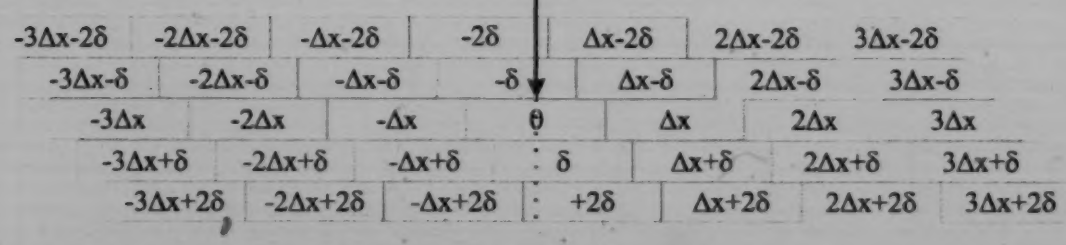

Figure 3.9: Schematic illustrating the arrangement of the slit beam (arrow) and the detector array for the measurement of the pre-sampling *LSF*. Here the columns represent the absolute locations of seven detector elements. The rows indicate a horizontal shift with respect to the beam. x_0 = detector pitch (3.15 mm), δ = detector translation (0.63 mm) with respect to the slit beam. The data measured at five translated positions of the detector array were interlaced to obtain the pre-sampling *LSF* with an effective sampling distance of δ.

Figure 3.10: The photograph shows the experimental set up for the measurement of the pre-sampling *LSF* in a 6 MV beam: the detector array (left) is translated using a linear stage, and long lead blocks (centre) are arranged to obtain the slit-beam of 0.2 mm width. Additional blocks on the right reduce the leakage radiation.

The measured MTF_{pre} is the product of radiation *MTF*, which characterizes the signal spread due to charge particle transport, Compton scattering and optical photon transport within the crystal array, and the detector aperture *MTF*. Importantly, the aliasing in the pre-sampling *MTF*, dominated by the detector aperture, is insignificant since the detector aperture *MTF* is very small for spatial frequencies larger than five times the Nyquist frequency of the detector array, i.e. ≈ 0.8 line pairs per mm (lp/mm).

The pre-sampling *MTF* obtained from this procedure was divided by the detector aperture *MTF* in order to obtain the radiation *MTF*. The detector aperture results from a combination of the photodiode and crystal size effects. As shown in figure 3.2, a single crystal (2.75 mm) sits on top of two photodiodes (2 x 1.175 mm) with a 0.4 mm dead reflector gap in between. Thus, one cannot take crystal size as the detector aperture because there is no direct photo-detector in the 0.4 mm reflector gap. Also, one cannot just take the aperture size of 2 x 1.175 = 2.35 mm as the reflector sends some light back into the crystal; a fraction of this reflected light may fall back on the active photo-detector part and contribute to signal. The effective detector aperture was estimated as $(1/f_0)$ where f_0 is the first zero-crossing spatial frequency in the measured pre-sampling *MTF*. The detector aperture *MTF* is determined as a sinc function using $(1/f_0)$ as the effective aperture width.

To verify that the measured radiation *MTF* did not suffer from aliasing, a Monte Carlo calculation of the radiation *MTF* was performed. Using the XYZDOSnrc user code of the EGSnrc Monte Carlo transport code (Kawrakow *et al.*, 2002), we modeled a slit beam (0.2 mm x 8 mm) of 6 MV photons incident on the center of an 8 mm wide, 30 mm long and 10 mm deep $CdWO_4$ crystal array. The slit beam was incident on the 8 mm x 30 mm face of the crystal array, which was divided into 0.01 mm x 8 mm x 10 mm voxels to reduce aliasing in the simulated *LSF*. The x-ray transport simulation in $CdWO_4$ crystals was also performed in our previous work (Monajemi *et al.*, 2004; Monajemi, 2004); however, the lateral voxel dimension was 3.15 mm instead of 0.01 mm used in

this work. The spectrum of the 6 MV photons was the same as used by Lachaine *et al.* (2001) and shown in figure 5.2. A total of 1 million photon histories were run using the transport parameters AE = ECUT = 0.521 MeV and AP = PCUT = 0.01 MeV.[1] The average energy deposited into chosen voxels of the $CdWO_4$ crystal block was calculated and taken as the radiation *LSF*, which was Fourier transformed to give the radiation *MTF*. The standard deviation in the calculated *LSF* was less than 3% up to 10 mm distance from the slit beam. It should be mentioned that EGSnrc Monte Carlo calculation automatically includes the scattered radiation produced within the detector array.

iii. *NPS*

Ideally, the noise only data can be obtained by subtracting the detector data that are collected during two consecutive pulses. However, the pulse-to-pulse variation of the 6 MV beam prevented an accurate measurement of the *NPS* as noted previously (Monajemi *et al.*, 2004; Monajemi, 2004). Therefore, a periodogram average method (Williams et al., 1999) was used. In this particular approach measuring aperture is that area of the detector which is a long narrow strip in which the longer dimension is segmented with a pitch of x_0 (3.15 mm) and has a finite sensitive width *L* perpendicular to the direction of array. Therefore, the *NPS* can be measured using the synthesized slit technique reviewed by Williams *et al.* (Williams et al., 1999) and discussed in the theory section. It should be noted that the integration at each pixel over the slit width *L* occurs naturally in this case. Based on the discussion of the synthetic slit technique by Williams *et al.* ((Williams et al., 1999) and using equation 3.31 the noise power spectrum of the slit, NPS_{NS}, is related to the two dimensional NPS_{2D} as follows,

$$NPS_{NS}(u) = \int NPS_{2D}(u,v)\left|T(v)\right|^2 dv \qquad (3.38)$$

where *u*, *v* are the spatial frequency coordinates, and *T(v)* is the Fourier transform of the response function of the detector along the width *L* denoted as

[1] In chapter 5, the details of the use of EGSnrc to simulate some properties of this detector are described and hence the discussion is excluded here.

R(y). In a synthesized slit technique, this response function is a rectangular function of width *L*. However, in the present detector, the width of the crystals is 8 mm while the width of the photodiodes is 2 mm (figure 3.2). The photodiodes receive scattered optical photons from the crystal area beyond 2 mm width as well as some of the optical photons that fall on the non-sensitive part of the photodiode array and are reflected back into the crystals, a portion of which is again detected within the sensitive 2 mm width. Therefore, the response function of the detector in the width dimension is not rectangular and it is represented as such in equation 3.38. According to Williams *et al.* (1999), if the width L is large enough such that NPS_{2D} has a small change in the *v* direction over the narrow width of *T(v)*, then, as is expressed in equation 3.35, one obtains the following approximation between NPS_{NS} and NPS_{2D}.

$$NPS_{NS}(u) \approx NPS_{2D}(u,0)\int |T(v)|^2\, dv \tag{3.39}$$

Therefore, the *NPS* along the array dimension of the present detector is $NPS_{2D}(u,0)$ and can be evaluated from the natural slit *NPS* by dividing it by the integral in equation 3.39. The NPS_{NS} of sampled random data ΔS of length *N* from our detector is given by equation (3.36):

$$NPS_{NS}(u) = \frac{x_0}{N}\langle |DFT(\Delta S)|^2 \rangle \tag{3.40}$$

where *N* is the number of samples used in the discrete Fourier transform (*DFT*) and notation $\langle\ \rangle$ represents the expected value and,

$$NPS(u) \cong NPS_{2D}(u,0) \approx \frac{x_0}{N\int |T(v)|^2\, dv}\langle |DFT(\Delta S)|^2 \rangle \tag{3.41}$$

Since the integral in the denominator of equation 3.41 has units of mm^{-1}, the *NPS* resulting from this equation has units of ($volt^2\ mm^2$).

The detector was centered in a 2.5 x 32 cm^2 6 MV field and the data for 10,000 pulses were recorded at a SDD of 110 cm. We have used a narrow beam in the *NPS* measurements to protect the nearby electronic components from radiation damage. This irradiation geometry does not include any small change in the measured *NPS* caused by the increased head scatter in the broad clinical beams. The resulting data were divided by the mean signal of each detector element to remove the effects of beam profile and element-to-element sensitivity variations. For each radiation pulse, i, these normalized data, S_i, were divided into 5 sub-groups, each containing 16 detector elements. For each of the 5 sub-groups, k, the noise only data, $\Delta S_{i,k}$, for each radiation pulse were obtained by subtracting the first 8-elements from the second 8-elements. This step is necessary in order to avoid the large correlation among detector elements caused by the pulse-to-pulse fluctuations in the beam output. A *DFT* of the resulting 8-point ($N = 8$) noise-only data was performed to obtain one periodogram. Finally, the *NPS* was obtained by averaging these periodograms over the 5 sub-groups and total number of radiation producing pulses, I, as follows:

$$\Delta S_{i,k}(1:8) = S_i(16k-15:16k-8) - S_i(16k-7:16k) \qquad 1 \le k \le 5,\ 1 \le i \le I \tag{3.42}$$

$$NPS(u) = \frac{x_0}{(2 \cdot 5 \cdot I \cdot N \cdot \int |T(v)|^2 dv)} \sum_{i=1}^{I} \left(\sum_{k=1}^{5} \left| DFT(\Delta S_{i,k}) \right|^2 \right) \tag{3.43}$$

and

$$u = \frac{n}{8 \cdot x_0} (lp/mm);\ n = 0,1,2,3,4$$

Please note that the summations and division by (5I) approximate the expected value by an average value. The *NPS* was divided by 2 in equation 3.43 since $\Delta S_{i,k}$ is obtained by subtraction. The entire experiment was repeated 10 times to

assess the experimental errors. As a result of division by the mean signal, the aforementioned procedure calculates the normalized *NPS* in units of mm^2.

The detector response function *R*(y) was measured to evaluate the integral in equation 3.43 as follows. A slit beam of 0.4 mm width was formed by the same apparatus as used in the *MTF* measurements. The detector array was arranged such that the length of the slit beam was along the array dimension and the width along the width *L* of the crystals. The entire detector array was translated along the crystal width and past the slit width in steps of Δy (0.375 mm), and the detector data was measured for 5000 pulses at each step. The mean detector signal, *D*(nΔy), as a function of slit position relative to the centre of crystal width, normalized at centre, represents the response function.

$$R(n\Delta y)=\frac{1}{L}D(n\Delta y);\ for\ n=1,N_y\ and\ N_y=\frac{L}{\Delta y} \tag{3.44}$$

The integral in the denominator of equation 3.44 was then evaluated as follows.:

$$\int|T(v)|^2\,dv \approx \Delta v\sum_{i=0}^{N_y-1}\left|DFT\{R(n\Delta y)\}\right|^2;\ and\ \Delta v=\frac{1}{\Delta y N_y}mm^{-1} \tag{3.45}$$

iv. *DQE*

Equation 3.37 was used to find the *DQE* of the detector. The photon fluence impinging on the detector per radiation pulse, φ, was obtained by using the following method. The dose per unit fluence factor (F = 7.51 x 10^{-8} cGy mm^2/photon) was calculated in water by Lachaine *et al.* (2001) using the EGSnrc Monte Carlo software with the 6 MV spectrum of this machine. Rogers (1984) calculated the dose per unit fluence factors for a number of mono-energetic photons in ICRU four element tissue by using broad beam geometry simulations and the previous version of Monte Carlo simulation software (EGS3). Using the factors reported by Rogers (1984) at 1.5 cm depth in tables 9-12, and the relative

fluence spectrum of the 6 MV beam for our machine, we estimated the dose to fluence factor to be 7.94 x 10^{-8} cGy mm^2/photon. Since the mono-energetic factors were not calculated in water by Rogers in exactly the same geometry as the calibration condition of the linac, and the resulting poly-energetic factor is only 5.7% different from that calculated by Lachaine *et al.* (2001), we used a value of 7.51 x 10^{-8} cGy mm^2/photon in our calculations. Therefore,

$$\varphi = \frac{\dot{D}}{F} \tag{3.46}$$

The dose per radiation pulse $\dot{D}$ was calculated as follows. The treatment beam was calibrated to deliver 1 cGy per MU at 1.5 cm depth in water for a 10 x 10 cm^2 field at 100 cm from the source. Using this geometry a pinpoint chamber (N31006, PTW Freiburg) was placed at 1.5 cm depth in a solid water phantom. The chamber reading (r_0) was recorded as 100 MUs were delivered. A second reading (r) was obtained using a 2.5 cm x 32 cm field size at a distance of 110 cm from the source to replicate the irradiation condition of the *NPS* measurement. Therefore the dose delivered at 1.5 cm depth in the geometry of *NPS* measurements was obtained as (100 r/r_0) cGy. The number of pulses, N, that actually produced radiation was determined from the data acquired with the detector array. Therefore, $\dot{D}$ is given as (100 $r/(r_0N)$).

In order to further establish that the fluence calculation is reasonable, we calculated the zero-frequency *DQE* of the detector using the method suggested by Swank (1973) and used by Keller *et al.* (2002) for a 1-D Xenon gas based arc detector array. The absorbed energy distribution, $AED(E=n\Delta E)$, is the probability that an incident photon from the 6 MV spectrum deposits *E* amount of energy in the detector array. Monte Carlo simulation, similar to that used in the radiation *MTF* calculation, was also used to score the $AED(E=n\Delta E)$ in the entire crystal, i.e. by ignoring voxels, in 0.01 MeV (ΔE) energy bins. The zero-frequency *DQE*(0) was calculated as M_1^2 / M_2 where M_1 and M_2 are, respectively, the first and second order energy moments of the *AED* defined as follows:

$$M_j = \sum_n (n\Delta E)^j \, AED(n\Delta E); \; j = 1,2. \tag{3.47}$$

where n denotes the energy bin number and the summation is taken over 600 energy bins.

v. Radiation Damage

Radiation hardness of $CdWO_4$ crystals has been studied previously (Kobayashi et al., 1994, Kozma et al., 2000) in a Co^{60} beam for doses of 10^5Gy and 10^8Gy. Since $CdWO_4$ scintillation crystals have been used extensively in single slice diagnostic CT systems, the radiation damage to the crystal-photodiode pair is not a significant issue if utilized for MVCT alone. However, the final goal of this project is to create a 2D detector array that can be utilized both for imaging and exit fluence measurements during radiotherapy treatments. In this situation, the detector array may receive up to 30 Gy per day based on 50% transmission through thirty patients each receiving a dose fraction of 2 Gy. Thus, we measured the effect of approximately 25 Gy per day on the detector array.

To avoid damaging the electronic components with the leakage radiation from the linear accelerator, the experiment was carried out in a Co^{60} beam using narrow beam collimation. The detector array was placed 84.5 cm from the source in a cobalt teletherapy unit (780E, Theratronics, Kanata, Canada). The collimator of the Co^{60} unit was set at 4.2 x 7.8 cm^2 and the irradiation field was further collimated to about 0.8 x 8.0 cm^2 by two lead blocks. The beam was turned on for 1.2 minutes and an average of 5000 readings for each detector element was collected at the end of the radiation period; the total time of data acquisition was 0.25 s. The detector was given a 5 minute recovery period to simulate the minimum time between two consecutive patient treatments. The 1.2 minute irradiation and subsequent 5000 point data collection was repeated. The cycle of irradiation and recovery period was repeated 20 times. Using the calibration data and the output factor for a 4.2 x 7.8 cm^2 field, each irradiation of 1.2 minutes is estimated to deliver a dose of 1.36 Gy to a small mass of tissue in free-space. This value is multiplied by the tissue air ratio, estimated as 1.0075 for Co^{60}, of the

collimated field at 0.5 cm depth, and ratio of the mass absorption coefficient of $CdWO_4$ to tissue (0.895) to give 1.23 Gy to $CdWO_4$ for each 1.2 minute irradiation and amounting to a total dose of 24.5 Gy. The mass absorption coefficients of tissue and $CdWO_4$ are available from NIST (2006). The experiment was repeated on four different days. The mean and standard deviation of the mean detector signal over four days were calculated and analyzed as a function of accumulated radiation dose. $CdWO_4$ is not expected to significantly recover its lost sensitivity during the irradiation period because of the long (10-20 hours) recovery period (Kobayashi et al., 1994), thus, the measured radiation damage is not expected to have a dose rate effect. Therefore, the radiation damage in a 6 MV pulsed beam should be similar to that in a Co^{60} beam for a given accumulated dose to $CdWO_4$.

D. Results

i. Linearity

a. Detector Response to Dose Rate

The linear regression analysis performed on the detector signal as a function of $(100/SDD)^2$ indicated a very linear response of the detector with dose rate. The R^2 coefficient was better than 0.9998 for all elements in the detector array. Since the standard deviation for each data point is less than 0.25%, the data points follow a straight line very well. However, there was a considerable (> two times) variation in the slopes indicating a large element-to-element variation in the sensitivity.

b. Attenuation Measurement

The attenuation of 6 MV photons by solid water is plotted in figure 3.11 for detector elements 1 and 40. Detector element 40 was positioned close to the central axis of the beam and detector element 1 was located 12.4 cm off axis. Therefore, detector element 1 saw a slightly larger solid water thickness due to the diverging path. The deviation of the second order fit from the straight line fit to the first four points for element 1 at larger solid water thickness indicates the

presence of spectral hardening. At a solid water thickness of 20 cm, the measured attenuation is about 5.5% lower than predicted by the extrapolated straight line. The second-order polynomial described the measured attenuation data (standard deviation of < 1%) very well for all the detector elements (R^2 = 1.0). For detector element 1, the second-order component amounts to 7.5% of the total attenuation at a thickness of 20 cm. For detector element 40, the measured attenuation of the beam is less than that for detector element 1. This is due to a conical-shaped flattening filter in the linac beam causing the photon beam to be more penetrating on the central axis. Attenuation measurements are discussed further in the "beam hardening" section in the following chapter.

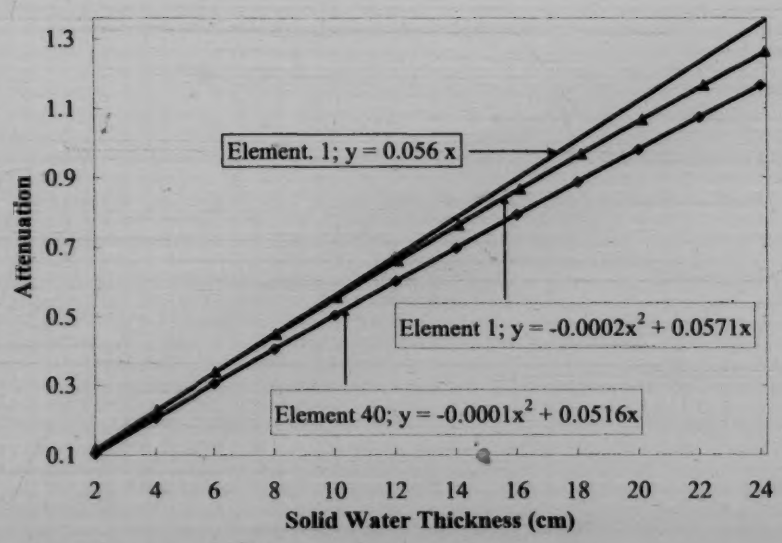

Figure 3.11: Plot of the attenuation of 6 MV photons by solid water as measured by detector elements 1 and 40. The straight line fit to the first four points of the detector element 1 data is extrapolated to increased thickness to indicate the amount of spectral hardening. Second order polynomials fit to all data describe the spectral hardening very well. The attenuation data for the remaining elements lies in between elements 1 and 40. The error bars on the measured data points are smaller than the symbols.

ii. MTF_{pre}

The measured and calculated *MTFs* are plotted in figure 3.12. Since the measured pre-sampling spanned the length of the array (80 x 3.15 = 252 mm), the resolution of the measured pre-sampling *MTF* in frequency space is 0.003968 mm^{-1} i.e. 1/(252 mm) giving measured points close to zero-frequency. For reference, the Nyquist frequency of the detector array is only 0.16 lp/mm due to the large pitch. The radiation *MTF* was obtained by dividing the pre-sampling *MTF* by the aperture *MTF*; it was not calculated in the vicinity of zero-crossings of the aperture *MTF* to avoid magnification of errors. Aliasing in the measurement of the pre-sampling *MTF* is negligible up to the Nyquist frequency of the detector array because the pre-sampling *MTF* is small at 0.8 lp/mm. This is also suggested by the *MTF* from the Monte Carlo simulation (also shown in Fig. 3.12) which is higher than the radiation *MTF* at all spatial frequencies (see Discussion section). The Monte Carlo calculated radiation *MTF* can be compared with the measured radiation *MTF* in the low spatial frequency range. The Monte Carlo calculated *MTF* is determined by the charged particle transport and, to a lesser extent, by Compton scattering.

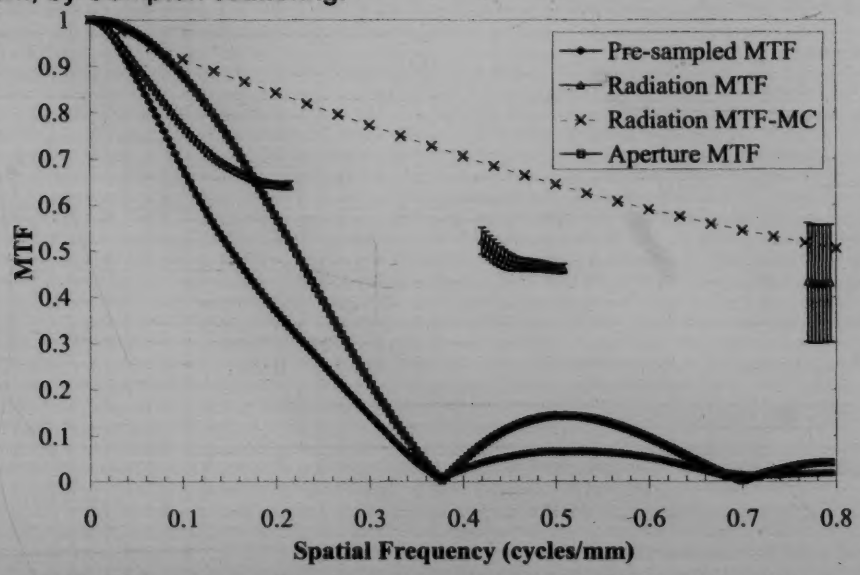

Figure 3.12: The pre-sampling, aperture and radiation *MTFs* of the detector array. For reference, the Nyquist frequency of the detector array is 0.16 lp/mm. The radiation *MTF* is obtained by dividing the pre-sampling *MTF* by the aperture *MTF*. The error bars on the crystal *MTF* are larger due to the division. Radiation *MTF* –MC is calculated using Monte Carlo simulation.

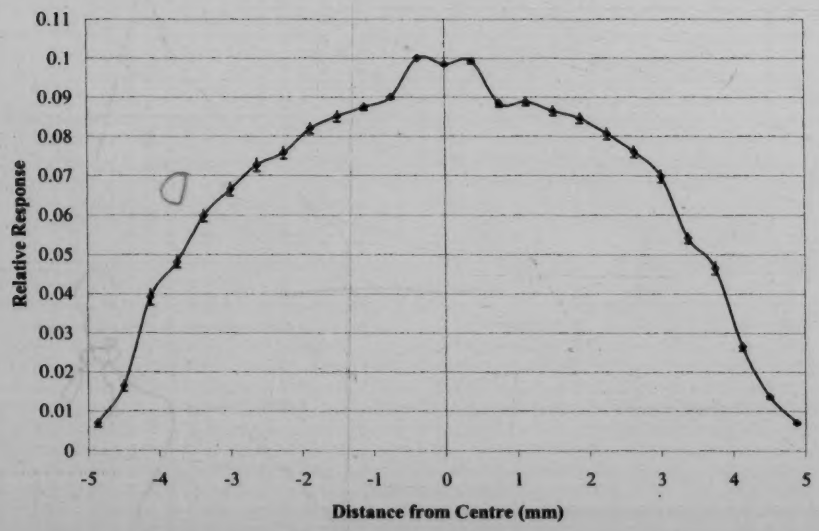

Figure 3.13: The measured relative detector response *R(nΔy)* as a function of distance of an 0.4 mm slit from the center of thr crystals in the direction perpendicular to the array. The error bars indicate ±1 standard deviation calculated from the central 8 elements.

iii. *NPS*

The measured relative response of the detector, *R(nΔy)*, perpendicular to the array direction is shown in figure 3.13 as a function of the distance from the centre of the crystals. This function is used to calculate the integral in equation 3.45 as part of *NPS* normalization in equation 3.43. Although the crystal width is 8 mm, the detectors provide signals even when the slit is located beyond 4 mm from the center because of the additional reflective coating at these surfaces. Charged particles created in the coating materials travel to the crystals and create signal. The sensitive detector width, *L*, in equation 3.45 was determined to be 10 mm as the extent of the non-zero signal in figure 3.13. The measured *NPS* of the detector array up to the Nyquist frequency in the 6 MV beam is plotted in figure 3.14.

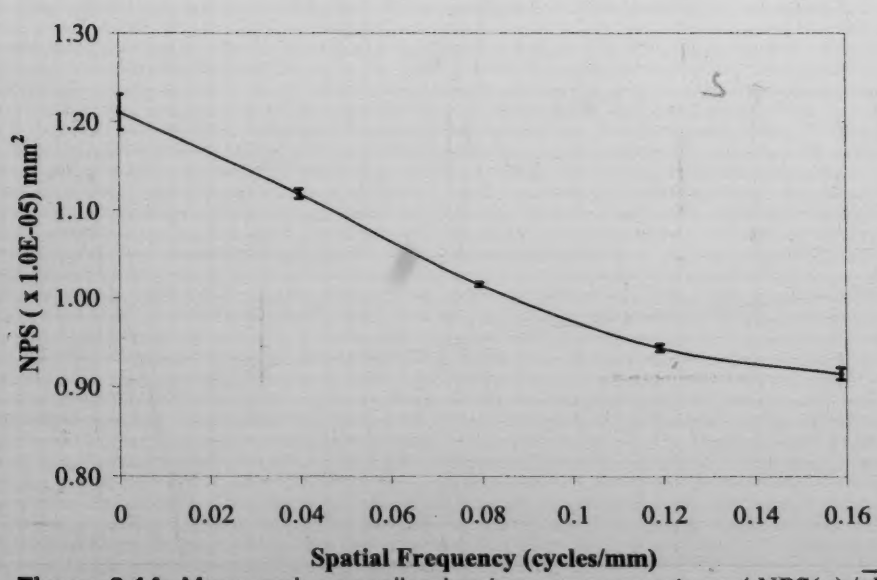

Figure 3.14: Measured, normalized noise power spectrum ($NPS(u)/\overline{d}^2$) for the *CdWO₄* array in a 6 MV beam.

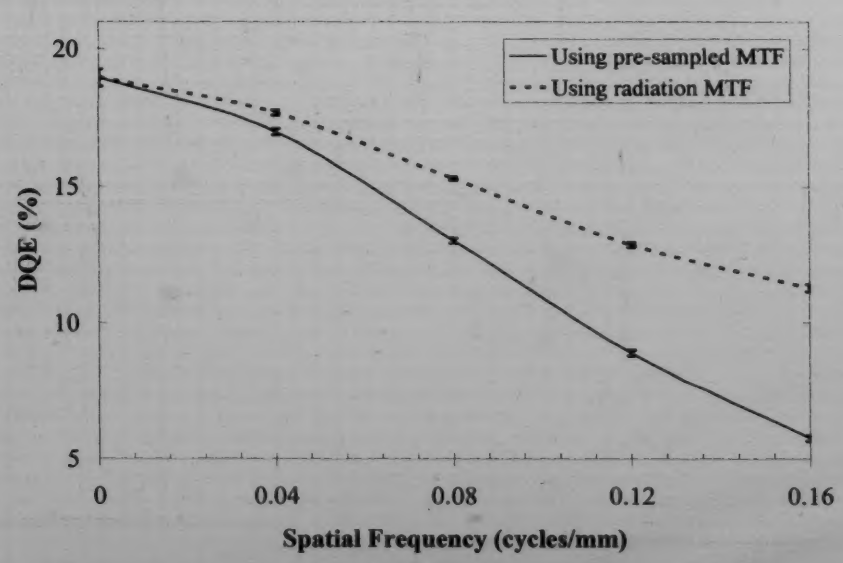

Figure 3.15: The measured detective quantum efficiency of the *CdWO₄* array calculated using the pre-sampling and radiation *MTFs* in a 6 MV beam.

iv. *DQE*

The measured pre-sampling and radiation *MTFs* were used to calculate the *DQE* of the detector array, and the results are plotted in figure 3.15. The *DQE* at zero spatial frequency is about 18.8 % and decreases at higher spatial frequencies. The higher *DQE* using the radiation *MTF* shows that the large detector pitch of 3.15 mm adversely affects the *DQE* at higher spatial frequencies. In a future implementation of this detector (see chapter 5), a smaller element pitch will be considered to reduce aliasing effects on the *MTF* and *DQE*. The value of 18.8 % for the measured *DQE* is in good agreement with the 19% calculated previously (Monajemi *et al.*, 2004; Monajemi, 2004) using a two-step Monte Carlo simulation. The first and second order energy moments of the AED determined by the Monte Carlo simulation in the present work were calculated to be 0.35 and 0.65 respectively that also resulted in zero-frequency *DQE* of 19% using Swank's method. This calculation indirectly verifies that the fluence per pulse estimate and the *NPS* normalization are reasonable.

v. Radiation Damage

Plotted in figure 3.16 is the mean detector signal as a function of the accumulated dose to scintillation crystals. Although only three detector elements are shown, the data for the other detector elements showed similar trends. The error bars show ± 1 standard deviation (< 0.5%) of the mean detector signals over four experiments. The data clearly show that the mean detector signal decreases continuously as a function of accumulated dose; however, the reduction in signal is less than 2% for all detector elements. The data also indicate that a significant portion of the small reduction in mean signal is recovered by the next day. However, because the experimental set up needed to be dismantled at the end of each day the measurements varied randomly due to the uncertainty in positioning the detector in the beam. As a result of this uncertainty, we did not observe a consistent increase or decrease in the detector

data from day-to-day. Figure 3.16 also includes the minimum and maximum values for detector element 42. The curve corresponding to the minimum values was observed on the first day of irradiation while the curve corresponding to the maximum values was observed on the third day of irradiation. Since the temperature coefficient (Saint-Globain) of the optical yield in $CdWO_4$ is less than 0.1%/°C (at 25°C), small day-to-day variation in the room temperature (< 1 °C) is not likely to create inconsistency in the measured data.

It should also be noted that these data cannot be easily compared with previous studies (Kobayashi et al., 1994, Kozma et al., 2000) because they looked at the reduction in luminescence at the wavelength of peak emission due to very large (10^3 – 10^6 Gy) dose in much larger $CdWO_4$ crystals.

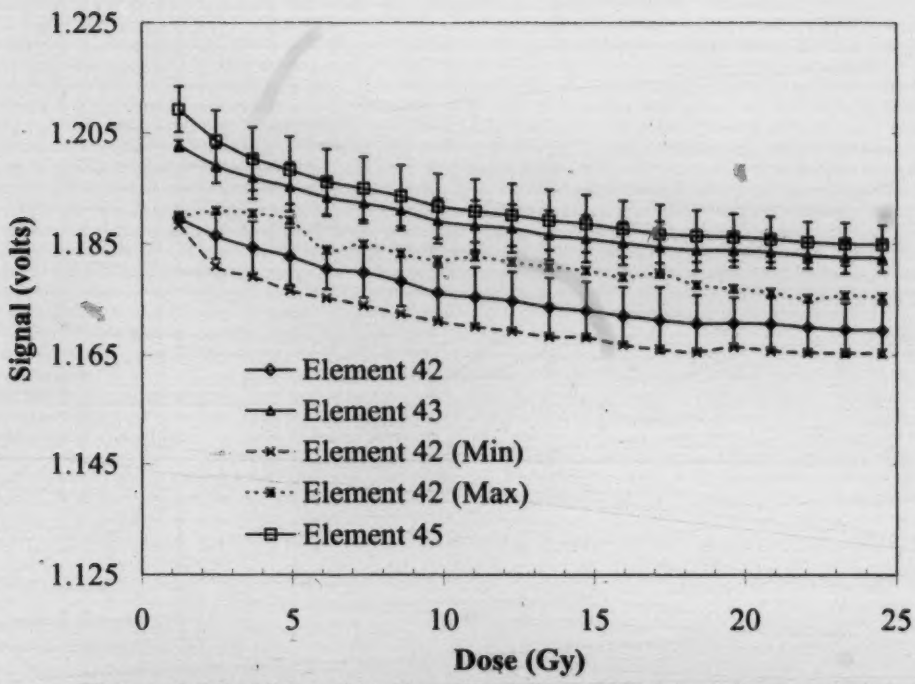

Figure 3.16: Mean detector signal (per unit integration period = 0.7 msec) as a function of accumulated dose to $CdWO_4$ crystals. The error bars indicate ± one standard deviation (< 0.5%) of measurements conducted on four different days and reflect set up uncertainty.

E. Discussion

The data in the attenuation measurements suggests that a correction for spectral hardening is required for the fan-beam data acquired by the prototype MVCT system. It also suggests that such corrections vary from element to element due to the presence of the conical flattening filter. It should be noted that the element-to-element correction (usually referred to as the flood field correction) removes the effects of element-to-element sensitivity variation and the variation in primary fluence across the detector. Since it is based on open-beam measurement, it does not account for the variation in the attenuation by imaged objects due to the variation in the primary beam spectrum across the detector. The use of the attenuation data to correct for image artifacts is described in the next chapter.

The difference between the measured radiation *MTF* and the Monte Carlo calculated *MTF* could potentially be caused by the leakage and scattered radiation produced within the 25 cm long lead blocks. However, the same blocks were also used in measuring the *MTF* of a similar detector in our previous study (Monajemi *et al.*, 2004; Monajemi, 2004) where a two step Monte Carlo approach was also used to include the effect of optical photon transport. A very good agreement between the measured *MTF* and that obtained from two step Monte Carlo approach was obtained. Since two-step Monte Carlo approach did not account for the leakage and scattered radiation within the lead blocks, this agreement indirectly suggested that leakage and scattered radiation in lead blocks is negligible. The measured radiation *MTF* has extra spreading of signal due to the leakage of optical photons through the optical glue and a small degree of optical photon leakage through the reflective gelcoat. Most of the leakage occurs through the common optical glue sheet placed between the bottom surface of the crystal arrays and the top surface of the photodiode arrays. Therefore, the measured radiation *MTF* is significantly lower than the Monte Carlo calculated radiation *MTF*. Since the radiation *MTF* is obtained by de-convolution, it has large errors at frequencies larger than 0.24 lp/mm. Even within the lower frequency range, the aperture *MTF* dominates the shape of the pre-

sampling *MTF*. Since the pre-sampling *MTF* is dominated by the aperture *MTF* at low frequencies, decreasing detector pitch should improve the pre-sampling *MTF*. However, the spatial resolution in the projection data is also determined by the focal spot size (Munro et al., 1988) of the linear accelerator and geometric magnification (Siewerdsen and Jaffray, 2000; Moy, 2000). Therefore, an optimal detector pitch should be determined by taking all these factors, including the radiation and optical transport in scintillators, into account which is part of a further investigation described in chapter 5. Since the detector array is similar in configuration to the Xenon gas arc detector described by Keller *et al.* (2002), the measured radiation *MTF* can be compared with the *MTF* presented in figure 12 of their publication for a tungsten plate thickness of 0.32 mm corresponding to the arc detector used in their bench top MVCT. The two *MTF*s are comparable up to 0.2 lp/mm and $CdWO_4$ *MTF* (0.46) is larger than Xenon gas detector *MTF* (0.3) around 0.5 lp/mm. Additionally, the frequencies at 0.5 *MTF* (f_{50}) are around 0.43 and 0.32 lp/mm respectively for $CdWO_4$ and Xenon gas detector, although the large error bars on $CdWO_4$ *MTF* should be kept in mind in making the comparison.

The relative decrease in the measured *NPS* as a function of spatial frequency is generally compared with the squared magnitude of the pre-sampling *MTF* to understand the noise correlation caused by the x-ray absorption noise. For the case of the present detector with a large pitch, such a comparison would indicate that the *NPS* does not decrease as rapidly with frequency as the squared pre-sampling *MTF* due to aliasing in the measured *NPS*. This over estimation of the measured *NPS*, caused by aliasing at non-zero spatial frequencies will tend to underestimate the measured *DQE* at non-zero frequencies.

An imaging arc detector using tungsten plates immersed in pressurized Xenon gas has been studied by Keller *et al.* (2002). A Monte Carlo simulation performed on a 1-D array by Keller *et al.* (2002) calculated *DQEs* of 20.4% and 31.4% in a 4 MV beam respectively for the focused and non-focused arrangements corresponding to 0.32 mm tungsten plate thickness. However, the

non-focused detector may suffer from poor spatial resolution. The zero frequency *DQE* of our $CdWO_4$ array is about 19% in a 6 MV beam and it is expected to be larger in a 4 MV beam. The advantage of a $CdWO_4$ array is that the *DQE* can be further increased by using slightly thicker crystals if the optical isolation between detector elements is maintained. Moreover, back-illuminated photodiode arrays (Semicoa, Costa Mesa, California) can be tiled in 2D because the wire bonding and optical windows of the photodiodes are on the opposite sides of the substrate. These arrays will allow a focused, high *DQE*, 2D detector to be built. The loss of resolution due to divergent rays in unfocussed detectors was studied by Moy (2000) and alternative schemes, using flat panel photodiode arrays, of focusing thick scintillation crystals toward the radiation source were suggested by Pang and Rowlands (2002, 2004) and Sawant *et al.* (2005). The use of 2D tiled photodiode arrays to build focused MVCT detectors is discussed in chapter 5.

The radiation damage experiments show that the $CdWO_4$-photodidode detector will show a reduction in signal of < 2.0% if the detector is used to measure the exit fluence for every patient on a particular day. Also, a significant portion of the lost sensitivity will be recovered by the next day within the experimental uncertainty of < 0.5%. However, any permanent loss (or gain) in the detector sensitivity of less than 0.5% can neither be established nor ruled out using these data because we did not observe a consistent increase or decrease in detector response from day-to-day due to setup uncertainty. A better controlled experiment will be required to measure any permanent damage to this detector due to large doses of radiation. The loss of sensitivity caused by radiation damage is unlikely to produce ghosting artefacts. Ghosting artifacts have been described by Siewerdsen *et al.* (1999) for an indirect detection active matrix flat panel detector due to signal lag, and in direct detection active matrix flat panel detectors due probably to space charge effects by several others (Zhao et al., 2002, Schroeder et al., 2004). Ghosting occurs when sensitivity reduction and recovery processes have a time constant of the order of the reading cycle of the detector. In the imaging experiments, the dose delivered to the $CdWO_4$ array is expected to be less than 10 cGy. Since the reduction in signal for approximately

25 Gy accumulated to the detector is less than 2%, the effect of 10 cGy would be negligibly small to create any ghosting effect. It can be argued that the detector can suffer a slight sensitivity loss if it is left in the beam during patient treatment and, thus, may receive larger doses. However, since there is negligible radiation damage during the imaging experiment and the recovery time constant for lost sensitivity is of the order of several hours (Kobayashi *et al.*, 1994), the radiation damage phenomenon is unlikely to cause any ghosting effect. The signal lag is also not expected to be a problem with this detector due to very small afterglow in $CdWO_4$ crystals (Monajemi *et al.*, 2004; Monajemi, 2004). Also, synchronization of data collection with the linac pulse interval of 7.3 msec will not create signal lag because of a small afterglow. The radiation damage due to small dose per pulse (<0.05 cGy) is not expected to create ghosting in pulse-to-pulse data collection. Any small CT number drift that may be caused by the loss in sensitivity of these scintillators during on day, can be addressed by performing frequent (4-5) air scans in one treatment day,

F. Conclusions

We have fabricated a prototype detector array of $CdWO_4$-photodidodes to be used in a bench-top fan-beam MVCT scanner. The detector electronics, data multiplexer, data acquisition timing control, rotary stage control and the data acquisition system for this prototype have been designed and shown to work well. The detector responds linearly to dose rate. A small yet significant amount of spectral hardening effect was determined in the attenuation measurements of 6 MV photon beam by solid water. This will form the basis of a spectral hardening correction used in the processing of the fan-beam projection data in the next chapter.

The pre-sampling *MTF* of this detector is dominated by the large pitch of 3.15 mm and the radiation *MTF* shows that a reduction in detector pitch may have a sizeable improvement on the spatial resolution. The most important feature of this detector is the large *DQE(0)* of 18.8%. In its own class of detectors, i.e. scintillation-photodiodes, the detector offers the largest *DQE* per

unit crystal thickness which suggests a significant reduction in radiation dose in MVCT imaging experiments. This issue is even more important since the $CdWO_4$-photodidode array can be extended into 2-D, aided by the recent advent of 2-D back-illuminated photodiode arrays and advances in array fabrication.

Radiation damage to the $CdWO_4$-photodiode combination is a significant issue; however, no previous data exists for the irradiation response of this combination. The experiments conducted in this work indicate that a reduction in detector sensitivity of less than 2% can be expected over a one day period and the detector recovers a large fraction of its lost sensitivity overnight. Any permanent damage to the detector array cannot be established.

In summary, a $CdWO_4$-photodidode detector array offers a large *DQE*. In subsequent work, we will investigate the imaging performance of this detector in MVCT application.

G. References

A. Berndt, S. Rathee, D. W. Rickey and J. Bews, "An 8-channel Detector for an ^{192}Ir brachytherapy source-based computed tomography scanner", IEEE Trans. Nucl. Sc. **47**, 1261-1267 (2000).

I. A. Cunningham, "Applied Linear Systems Theory", *in Handbook of Medical Imaging,* edited by R. L. Van Metter (SPIE, Bellingham, WA, 2000) Ch. 2.

J. C. Dainty, and R. Shaw, *Image Science,* Academic Press, 1974.

H. Fujita, D. Y. Tsai, T. Itoh, *et al.*, "A simple method for determining the modulation transfer function in digital radiography," IEEE Trans. on Medical Imaging **11**, 34-39 (1992).

I. Kawrakow and D.W.O. Rogers, "The EGSnrc code system: Monte Carlo simulation of electron and photon transport," NRCC Report PIRS-701 (2002).

H. Keller *et al.*, "Monte Carlo study of a highly efficient gas ionization detector for megavoltage imaging and image-guided radiotherapy", Med. Phys., **29**(2), 165-175 (2002).

M. Kobayashi, M. Ishii, Y. Usuki and H. Yahagi, "Cadmium tungstate scintillators with excellent radiation hardness and low background", Nucl Instrum Meth A **349**(2-3), 407-411, (1994).

P. Kozma, R. Bajgar, and P. Kozma Jr., "Radiation resistivity of large tungstate crystals", Rad. Phys. Chem., 59, 377-380, (2000).

M. Lachaine, E. Fourkal and B.G. Fallone, "Detective quantum efficiency of a direct-detection active matrix flat panel imager at megavoltage energies," Med. Phys. **28** , 1364-1372 (2001).

T.T. Monajemi, S. Steciw, B. G. Fallone and S. Rathee, "Modelling scintillator-photodiodes as detectors for megavoltage CT," Med. Phys. **31** (5), 1225-1234, (2004).

T.T. Monajemi, *Modelling scintillator-photodiodes as detectors for megavoltage CT*, MSc thesis, 2004.

J. Moy, "Signal-to-noise ratio and spatial resolution in x-ray electronic imagers: is the MTF a relevant parameter?" Med. Phys. **27**, 86-93 (2000).

P. Munro, J. A. Rawlinson and A. Fenster, "Therapy imaging: source sizes of radiotherapy beams", Med. Phys. **15** (4), 517-524 (1988).

G. Pang and J. A. Rowlands, "Development of high quantum efficiency flat panel detectors for portal imaging: Intrinsic spatial resolution", Med. Phys., **29**(10), 2274-2285, (2002).

G. Pang and J. A. Rowlands, "Development of high quantum efficiency, flat panel, thick detectors for megavoltage x-ray imaging: A novel direct-conversion design and its feasibility", Med. Phys., **31**(11), 3004-3016, (2004).

D. W. O. Rogers, "Fluence to dose equivalent conversion factors calculated with EGS3 for electrons from 100 keV to 20 GeV and photons from 11 keV and 20 GeV," Health Phys. **46**, 891-914 (1984).

A. Sawant, L. E. Antonuk, Y. El-Mohri, *et al.*, "Segmented crystalline scintillators: An initial investigation of high quantum efficiency detectors for megavoltage x-ray imaging", Med. Phys., **32**(10), 3067-3083, (2005).

C. Schroeder, T. Stanescu, S. Rathee, B. G. Fallone, "Lag measurement in a-Se active matrix flat panel imager," Med. Phys. **31**, 1203-1209 (2004).

J. H. Siewerdsen and D. A. Jaffray, "Optimization of x-ray imaging geometry (with specific application to flat-panel cone-beam computed tomography)," Med. Phys. **27**, 1093-1914 (2000).

J. H. Siewerdsen and D. A. Jaffray, "A ghost story: spatio-temporal response characteristics of an indirect-detection flat panel imager," Med. Phys. **26**, 1624-

1641(1999).

J. H. Siewerdsen and D. A. Jaffray, "Cone-beam computed tomography with a flat panel imager: Effect of image lag," Med. Phys. **26**, 2635-2647 (1999).

R. K. Swank, "Absorption and noise in x-ray phosphors", J. Appl. Phys., **44**, 4199-4203, (1973).

D. Tu, *Bench-top Megavoltage Computed Tomography Scanner with Cadmium Tungstate-Photodiode Detectors*, MSc. Thesis, University of Alberta (2005).

Van den Heuvel, T. Powell, E. Seppi, *et al.*, "Independent verification of ultrasound based image-guided radiation treatment, using electronic portal imaging and implanted gold markers," Med. Phys. **30**, 2878-2887 (2003).

M. B. Williams, P. A. Mangiafico, and P. U. Simoni, "Noise power spectra of images from digital mammography detectors", Med. Phys., **26**(7), 1279-1293, (1999).

www.detectors.saint-gobain.com

www.nist .gov/ PhysRefData; "NIST: The National Institute of Standards and Technology website"

W. Zhao, C. DeCrescenzo, and J. A. Rowlands, "Investigation of lag and ghosting in amorphous selenium flat-panel x-ray detector", Proc. SPIE, 4682, 9-20, (2002).

Chapter 4

The Bench-top System: B. Image Performance Evaluation

A detailed description of our prototype fan-beam MVCT system along with the characterization of signal acquired from the 80-element detector array is presented in the previous chapter. In this chapter, we present the performance characteristics (i.e. image quality) of this prototype CT scanner mainly in a Co^{60} (780E, MDS Nordion, Kanata, Canada) beam. During the earlier phases of the project, some images were also taken in a 6 MV (600C, Varian Medical Systems, Palo Alto, CA) beam. As mentioned in the previous chapter the system has run reliably except for an initial problem with the detector boards. It was noticed very early in the experimental stage that the analog switches on the detector boards are sensitive to leakage radiation through the accelerator jaws. Therefore, the 6 MV imaging experiments were abandoned. We manufactured extra shielding blocks to protect the detector board electronics. It should also be noted that the detector boards have a practical limitation in that the change in detector gain required between the 6 MV and Co^{60} experiments was obtained by physically replacing the resistors in the feed back loop of the amplifiers (see figure 3.4). Therefore, experiments could not easily be repeated on both 6 MV and Co^{60} units. While most of the experiments in the previous chapter were performed in a 6 MV photon beam, as the project progressed we found it easier to work with the lower dose rate in Co^{60}. Therefore, we were not able to produce low dose images at 6 MV and hence the imaging performance was not evaluated for this beam. Similar to other investigators (Simpson *et al.*, 1982, Lewis *et al.*, 1992, Seppi *et al.*, 2003), we found the presence of ring artefacts to be the most persistent problem in our system; a calibration method was developed to minimize the

presence of these artefacts. The low contrast resolution (LCR) in the reconstructed CT images is studied as a function of radiation dose and target size. The experimental signal to noise ratio (SNR) performance of the system as a function of radiation dose is also presented. In our final results, we discuss the spatial resolution and the dependence of CT numbers on material density in our system.

A. Methods and Materials

i. Imaging Geometry

A typical geometry for a third generation CT scanner is illustrated in figure 4.1. Typically a large number of detectors are focused on the x-ray source. The size of the detector array must be sufficiently large so that the object is within the field of view of the detector at all times. The x-ray source and the detector remain stationary with respect to each other while the entire system rotates about the patient (Hsieh, 2003). In the bench-top variation of the scanner for research purposes, the source and detector remain stationary while the object is rotated.

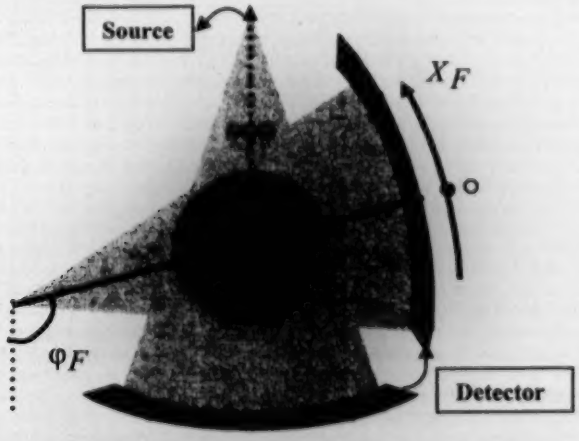

Figure 4.1: Third generation CT scanner geometry. *SOD* is the distance from the source to the centre of rotation; X_F is curvilinear distance from centre for elements along the detector arc; φ_F is the fan beam projection angle given by the rotation of the source from the vertical position.

The imaging experiments were mainly performed in a Co^{60} beam while the beam hardening calibrations were studied both in Co^{60} and 6 MV beams. A photograph of the imaging geometry is shown in figure 4.2 for the Co^{60} imaging experiments. The Co^{60} gantry and the image receptor are stationary; the gantry is positioned at 90°, i.e. horizontal position. A precision rotary stage (200RT, Daedal Division, Parker Hannifin Corp, Irwin, PA) was used to rotate all the phantoms. The precision stage is rotated by a stepper motor (ZETA57-83, Compumotor Division, Parker Hannifin Corp, Rohnet Park, CA) that is controlled via the digital ports and a programmable pulse generator from the data acquisition board (PCI-MIO-16XE, Austin, TX). The rotary stage completes one revolution in 22.5 seconds. The image receptor sits on a manually translated linear stage (linear resolution = 0.375 mm) that is used to align the center of the detector array with the central axis of the beam, and the center of rotation of the precision stage. A small Plexiglas cylinder containing a 1 mm thick lead wire at the center was precisely machined to fit in the central hole of the rotary platform and used for aligning the center of rotation of the stage with the center of the detector array. The centre of the detector arc is located at a distance of 110 cm from the photon source in all the experiments. The orientation of the detector with respect to the central beam axis is similar to figure 4.1. The centres of all the CATPHAN500 phantom modules were placed at a distance of 70 cm from the Co^{60} source. This distance was chosen to minimize the scatter from the phantom on the image receptor while utilizing most of the field of view of the detector. The centres of the in-house electron density phantom was placed at a distance of 95 cm from the source to fit the phantom within the field of view of the image receptor. Slice numbers 6 and 7 of the Alderson Rando phantom were placed at a distance of 80 cm from the Co^{60} source for imaging. The precision rotary stage is equipped with a magnetic home switch indicating the zero position. The imaging data collection gate is enabled between two consecutive zero-position signals. The frequency of the data collection cycle is set to 694 and 137 Hz (linac pulse

frequency), resulting in 15617 and 3083 data points for each detector per 360° rotation, respectively for Co^{60} and 6 MV beams.

Figure 4.2: The experimental set up for imaging in a Co^{60} beam. The phantoms were rotated while the γ–ray source and the detector array were held stationary.

ii. Phantoms

Spatial resolution, image SNR and uniformity, and LCR were studied using CATPHAN500 (The Phantom Laboratory, Salem, NY). Individual modules, each with a diameter of 15 cm and different thicknesses were removed from the phantom to fit into the approximately 16 cm diameter field of view of the standard imaging geometry of the prototype CT scanner (Source to detector distance (SDD) = 110 cm; source to object distance (SOD) = 70 cm). The 4 cm thick spatial resolution module (CTP528-figure 4.16) contains 2 mm thick aluminium contrast bar patterns that are placed at a radial position and provide a measure of spatial resolution ranging from 1 to 21 line pairs per cm. The image of the bar pattern phantom was evaluated visually to see which bar pattern was visible in the image. To study the SNR of the system, as well as to assess the uniformity of the images, the CTP486 module (near water equivalent uniform phantom of 6.8 cm thickness) of CATPHAN500 was used. A specially designed module (CTP612-figure 4.13, 3.8 cm thick) was used to assess the low contrast resolution of the system. This phantom consists of inserts at 3%, 2.5% and 1.5% nominal contrast levels. These contrast levels are measured as the difference between the density of each plug and the background material divided by the

density of the background material. Each contrast level has cylinders of diameters 2, 0.4, 0.5, 0.6, 0.7, 0.8 and 1.5 cm, and there is a central cylinder of 1.5 cm diameter with a contrast level of 1.5%. To assess the relationship between pixel value and density for this system, an in house phantom with a diameter of 19.1 cm and thickness of 5 cm (figure 4.17) was used in a slightly different imaging geometry (SDD = 110 cm, SOD = 95 cm). This phantom has different plugs with varying densities. These plugs are labelled *a*, *b*, *c*, *d*, *e*, *f*, *g*, *h*, *i*, *j*, *k* and *l* in figure 4.17 and have corresponding densities of 1, 2.228, 0.65, 2.18, 1.276, 1.39, 0.789, 1.263, 0.92, 1.87, 1 and *unknown* g/cm^3 respectively. The background material is made of Plexiglas with a density of 1.16 g/cm^3. We also used two slices from the Alderson Rando phantom (figure 4.18) to demonstrate the image quality in a humanoid phantom (SDD = 110 cm, SOD = 80 cm). Alderson Rando is a 175 cm tall, 73 kg anthropomorphic phantom designed to facilitate dosimetric measurements in geometry faithful to the human anatomy. The phantom is transected horizontally to give 2.5 cm thick slices through a model of the human body.

III. Basic Data Processing

As mentioned above we collect 15617 and 3083 data points for each detector per 360° rotation in Co^{60} and 6 MV beams, respectively. These data points were arranged in a matrix so that each row represents one set of these 15617 or 3083 data points (views), and each column represents the reading of one detector. This matrix – the sinogram – for an airscan (i.e. no phantom is placed in the beam) in Co^{60} and 6 MV beams is shown in figure 4.3. The black horizontal lines across some rows in figure 4.3 (a) show the effect of linear accelerator sync pulses when the radiation is off, on the reading of the detector. The first step in analyzing the data from a linear accelerator for our system, therefore, is to eliminate these rows in the sinogram while making sure that the angle of each view (i.e. row) is still recorded properly.

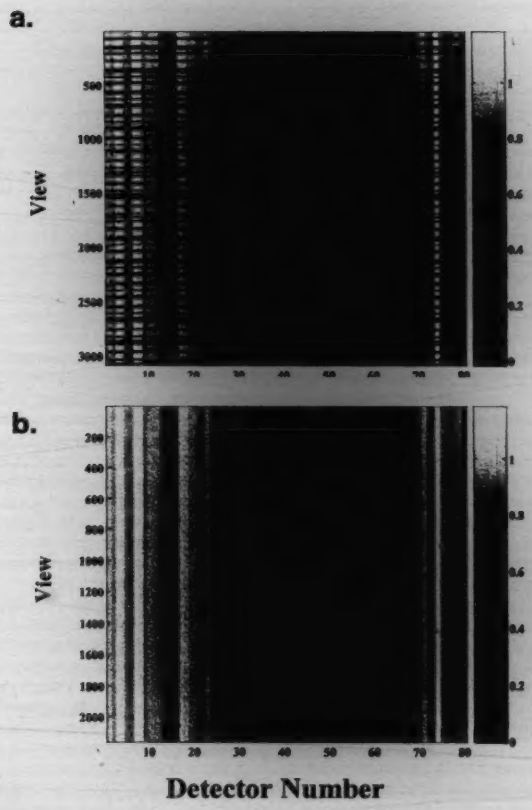

Figure 4.3: The raw air scan data acquired in (a) 6 MV and (b) Co^{60} beams.

For each scan, the sinogram data was averaged to give a 360 (views) x 80 (detectors) data set. In order to use the raw sinogram to reconstruct images, one needs not only the *scan data* but also the *air scan* and *dark current* data. The *dark* or *background current* is taken with the imaging system on and the beam off. The *air scan* is taken with the imaging system and the beam on, but without a phantom in place. Both of these are 1D arrays of 80 elements. Both the *scan d* the *air scan* must have the background subtracted from them. To corre temporal variation in the intensity of the photon source, the signal of etector outside the phantom shadow was taken as the reference signal

and was used to normalize the signal from all other detectors. The variations in the incoming radiation fluence from the source are known to cause ring artefacts in cone beam MVCT images (Partridge *et al.*, 1998). Pulse-to-pulse variations in the 6 MV beam were relatively large compared to the insignificant temporal variation in the Co^{60} beam. To get the ray integral for each view (λ_i) which is needed for image reconstruction, the dark and temporal-variation-corrected air scan (I_0) data was divided by the dark and temporal-variation-corrected phantom data I_i:

$$I_i = I_0 \exp(-\int \mu(r)dr); \tag{4.1}$$

where μ is the attenuation coefficient of the imaged object, as follows:

$$\lambda_i = -\ln\left(\frac{I_i}{I_0}\right) = \int \mu(r)dr \tag{4.2}$$

The division step in the equation above automatically removes the variation in the sensitivities among the detector elements. Hence, no flood field correction was necessary at this stage.

iv. Reconstruction

A parallel beam "filtered backprojection" (Kak and Slaney, 2001) method was employed to reconstruct CT images from the acquired fan-beam projection data after fan-to-parallel rebining. A projection is a set of line integrals. The simplest case for which one can acquire a projection is shown in figure 4.4 (a) where a collection of parallel ray integrals provides one "projection", P_θ , through an object $\mu(x,y)$ at angle θ. Parallel projections could be measured by moving an x-ray source and detector simultaneously across the object along a path oriented at angle θ with respect to x-axis as shown in figure 4.4 (a). For such a

simple case the filtered backprojection can be expressed as (Kak and Slaney, 2001):

$$\hat{\mu}(x,y) = \int_0^{\pi} Q_\theta(x\cos\theta + y\sin\theta)d\theta \tag{4.2}$$

$$Q_\theta(t) = \int_{-\infty}^{\infty} S_\theta(w)|w|e^{i2\pi wt}dw \tag{4.3}$$

$\hat{\mu}(x,y)$ is the reconstructed object distribution in the spatial domain; w, θ are the distance angle variables in polar coordinates in the Fourier domain, $S_\theta(w)$ is the Fourier transform of the projections P_θ at an angle θ . $Q_\theta(t)$ is the "filtered projection" and $|w|$ is the frequency response of a ramp filter.

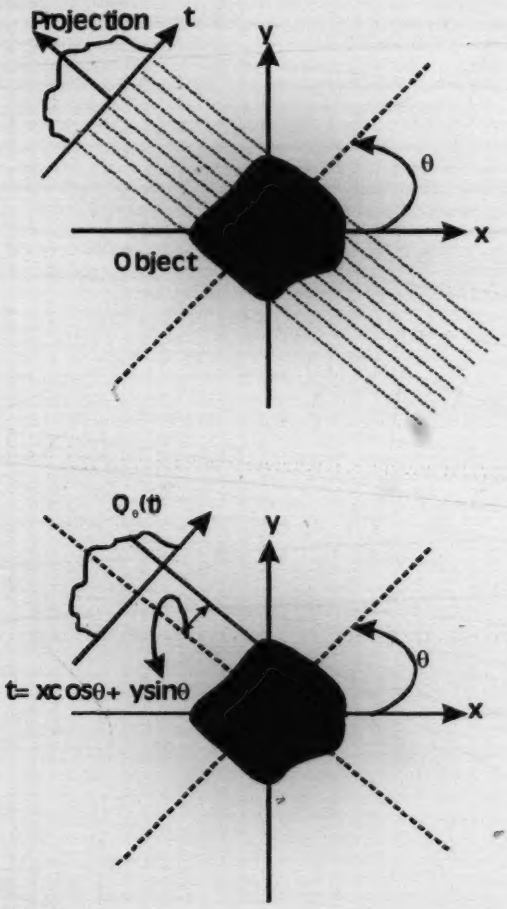

Figure 4.4: Parallel beam data collection geometry: (a) A set of line integrals at a rotation angle θ gives a projection for that angle. (b) The projected center of a pixel (x,y) as $t = x\cos\theta + y\sin\theta$ does not fall on a sampled locations of the filtered projection data $Q_\theta(t)$ in the spatial domain.

In this implementation of CT reconstruction, the ramp filter $|w|$ is impractical since it passes higher frequencies (where noise is prominent) as faithfully as the lower ones and it does not have a cut-off frequency. In our CT reconstruction, we employed the "Shepp-logan" filter which introduces a cut-off frequency (at the Nyquist frequency of rebinned parallel projection data) as well as apodizes the filter function by a Sinc function in frequency domain (Shepp and Logan, 1974). Moreover, during backprojection as shown in figure 4.4 (b), the projected center of a pixel (x,y) as $t = x\cos\theta + y\sin\theta$ does not usually fall on a sampled location of the filtered projection data $Q_\theta(t)$ in the spatial domain. A linear interpolation was used to assign a value for $Q_\theta(t)$ between the two neighbouring samples.

As shown in figure 4.1, we did not acquire the projection data in a parallel beam geometry; our system acquires its data in a fan beam geometry. The two equations below can be used to convert fan beam data sets to parallel beam data sets (Kak and Slaney, 2001):

$$t = SOD.\sin(\frac{x_F}{2SOD}) \tag{4.4}$$

$$\theta = \varphi_F + \frac{x_F}{2SOD} \tag{4.5}$$

t is the distance from each detector to the center of rotation in the object plane in parallel ray geometry; SOD is the distance from the source to the centre of object which is also the center of rotation; x_F is the arc length for each ray integral in the fan beam geometry; θ is the source and detector rotation in parallel geometry (same as θ in figure 4.4); and φ_F is the rotation of the axis of source and detector from the 0 position. Due to the *sin* function in equation (4.4) and because $x_F/2SOD$ is not exactly equal to 1° (angular interval of the fan beam data), bilinear interpolation is required in performing the coordinate transformation in equations (4.4) and (4.5). To find the exact distance between neighbouring detectors (needed for determining x_F) a radiographic film (Kodak

XV) was cut into a ~26 x 3 cm^2 strip and tightly packed into a light-tight envelope. The strip containing the film was snuggly taped at the back of the detector arc and exposed to obtain the radiograph of detector elements. The spacing between the detector blocks was measured by digitizing the film and establishing the geometric calibration of the film.

Figure 4.5: A radiograph of the 80 element detector array.

To reconstruct the 256 x 256 pixel images, fan-to-parallel rebinning and filtered backprojection programs utilizing the Shepp and Logan filter (Shepp and Logan, 1974) were written in MATLAB (The Mathworks Inc., Natick, MA). The fan beam sinogram was first zero padded to give parallel data with 360 projections, 89 data points in each projection with equal spacing of 3.15 mm between each consecutive data point.

v. Scan Dose

The set up for estimating the dose is shown in figure 4.6. The main assumption used in this set up is that the cylindrical geometry of the phantom can be approximated by a rectangular geometry. Hence instead of using a cylindrical phantom, rectangular slabs of solid water were used in this experiment. The collimators were opened to the same field size as used in the imaging geometry (4 x 21 cm^2 in Co^{60} along with extra collimation to make the field ~ 0.8 x 26 at the surface of the detector at SDD ~ 110 cm; 2.5 x 25 cm^2 in 6 MV). An ion chamber (Protea, Protea Corporation) was placed at a depth of 7.5 cm (radius of the CATPHAN500 phantoms); the distance from the source to the ion chamber was equal to the centre of LCR phantom in imaging geometry (70

cm in Co^{60} ; 90 cm in 6 MV) . The ion chamber reading was then recorded (D_1). The distance from the source to the ion chamber was changed to 80 cm for Co^{60} and 100 cm for the linac. The ion chamber depth was kept at 7.5 cm, while the field size was set to 10 x10 cm^2 at the isocenter. The reading of the ion chamber was recorded again (D_2). For all the readings 100 monitor units were delivered for 6 MV and 2 minutes of radiation for Co^{60}. The dose to the center of the phantom is then calculated by the following two equations:

$$D_{6MV} = \frac{D_1(6MV)}{D_2(6MV)} \bullet TPR(depth = 7.5cm; fs = 10x10cm^2) \bullet D_{cal}(depth = 1.5cm; fs = 10x10cm^2) \quad (4.6)$$

$$D_{Co^{60}} = \frac{D_1(Co^{60})}{D_2(Co^{60})} \bullet TAR(depth = 7.5cm; fs = 10x10cm^2) \bullet D_{cal}(fs = 10x10cm^2) \quad (4.7)$$

where *TPR* is the tissue phantom ratio dose conversion (Johns and Cunningham, 1983). The TPR is measured as the ratio of dose for given field sizes and depths in water relative to a 10x10 cm^2 field size at a depth of 1.5 cm (depth of maximum dose for 6 MV photons), the measurement probe being at the same distance from the source in both cases. *TAR* is the tissue to air ratio (Johns and Cunningham, 1983); it is measured at certain field sizes and depths in water relative to a 10x10 cm^2 field size in a small mass of tissue in air. D_{cal} in the calibrated dose for a 10x10 cm^2 field size at a depth of 1.5 cm in water in 6 MV beam and to a small mass of tissue in air for Co^{60} beam. *TPR* and D_{cal} for 6 MV are measured at 100 cm; *TAR* and D_{cal} are measured at 80 cm for Co^{60}. The dose in equation 4.6 is then multiplied by 94 MUs (delivered in 22.5 s) to get the imaging dose for 6 MV if every radiation pulse is utilized in reconstructing the image. For the Co^{60} beam, the detectors only integrate charge for 0.7 ms in each data cycle because the remaining time of a data cycle is used in reading the detector data. Generally the detectors in diagnostic CT integrate charge for the full cycle by utilizing dual integrators per detector element; however, this was not implemented in our simple circuit. Therefore, the image forming scan time in the Co^{60} beam was (15617 x 0.7 ms) 10.93 s. Thus the dose in the image geometry, estimated in equation 4.7 was multiplied by 10.93 s to get the imaging dose in Co^{60} beam if every data pulse is utilized in reconstructing them.

The dose to the center of the phantom was estimated to be approximately 17 and 60 cGy in Co^{60} and 6 MV beams when all the collected pulses were used in the reconstruction process.

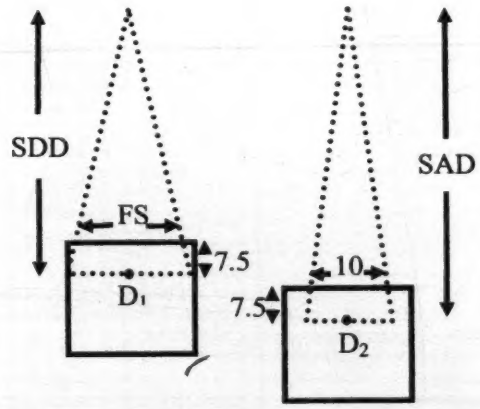

Figure 4.6: The set up for estimating the dose to the phantom: Rectangular slabs of solid water were used in this experiment. The collimators were opened to the same field size as used in the imaging geometry (FS). An ion chamber was placed at a depth of 7.5 cm; the distance from the source to the ion chamber was equal to the distance used in the imaging geometry (SDD). The ion chamber reading was then recorded (D_1). The distance from the source to the ion chamber was changed to 80cm for Co^{60} and 100 cm for the linac (SAD). The ion chamber depth was kept at 7.5 cm, while the field size was set to 10 x10 cm^2 at the isocenter. The reading of the ion chamber was recorded again (D_2). For all the readings 100 monitor units were delivered for 6 MV and 2 minutes of radiation for Co^{60}.

In Co^{60}, images with doses of 8.5, 4.3 and 2.1 cGy were obtained by utilizing only one-half, one-fourth and one-eighth of the data pulses per revolution, respectively. In the 6 MV beam, we reconstructed the images with one-ninth of the data pulses to get results at less than 9 cGy. It should be noted that neither an increase in rotational speed nor a reduction in dose output rates (i.e. per pulse) of teletherapy units was practical. The number of pulses of data averaged per degree reduces significantly when a larger fraction of pulses is thrown away. This procedure of reducing image forming dose results in inferior image quality due to sparser angular sampling when compared to the case when the entire number of pulses are utilized and dose per pulse is reduced

proportionately. Other investigators (Pouliot *et al.*, 2005) have windowed the pulse rate of a linac (Siemens Primus, Siemens Medical Solutions, Concord, Ca) so that only a fraction of the number of pulses were delivered. So the angular dose rate was reduced. Similarly in Tomotherapy™ machines, the pulse rate is reduced from 296 Hz to 80 Hz for the imaging mode. However, since we have no way of doing so, our images for 6 MV still have a high dose delivered to the center of the image and are not clinically relevant.

vi. Artefacts

a. Beam Hardening

In kVCT imaging, beam hardening artefacts, manifest as a distinct dark circular region inside the image of a uniform circular phantom. In the kV range, the attenuation coefficient of most tissue-like materials decreases with energy. Therefore in a polychromatic x-ray beam incident on a phantom, the lower energy photons are preferentially absorbed so the remaining beam becomes higher in energy or "harder". Therefore, in a circular phantom more beam hardening occurs in the central part of the phantom where there is more material, than in the peripheral region where the ray path through the phantom is shorter. Hence, the attenuation coefficient is recorded as lower in the central region of the phantom (Joseph *et al.*, 1978).

Even though Co^{60} decays with two gamma rays at 1.17 and 1.33 MeV, the spectrum of photons from the encapsulated source contains other components. A detailed review of spectral measurements for different forms of capsule is given in ICRU report 18 (1971). The thick target bremsstrahlung spectra from linear accelerators are also poly-energetic with the central region of the beam higher in intensity than the peripheral region. In clinical linear accelerators a flattening filter is placed in the path of the beam to make the intensity of the beam uniform across the clinical treatment field. This filter is conical in shape so that it absorbs more of the central photons than the peripheral photons. Hence the beam emerging from the central region of the flattening filter is higher in energy than the peripheral. This "harder" beam will have a lower attenuation coefficient

in a patient's body than the peripheral beam. Therefore, the source of beam hardening in the central region is no longer due only to the shape of the imaging object, a major contribution is also due to the shape of the flattening filter. The peripheral beam is hardened more in the phantom.

In order to correct for the beam hardening artefacts in our phantoms in Co^{60} and 6 MV photon beams, the following experiment was carried out. Slabs of solid water (11 slabs, each 2 cm thick) were placed in the path of a narrowly collimated Co^{60} beam (~0.6 x 20 cm^2 at 80 cm from the source = the imaging beam size) on top of the treatment couch, and the detector was placed under the treatment couch at a distance of 110 cm from the source. The source to couch top distance was 68 cm. The beam was collimated before it hit the solid water; i.e. the same collimation as the imaging geometry was used. Hence no post phantom collimation was done. For each thickness of solid water (z), 6000 readings for each detector element were taken. Therefore, the attenuation measurements were carried out for all the detectors at the same time and *not* for each detector individually. The dark current was subtracted from the mean of these points to give the detector signal $I(x)$, where x is the path-length (different from z due to divergence) through solid water for each detector. The attenuation was calculated as $y(x) = Ln[I(0)/I(x)]$ for each path-length and detector channel, where $I(0)$ is the detector signal for the open beam. The function $y(x)$ was fit to a second order polynomial in 'x', and the first (α) and second (β) order coefficients were obtained for each detector while the intercept was forced to be zero. The coefficients of the second order polynomial were used to convert the measured attenuation for each detector, in the imaging experiment, to the equivalent solid water thickness. To study beam hardening at 6 MV, the same procedure was performed with some minor differences. The source to couch top distance was 90 cm, and 1000 points were taken for each detector reading and each solid water thickness.

b. Ring Artefacts

We found ring artefacts to be the most debilitating problem in assessing the quality of the images. Ring artefacts are a common problem in third generation CT scanners; they are caused by slight imbalance in the response of different neighbouring detectors and show up as vertical bars in the sinogram. Lewis *et al.* (1992) used a method called "sinogram filtering" to remove ring artefacts in their system. Since these artefacts appear as vertical lines in sinogram space, in the corresponding Fourier domain they fall at zero frequency in the variable conjugate to angle and at a broad spectrum of frequencies in the variable conjugate to distance, thus, can be filtered out. We found that the ring artifacts in our system are too strong to be corrected in this manner. Moreover, a close examination of these artefacts shows that they always appear at the end detectors of each 8-element array (figure 3.2).

To assess the signal at the end detectors, the line spread function (LSF) in detectors 24 and 25 (neighbouring end detectors on the third and fourth 8-element arrays) and detector 29 (the fifth detector on the fourth 8-element array) was assessed. The beam was collimated to a very narrow slit (~ 0.1 cm) in the 0.275 cm direction, using two lead blocks of 5 x 10 x 25 cm^3 and centered on detector elements to obtain the LSF. The signals of the central detector as well as its four neighbouring (two to the left and two to the right) detectors were obtained. These data were normalized to the total signal in the five crystals to give the five point LSFs centered at detectors 24, 25 and 29. The LSFs at the end detectors (24, 25) were found to be significantly asymmetric compared to that at the central detector (29), because the end detectors are separated by air spaces instead of *gelcoat*.

In order to study how the asymmetric LSFs at the end detectors in 8-element arrays affect the attenuation measured by the system, a simple simulation was carried out. The attenuation of Co^{60} after passing through a 15 cm diameter cylinder of water in fan beam geometry similar to our system was calculated. The signal spread due to the LSF was calculated by superposition of

the calculated beam attenuation and the corresponding LSFs. In the simulation, the left corner detectors on each 8-element array (1,9,17...73) are assumed to have the same LSF as detector 24. Similarly, the right corner detectors (8, 16, 24 ...72) are assumed to have the same LSF as detector 25; all the remaining detectors are assumed to have the same LSF as detector 29. The ring artefacts seen in the simulated images (figure 4.10 d) are similar to the ones in the experimental images (figure 4.10 e). Therefore, the ring artefacts are caused by the asymmetric LSFs at the end detectors. We tried to fill the air gaps in between the 8-element blocks with silicon glue, but found it to be impractical for this detector design. A more practical detector design would eliminate these air gaps and would bond all the crystals together in a similar fashion. Since it was impractical for us to build the detector again, a different approach was taken to remove these ring artefacts. Every time a phantom was imaged, an image of the uniform phantom (CTP486) was taken as well. This image was reconstructed and contained ring artefacts at end detector locations (e.g. figure 4.10e). A simple code was written in MATLAB, which measures the diameter of the reconstructed image and creates a uniform mathematical phantom of the same diameter. This uniform phantom is then re-projected using the same geometry as in the imaging set up. The angular mean of the re-projected data is compared to the angular mean of the measured projection data of CTP486 to obtain a normalization factor for each *end* detector. This normalization factor which hereafter is referred to as the "calibration factor" is used to correct all the projections taken from the other phantoms in this set up. It should be noted that a similar approach was taken by Seppi *et al.* (2003) in order to obtain artefact free images in their MV CBCT system.

c. Centre of Rotation

A minor problem that was occasionally observed was a "halo" artefact around circular objects. An example of such artefact is shown in figure 4.7; this image also suffers from ring artefacts. The "halo" artefact is a result of misaligning the detector/phantom such that the central detector is shifted. The

problem can be resolved during the filtered backprojection process by determining the correct central detector.

Figure 4.7: An example of an image with both ring and center-of-rotation artefacts. See page 120 for the artefact free image.

d. Incorrect Fan Beam Rotation

Another problem which occurred only occasionally, was the presence of "out of focus" artefacts as shown in figure 4.8. The source of this artefact is not recognizing the direction of rotation for the phantom on the bench-top rotary stage. If the phantom is rotating in the clockwise direction, but in the reconstruction software, the rotation is indicated as counter-clockwise or vice versa, artefacts similar to figure 4.8 appear. As with the centreing artefact, once the source of the problem is recognized, the solution is straight forward and performed in the reconstruction software.

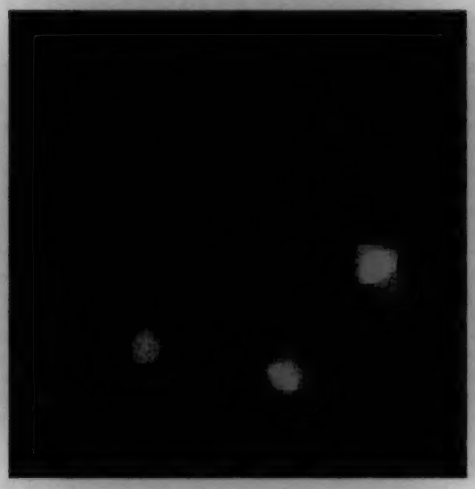

Figure 4.8: An example of an image with incorrect-fan-beam-rotation artefact. See page 120 for the artefact free image.

vii. Image Assessment

Once all the corrections were carried out we had 256 x 256 pixel images of different phantoms at a slice thickness of 8 mm. For the purpose of positioning patients, it is important for the observer to be able to at the very least distinguish between bone tissue and soft tissue (high contrast resolution); in an ideal situation the observer would be able to differentiate among several different soft tissue materials (low contrast resolution). The effect of a detector on the LCR in a CT image is a result of the absolute signal differentiation of the detector as well as the noise added by the detector. Therefore, the dependence of the SNR and LCR of the system on the image forming dose delivered to the center of the phantoms was studied. The LCR as a function of object size, as well as the spatial resolution and the linearity of the CT numbers with electron density were investigated. All the image assessments were carried out for the Co^{60} images.

According to Barrett *et al.* (1976), SNR^2 is proportional to the dose in CT images. The SNR at the center of an MVCT image of the CTP486 uniform module was measured in a circular region with a physical diameter of approximately 13 cm for doses of 17, 8.5, 4.3 and 2.1 cGy.

The LCR CTP612 phantom was used to assess the low contrast resolution of the system as a function of dose using the following relationship:

$$C = \frac{\mu_{object} - \mu_{reference}}{\mu_{reference}} \qquad (4.8)$$

where μ_{object} is the attenuation coefficient of one of the 2 cm cylinders of the three contrast levels in the CTP612 and $\mu_{reference}$ is the attenuation coefficient of the background material in CTP612. The dependence of low contrast resolution on object size was investigated in the CTP612 for the dose of 17cGy for the different diameters of targets at the three contrast levels.

Images of the electron density phantom and the CTP528 for a dose of 2.1cGy were taken to assess the linearity of the CT numbers with material density and the spatial resolution of the system respectively. Images of the Alderson Rando phantom are presented for visual evaluation.

B. Results and Discussion

i. Data Processing and Reconstruction

a. Beam Hardening

The first and second order coefficients of the quadratic curves fit to the attenuation data for each detector are shown in figure 4.9. It is observed that the magnitude of the first order coefficient in the Co^{60} beam is on average 700 times greater than the second order coefficient, and there is a very small variation in the attenuation (α) measured by each detector (mean= 0.0688 cm^{-1}, standard deviation= 0.002). Moreover, images of the uniform phantom (not included here) do not show a noticeable bowl artefact. Since beam hardening is not a significant problem in our experiments for Co^{60}, the correction for beam hardening artefacts may be ignored while using the detector in this beam. However, in the images presented in this chapter, this correction was carried out. Beam hardening is slightly more significant for the 6 MV beam.The relative magnitudes (notice the negative sign on the second order scale) of these coefficients increase for the detectors away from the central axis. This is due to the presence of the conical shaped flattening filter in the 6 MV beam. At the center of the field, the beam has a smaller fraction of low energy photons compared to a point off axis. Therefore, the mean photon energy decreases at off-axis points resulting in a larger first order coefficient. It is necessary to perform the beam-hardening correction to account for both the decrease in the mean energy and the softening of the spectrum away from the central axis in the 6 MV beam.

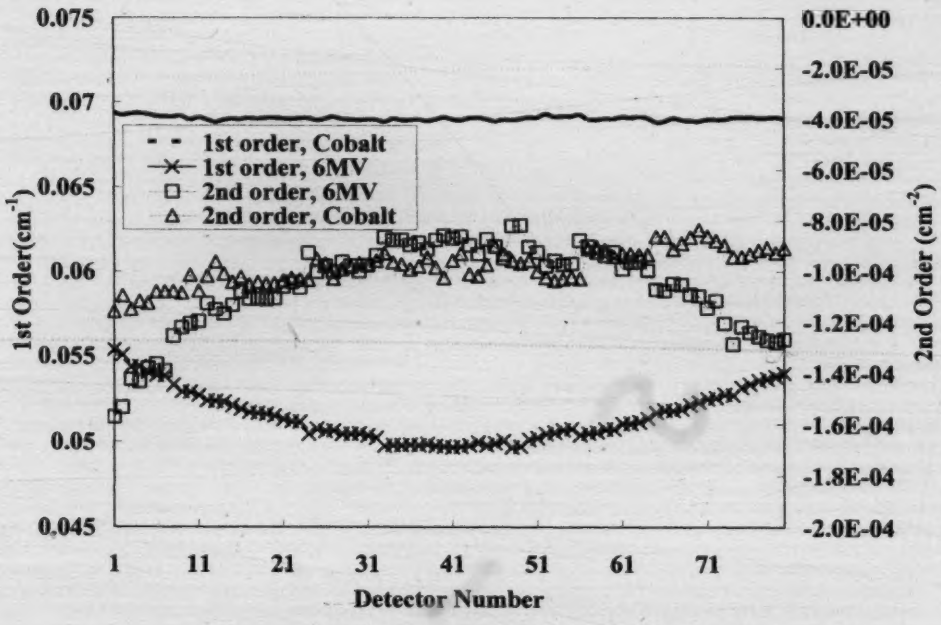

Figure 4.9: The first order, α, and the second order, β, terms of the polynomial fit to the measured attenuation of 6 MV and Co^{60} beams by solid water.

b. Ring Artefacts

Figures 4.10 a,b,c show the LSF of detectors 29, 25 and 24 in the Co^{60} beam. It is clearly observed that the LSF of detector 29 is symmetric, while the LSFs of detectors 24 and 25 are strongly asymmetric. Moreover, it is seen that these two asymmetric LSFs are almost mirror images of each other; in both cases the signal to the neighbouring detectors in the same block is higher than the corresponding neighbouring detectors in the adjacent block. Figure 4.10 d shows the result of applying these LSFs to the re-projected data of a uniform phantom in the simulation. Ring artefacts similar to those in the experimental image (Figure 4.10 e) are observed. This similarity suggests that the ring artefacts are caused by the asymmetry in the LSFs at the end detectors in the 8-element detector blocks. These artefacts are removed by the normalization scheme mentioned in the Materials and Methods section of this chapter. The results of applying various corrections to the projection data are presented in

figure 4.11. In this figure, a relative intensity profile through the center of the MVCT image for the 6 MV beam of the uniform phantom is displayed at various steps in the correction process. The first profile denoted as "base correction" is obtained from the reconstructed image after applying the correction for "dark current" and "pulse-to-pulse" variation in the 6 MV beam. A significant cupping due to the beam hardening and variation due to the asymmetric LSF at the block ends is visible in this profile. The cupping artefact is almost removed after applying the beam hardening correction; however, large variations in the relative intensity profiles due to the asymmetric LSF are visible. These variations are at similar locations to the ring artefacts seen in the images of uniform phantoms, e.g. in 4.10(e). The final flat profile, denoted as "after applying calibration factors" in figure 4.11, is obtained after applying the calibration factors. Although the calibration factors are derived by applying the asymmetric LSF to the simulated projection data for the uniform water phantom, the application of the calibration factors to the projection data for every other phantom used in this chapter reduced the ring artefacts in the corresponding images. If the entire 80-element array was bonded into one uniform detector arc, these ring artefacts would have been completely avoided. Therefore, thick scintillation crystals must be bonded uniformly in the detector array instead of using small building blocks joined together to form the entire array.

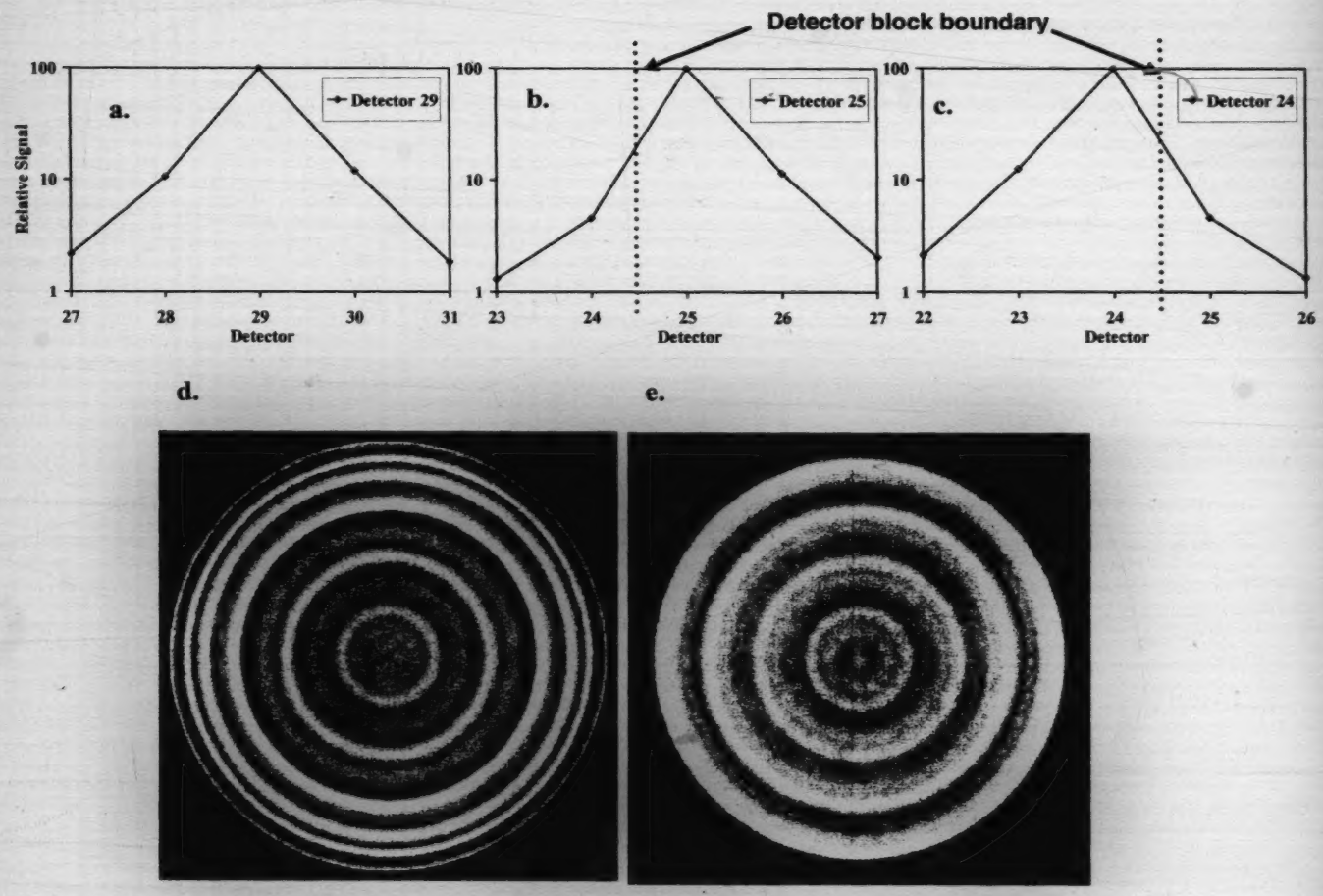

Figure 4.10: (a,b,c) The normalized LSFs of three detectors in different locations in one block: 29 (middle of the third block), 25 (left corner of the third block), 24 (right corner of the third block); (d) The result of applying these LSFs to the simulated projections of a uniform phantom (diameter = 15 cm); ring artifacts similar to the experimental image (e) are observed.

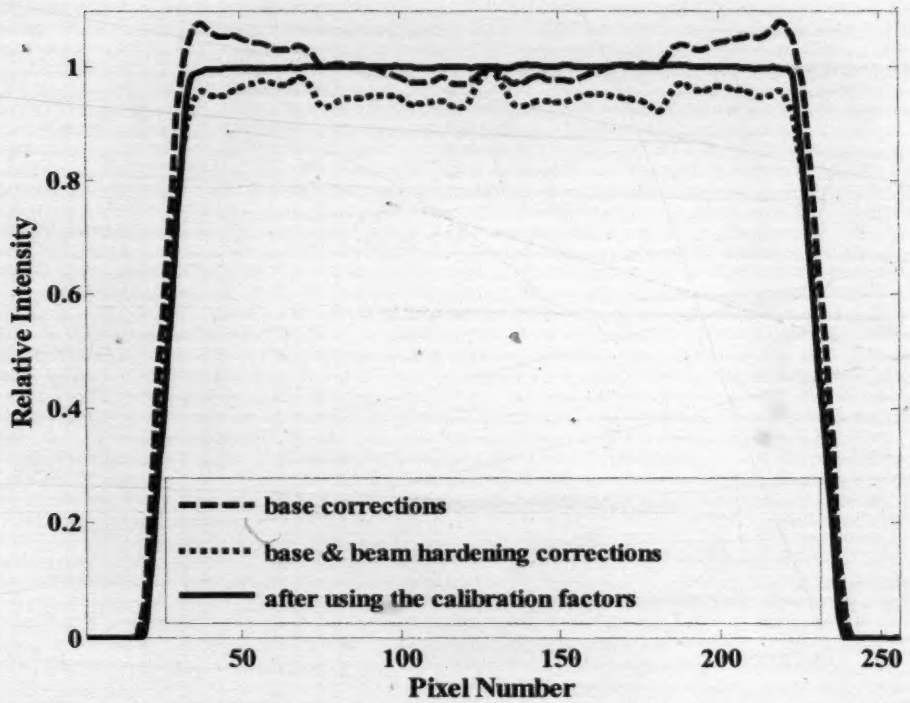

Figure 4.11: Relative intensity profiles through the reconstructed image of the uniform phantom in the 6 MV beam after applying various correction steps. Base correction includes the dark current and pulse-to-pulse variation. The beam hardening and calibration factors are described in the text.

ii. Image Assessment

Figure 4.12 shows the dependence of SNR^2 on dose, obtained from the uniform phantom images in the Co^{60} beam. The linear fit is very good with R^2 = 0.9977. Therefore, the SNR^2 is linearly proportional to the radiation dose used in forming the image. This result also indicates that the noise in the resulting MVCT images is determined mainly by the quantum noise.

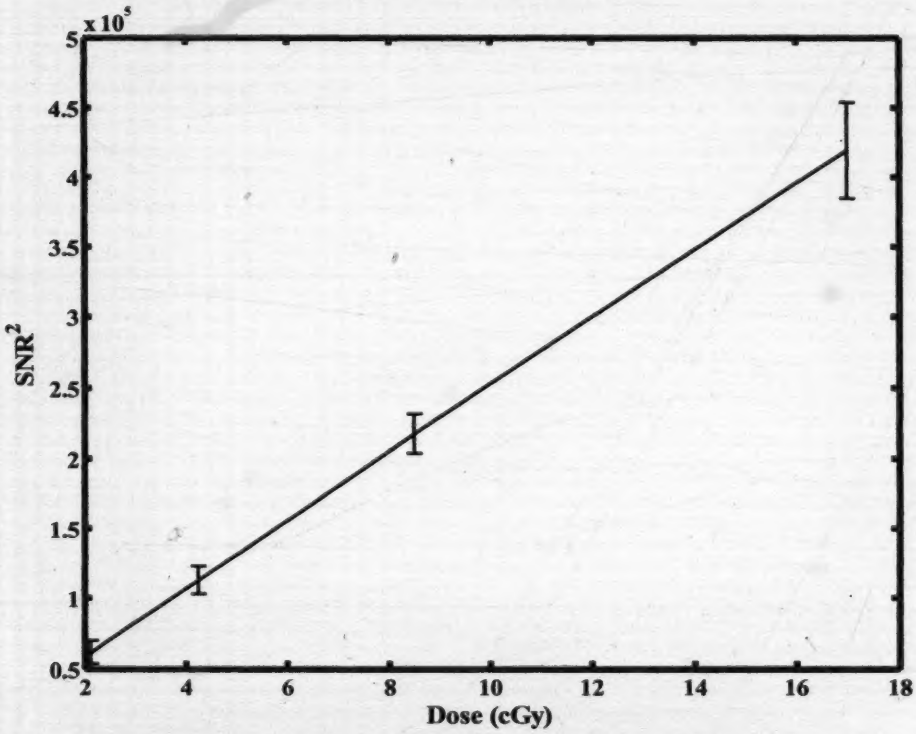

Figure 4.12: The dependence of SNR^2 on dose in MVCT images of the uniform phantom in the Co^{60} beam. The best fit line has R^2 = 0.9977.

Figures 4.13(a) through 4.13(d) show the images of the LCR CTP612 module at four different dose levels. These images qualitatively illustrate the interplay of contrast and SNR in our system for the Co^{60} beam. The large cylinders are visible at all contrast levels when there is a four-fold reduction in dose. It is clear that the lower SNR decreases the visibility of smaller objects in the phantom as the dose decreases. However, the small cylinder at the center, of 1.5 cm diameter at the nominal contrast level of 1.5%, is visible in all images. The image reconstructed with 2.1 cGy dose still shows the 0.6 cm and 0.7 cm cylinders while the 0.4 cm and 0.5 cm cylinders are nearly merged due to the poor spatial resolution resulting from throwing away seven-eighths of the angular projections. These results cannot be directly compared to the results of other investigators since the specialized module of the CATPHAN500 phantom was built only for this work and has never been used previously. The difficulty associated with assessing the LCR with inserted contrasts was alluded to by Seppi *et al.* (2003) as arising because the boundary between the host phantom and the inserted targets makes the targets easy to visualize. Seppi *et al.* (2003) estimated a contrast resolution of 1% for their CsI-based MVCT system using a radiation dose of 16cGy. The bench-top MVCT described by Ruchala *et al.* (1999) obtained an LCR of about 2% for relatively large size (≈ 20 mm) embedded discs using 8 cGy of dose.

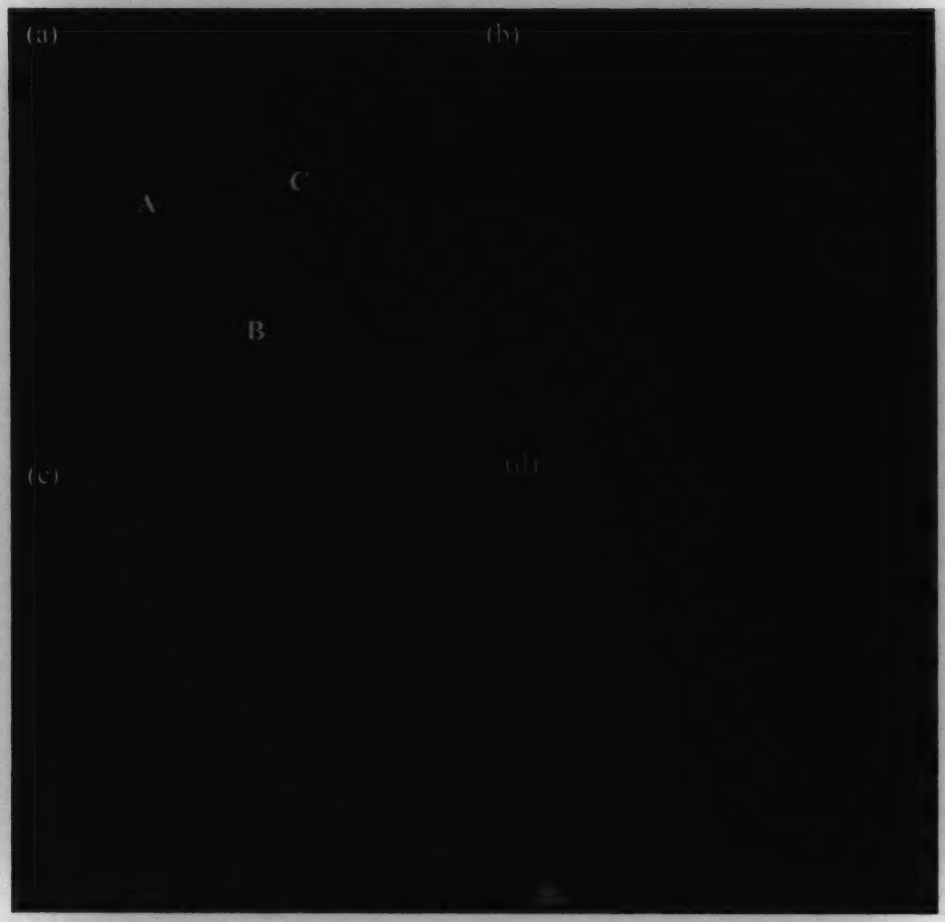

Figure 4.13: Images of CTP612 (diameter = 15 cm) at four different dose levels, (a) 17cGy, (b)8.5 cGy, (c)4.3 cGy, (d)2.1 cGy. Groups A, B and C have experimental contrasts of 2.8%, 1.9% and 2.1% respectively while the cylinder in the middle has a contrast of 1.5% for Co^{60} with respect to the background material in the phantom. All images are windowed and levelled the same way.

Figure 4.14 shows the contrast of the largest circle in each group as a function of dose. The contrast values obtained from the lower dose images are plotted as a function of the contrast calculated from the 17 cGy image. It is seen that, as the dose decreases, the contrast in the objects is approximately constant. Therefore, any detector calibrations performed at higher dose levels still hold at lower dose levels. Figure 4.15 shows how at 17 cGy the contrast is related to object size. The general trend is that the contrast decreases as the object size decreases. Similar results are obtained at the other dose levels.

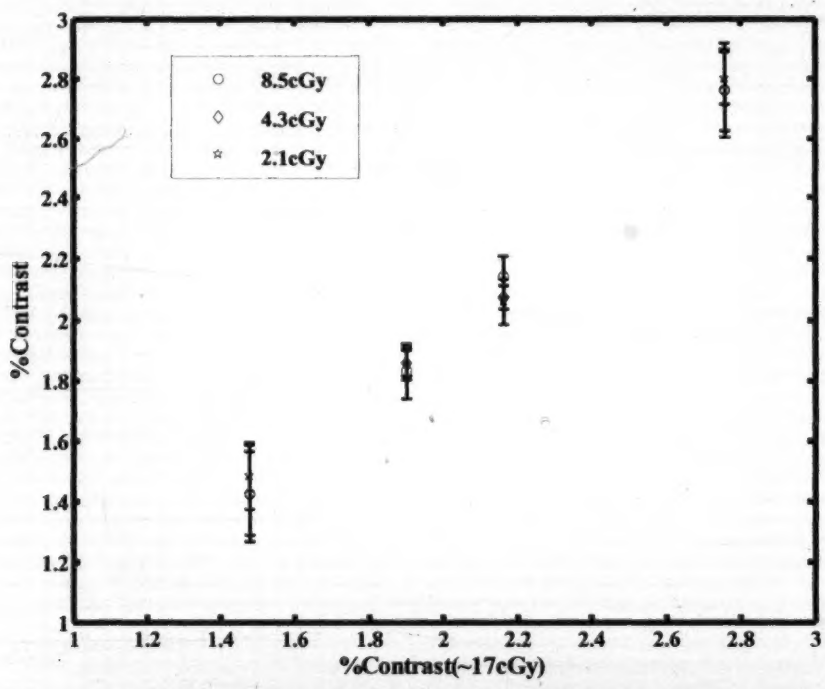

Figure 4.14: The contrast of the 17cGy scan of CTP612 module is compared with the contrast obtained at more clinically viable doses of 8.5, 4.3 and 2cGy. The largest cylinder in groups A, B and C (see figure 4.13) as well as the cylinder in the middle were used in this comparison.

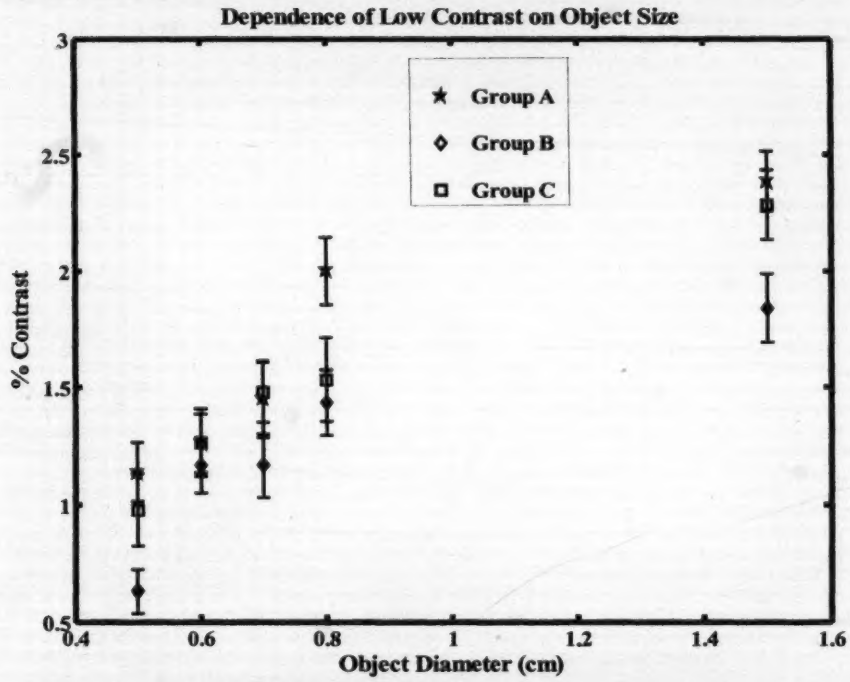

Figure 4.15: The contrast of objects of different sizes in the CTP612 module at 17cGy. See Figure 4.13 caption for contrast levels in groups A, B and C.

Due to the large size of the Co^{60} source (2cm) and the relatively large detector pitch, the system suffers from poor spatial resolution. This is shown in figure 4.16 where only 1 line pair per cm is observed. The smaller source size offered by a medical linear accelerator will provide improved spatial resolution.

Figure 4.17 illustrates the linearity of the CT numbers as a function of the density of the objects at a radiation dose of 2.1 cGy. As found by other investigators, the CT numbers are fairly linear with the density of objects. R^2 = 0.9923 was calculated by the linear regression of CT numbers and density of inserts. The image of the in-house phantom is also shown in Figure 4.17.

Figure 4.16: Image of the spatial resolution phantom (diameter = 15 cm) at 2.1cGy. The spatial resolution of the system is 1 line pair per cm for Co^{60} beam.

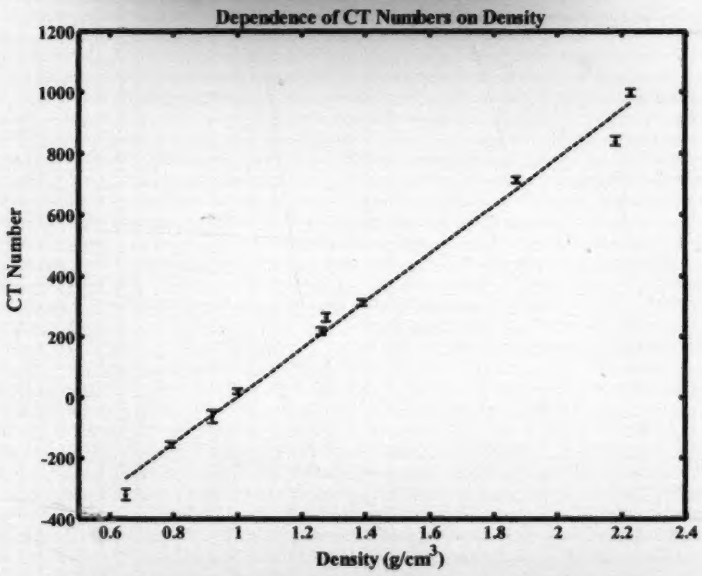

Figure 4.17: Image of our in-house density phantom (diameter = 19.1 cm) obtained at a dose of 2.1 cGy. The CT numbers are linear with density with R^2 = 0.9923. The key for the arrangement of density plugs is provided in section A.ii.

Figure 4.18: Images through slices 6 and 7 of the Rando phantom. The center of the phantom was placed at 80cm from the source in the Co^{60} beam. The dose used to obtain these images was 2.1cGy.

The MVCT images of the two slices of the Alderson Rando phantom at 2.1 cGy are shown in Figure 4.18. The images clearly demonstrate the limited anatomical structures in the phantom including teeth, air cavity and other bone-like tissue.

C. Conclusions

The ultimate goal of our work is to create a focussed 2-D MV detector with high DQE such that reasonable LCR at low dose can be obtained in MVCT. As an initial step we have fabricated a 1-D array of 80-elements containing $CdWO_4$ and photodiodes, placed it on an arc with a radius of 110 cm and added a rotary stage to create a third generation CT scanner. We have presented the imaging characteristics of this scanner for Co^{60}. While reconstructing images from this scanner, the most persistent problem was the presence of ring artefacts. The measured contrast of the system as function of dose was shown to be fairly constant, while at a fixed dose the contrast decreased as the object size decreased. The SNR of this system was shown to be proportional to the square root of dose. Most importantly, the low contrast resolution of 1.5% for an object of size 0.6 cm was achievable at a radiation dose of 2.1 cGy. The spatial resolution

in Co^{60} beam was limited to 1 line pair per cm due mainly to the size of the Co^{60} source and the detector pitch.

D. References

H. H. Barrett, S. K. Gordon and R. S. Hershel, "Statistical limitations in transaxial tomography," Comput. Biol. Med. **6**, 307-323 (1976).

J. Hsieh, *Computed Tomography: Principles, Design, Artifacts, and Recent Advances* ,SPIE Press, 2003.

ICRU, "Specification of high-activity gamma-ray sources," ICRU Report 18, ICRU, Washington, D.C. (1971).

H. E. Johns and J. R. Cunningham, *The Physics of Radiology*, 4th ed. (Thomas, Springfield, IL, 1983).

P. M. Joseph and R. D. Spital, "A method for correcting bone induced artifacts in computed tomography scanners," J. Comput. Assist. Tomogr. **2**, 100-108, (1978).

A. C. Kak and M. Slaney, *Principles of Computerized Tomographic Imaging*, Society of Industrial and Applied Mathematics, 2001.

D. G. Lewis, W. Swindell, E. J. Morton, P. M. Evans, and Z. R. Xiao, "A megavoltage CT scanner for radiotherapy verification," Phys. Med. Biol. **37**, 1985-1999 (1992).

M. Partridge, P. M. Evans, and M. A. Mosleh-Shirazi, "Linear accelerator output variations and their consequences for megavoltage imaging," Med. Phys. **25**, 1443-1452 (1998).

J . Pouliot, A. Bani-Hashemi, J. Chen, *et al.*, "Low dose megavoltage cone beam CT for radiotherapy", Int. J. Radiat. Oncol. Biol. Phys. **61**, 552-560 (2005).

K. J. Ruchala, G. H. Olivera, E. A. Schloesser and T. R. Mackie, "Megavoltage CT on a tomotherapy system," Phys. Med. Biol. **44**, 2597-2621(1999)

K. J. Ruchala, G. H. Olivera, E. A. Schloesser, *et al.*, "Calibration of a tomotherapeutic MVCT system," Phys. Med. Biol. **45**, N27-36 (2000).

E. J. Seppi, P. Munro, S. W. Johnsen, E. G. Shapiro, C. Tognina, D. Jones, J. M. Pavkovich, C. Webb, I. Mollov, L. D. Partain, and R. E. Colbeth, "Megavoltage

cone-beam computed tomography using a high-efficiency image receptor," Int. J. Radiation Oncology Biol. Phys. **55**, 793-803 (2003).

R. G. Simpson, C. T. Chen, E. A. Grubbs, and W. Swindell, "A 4-MV CT scanner for radiation therapy: The prototype system," Med. Phys. **9**, 574-579 (1982).

L. A. Shepp and B. F. Logan, "The Fourier reconstruction of a head section," IEEE Trans. Nucl. Sci. **21**, 21-43 (1974).

Chapter 5

Monte Carlo Study: Detector Design

The first phase of this project has been described in an earlier thesis (Monajemi, 2004). In that first phase, we used Monte Carlo (MC) simulations of both x-ray/γ-ray and optical photon transport to predict the imaging characteristics of a 1 cm tall, eight element array of $CdWO_4$ crystals in contact with photodiodes; the MC predictions have been verified by measurements made in Co^{60} and 6 MV beams. For the second phase of the project, we have built an arc-detector composed of an eighty element array of 1 cm tall $CdWO_4$-photodiodes and studied its imaging characteristics (Rathee et al., 2006; chapter 3). The same detector has been coupled to a rotary stage to build a bench-top third generation MVCT scanner; a preliminary set of images has been taken and analyzed using this scanner (Monajemi *et al.*, 2006; chapter 4). The natural next step in this study is expanding this detector to an area imaging system, i.e. a system that is capable of imaging more than one slice at a time leading to a cone beam system, and exploring its imaging capabilities. Before doing so however, we need to answer a few questions regarding the design parameters of the new area detector including scintillator dimensions, x-ray and optical properties of septa material, and effects of beam divergence, system magnification, and patient scatter on the imaging performance of the detector. The previously studied two-step MC simulation approach is a convenient technique of manipulating different design parameters and calculating the resulting change in the imaging performance of the detector. This MC approach allows simulation of x-ray interactions within the scintillation material and subsequent transport of secondary optical photons to the photodiodes. Therefore this approach is both

more suitable and economical to study the impact of design parameters on the image performance of the detector than the experimental methods.

In writing this chapter each section (i.e. Introduction, Theory, Materials and Methods.....) is divided into two parts. The first part deals with a segmented detector geometry where optically opaque and reflective septa separate the individual scintillation elements of the virtual area detector, while the second part examines a continuous slab of the scintillator and does not consider the optical transport as explained in section B.ii of this chapter. The first part answers the following questions: (1) What effect do the septa material and crystal height have on the imaging performance of the detector? (2) If we implemented this detector on a Hi-Art II TomoTherapy™ unit that delivers a relatively lower energy photon spectrum for the imaging beam, how would the theoretical imaging characteristics change? and finally (3) What effect does beam divergence have on the imaging characteristics of this thick segmented detector? The second part is only concerned with the $MTF(f)$ of the entire imaging system, and aims to answer one specific question: How small do we need to make the pixels (element size) considering the effects of source size, system magnification and patient scatter? These three parameters determine the spatial resolution in the images in addition to the inherent signal spread within the detector, and thus may impact the element size of the detector. The answer to this question is very important as $CdWO_4$ cannot be made less than 1 mm in both the x and y directions due to the presence of a cleavage plane (Kinloch *et al.*, 1994).

A. Introduction

i. Imaging Characteristics of the Detector

One of many advantages of using crystalline scintillation materials for MV imaging is that they lend themselves to segmentation and hence optically opaque and reflective septa can be used to prevent spreading of optical photons from one detector element to another. If at the same time the optical yield and transmission are favourable, the dimension of high density scintillation crystals in

the beam direction (i.e. height) can be increased to achieve high *quantum efficiency (QE).* High QE means that a large fraction of the incident beam will interact in the scintillator. When increasing the scintillator height, it is necessary to study the signal created in the optical sensors as a function of crystal height. While the MV energy deposition increases as the crystal height is increased, a lesser fraction of the optical photons created in the top layers reaches the optical sensors placed at the bottom of the crystal both due to self-absorption within the crystal and absorption within the septa. Therefore the first step in choosing the optimum height for a crystal is to study the signal generated in the crystal and to find the height that creates the optimum signal. Simultaneous study of the secondary electron and optical photon spread in the scintillator-photodiode detector is required to ensure optimal spatial resolution. Since the optical photons are created istropically (Mosleh-Shirazi *et al.*, 1998) and scatter as they travel within the scintillator, the scintillator crystals should be segmented to minimize the loss of spatial resolution. (Mosleh-Shirazi, 1998, Sawant et al., 2005) Appropriate septa materials can be placed between segments to stop the spread of optical photons from one crystal to another. The septa material should be highly opaque and reflective to avoid optical spread to the neighbouring segments and at the same time direct the optical photons that are generated within one segment towards the corresponding optical sensor. When choosing a septa wall material and its thickness, it is necessary to look at the overall signal (i.e. MV energy deposition and optical signal transport) of the detector as a function of septa material and thickness. Septa material can be made of high or low density materials. The effect of high and low density septa on the *DQE(f)* of scintillator-photodiode based detectors when ignoring the effect of optical photons has been studied earlier (Sawant *et al.*, 2005). In their results, the authors state that the best combination of detector and septa material are high density crystals with high density septa materials. $CdWO_4$ and W are an example of such a combination. One of our goals in this chapter is to see if their conclusion still holds if the effect of optical photons is considered.

Another issue which becomes increasingly important for tall scintillation crystals is the effect of beam divergence on the imaging characteristics of the detector since the off-axis beam is incident obliquely on the detector elements mounted on a flat surface. Thus obliquely incident rays may travel through more than one detector element causing a spatial spread in the detector signal. Sawant *et al.* (2005) and Pang and Rowlands (2002) provide a schematic cross-sectional view of an idealized segmented detector. The detector consists of optically isolated crystals, the center-to-center spacing of the segmented scintillator elements equals the pixel pitch of the active matrix photodiode array, and the individual septa between the segmented scintillator elements are focused towards the MV source. If the detector is not focused the angle of beam incidence on the detector varies across the area of the detector.

The focus of the first part of the present study is on the effects of different detector parameters, namely scintillation crystal height, septa material, beam divergence and beam spectrum on the frequency dependent spatial resolution and DQE at zero frequency of a hypothetical area detector based on segmented $CdWO_4$ crystals and silicon photodiode arrays.

ii. $MTF(f)$: Entire System

An entire treatment-position-based imaging system consists not of the detector alone but also the focal spot and the patient as shown in figure 5.1. Therefore, the size of the focal spot, and the distance of the detector from both the focal spot and the patient affect the imaging characteristics of the detector. Our goal in this section is to study the effects of these system parameters on the spatial resolution, $MTF(f)$. Since our goal is to estimate the size of the smallest resolvable object in the patient plane, we look at $MTF(f)$ in the plane of the patient in this section. The motivation for this work came from the physical limitation that $CdWO_4$ crystals cannot be made less than 1 mm wide in both the x and y directions (Kinloch *et al.*, 1994) due to the presence of a cleavage plane. The specific question that we are trying to answer is how much this relatively large pixel size degrades the inherent spatial resolution, considering the effects

of other parts of the imaging system on the entire system $MTF(f)$. It is worth noting here that the inherent spatial resolution of a scintillator is a result of high energy photon interactions and secondary particles traveling within the scintillator as well as the spread of the resulting optical photons as shown in section i of the experiments in this chapter. However, for reasons discussed in section B.ii, simulations did not consider the effects of optical photons in this portion of the study. Nonetheless, the general conclusions drawn from the simulation results of the focal spot, patient scatter and system magnification which is related to the distance of the detector from both the source and patient planes, still hold and can serve as general guidelines in the future design of this detector.

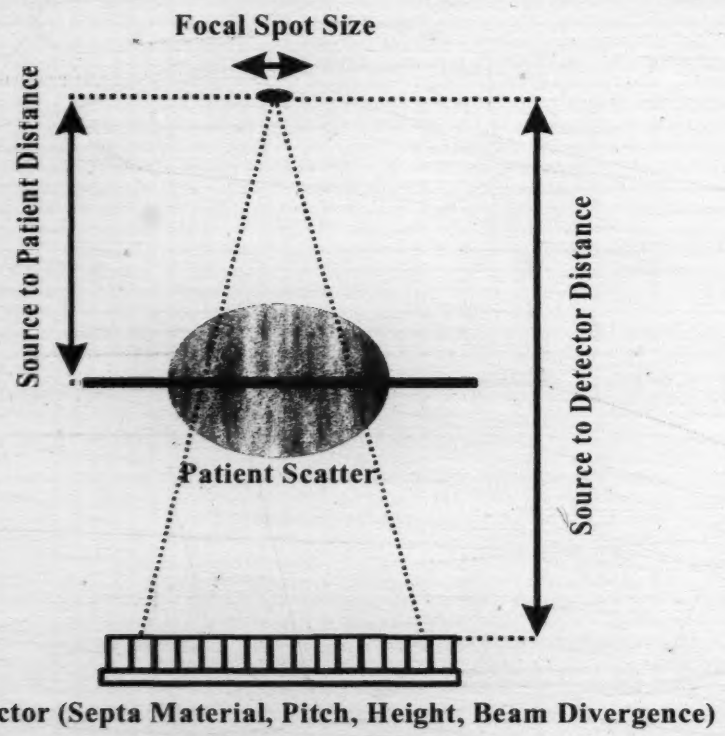

Figure 5.1: Different system parameters which have been considered in this study for designing a cone beam MV detector. The cross-sectional view of the detector is shown as a linear segmented array as opposed to being focused on the *x*-ray source, to study the effect of beam divergence.

B. Theory

i. Imaging Characteristics of the Detector

As discussed in chapter 3, segmented detectors are shift-variant systems. While for spatially continuous detector structures (i.e. non-segmented), the study of these detectors as shift-invariant systems is intuitively justified, in a strict sense one cannot apply the concept of Fourier based image characterization parameters such as MTF, noise power spectrum, NPS and DQE to segmented detector systems, especially as the detector fill factor is decreased. Sawant *et al.* (2005) have shown that the concept of pre-sampling signal still applies to these detectors as long as the scintillator elements are registered exactly to the photodiode array elements. The proof is illustrated here in equation 3.9 through 3.16. In this work, the slanted slit technique (Fujita *et al.*, 1992) of obtaining the LSF_{pre} -illustrated in figure 3.8- is used to calculate MTF_{pre}.

$DQE(0)$ of a scintillation detector can be calculated by using the MV photon absorbed energy distribution function, AED, when the effect of optical photon transport is ignored and by using the photodiode signal's pulse height spectrum $P(S_{opt})$ when the effect of optical photons is included (Swank, 1973 and 1974; Jaffray *et al.*, 1995). The AED shows the distribution of deposited energy from each incident *x*-ray quantum in the detector through interactions such as photoelectric absorption, Compton scattering, and pair production. It provides the number of incident x-ray photons that deposit a specific amount of energy within the scintillator for a range of energies and it can be calculated using Monte Carlo simulation. $P(S_{opt})$ is the probability that an incoming *x*-ray interacts and that finally S_{opt} amount of relative current is produced in the photodiode. The relative photodiode current is calculated as the weighted summation of the incident optical photon spectrum by the wavelength (λ) dependent sensitivity spectrum, $\eta(\lambda)$, of the silicon photodiode. For example, if $N(\lambda)$ is the optical fluence incident on the photodiode for an incident *x*-ray quantum then the relative photodiode current is calculated as follows:

$$S_{opt} = \int N(\lambda)\eta(\lambda)\,d\lambda \tag{5.1}$$

The function $N(\lambda)$ is calculated using the two-step Monte Carlo method discussed in section C.i. Once the AED and $P(S_{opt})$ are known and binned into small enough intervals, the moments of these functions can be calculated as the following summations:

$$M_n = \sum_E AED(E)E^n \tag{5.2}$$

$$M_n = \sum_{S_{opt}} P(S_{opt})S_{opt}{}^n \tag{5.3}$$

where E is the amount of *x*-ray energy deposited in the scintillator. $DQE(0)$ in each case is calculated by:

$$DQE(0) = \frac{M_1{}^2}{M_2} \tag{5.4}$$

When finding the AED or $P(S_{opt})$ functions using Monte Carlo simulations for shift-variant segmented scintillation detectors, it is important that the incoming beam on the detector is either as large as the detector area or as large as the portion of the detector that identically repeats itself. For example in case of a segmented detector, the incoming beam must be at least as large as one detector element comprising scintillator and its surrounding septa material, and its central axis must coincide with the center of the element.

ii. $MTF(f)$: Entire System

The $MTF_{pre}(f)$ calculated in section B.i, only considers the signal spread due to MV and optical photons in the plane of the detector. However, in MV imaging, one is concerned with visualising objects in the plane of the patient. The important factors that affect the spread of a line in the plane of the object are the

photon fluence distribution of the source (source LSF denoted as $f(x')$), the signal spread in the detector (detector LSF denoted as $d(x)$), patient scatter and geometric magnification. The magnification is defined as the ratio of source to detector (*SDD*) and source to object (*SOD*) distances. In the absence of patient scatter, the source and detector LSFs are geometrically scaled in the object plane and convolved to give the *LSF* of the imaging system (Swindell *et al.*, 1991):

$$LSF_{sys}(x'') = f[x'' = \frac{x'(M-1)}{M}] \otimes d[x'' = \frac{x}{M}] \tag{5.5}$$

where x, x', and x'' are linear distances in the detector, source and object planes respectively and M is the geometric magnification. The MTF of the imaging system, $MTF_{pre}(f)$, is then obtained by taking the Fourier transform of equation (5.5).

The 2D distribution of energy deposited in the detector due to a pencil beam of MV *x*-rays is calculated using Monte Carlo simulations and then averaged along one dimension to obtain the 1D detector LSF. The object scatter can also be taken into account within equation (5.5) by making simple approximations. If the object is assumed to be a semi-infinite slab, then the lateral distribution of scattered radiation due to a pencil beam of MV *x*-rays becomes spatially invariant. Therefore, if the pencil beam is incident first on the slab objects in the Monte Carlo simulation of the detector LSF, the lateral distribution of scattered radiation becomes part of the exiting beam incident on the detector. The resulting detector LSF when used in equation (5.5) to calculate the system LSF will account for the object scatter. It should be noted that scattered radiation in patients is not spatially invariant; the aforementioned analysis is a simplification to study the imaging system resolution using elementary Fourier analysis.

The detector LSF used in calculating the imaging system LSF does not consider optical photon transport. The optical spread must be calculated for the real detector pitch by taking the optical properties of the septa material into

account to calculate the detector-only LSF. However, in order to correctly account for the *x*-ray source LSF in equation (5.5), one needs to calculate the detector LSF at a very small detector (virtual) pitch. The presampling LSF corresponds to the readings that each photodiode would have if it were placed anywhere at the bottom of the crystal surface. To find the presampling LSF we need to find the moving average of the finely sampled LSF by averaging the appropriate number of points for a given photodiode size. Therefore, in this simple approach to account for the source size, patient scatter and geometric magnification, the optical transport was ignored. The effect of optical photon transport was thus only included in the first half of this study primarily to investigate the effect of optical noise on the $DQE(0)$ and of the optical signal spread on the $MTF(f)$ of the detector alone.

C. Material and Methods

All the MV intractions were simulated using the code DOSXYZnrc of the EGSnrc (Kawrakow and Rogers, 2002) Monte Carlo simulation system. The *ECUT* and *PCUT* parameters, which are the cut off energies for electron and photon transport, were set to 0.521 MeV (rest mass + kinetic energy) and 0.01 MeV, respectively. PRESTA II algorithm was used for electron transport.

A detailed description of how DETECT2000 (Levin and Moisan, 1996; Knoll *et al.*, 1988) was used to simulate the optical photon properties of an early prototype of 8-element $CdWO_4$ crystals in contact with photodiodes, is described elsewhere (Monajemi *et al.*, 2004). The optical photon properties of the cone beam detector in this study are assumed to be the same as the early prototypes; therefore, similar simulation methods are employed here.

Briefly, in DETECT2000 (Levin and Moisan, 1996; Knoll *et al.*, 1988) a number of optical photons proportional to the energy deposited in each user defined voxel is created isotropically. The optical photons are individually tracked until they are either absorbed in the crystal bulk or septa material, or reach the photodiodes or escape the volume. Optical scattering and absorption occur in the crystal volume based on the corresponding wavelength-dependent,

user-specified mean free paths. The software offers seven different surface finishes for the septa material: METAL, PAINT, POLISH, GROUND, DETECT, PSEUDO and UNIFIED. Each of these surface finishes treats the reflection and transmission of light in a different way. A PSEUDO surface is just a boundary which connects two different components having the same optical properties and is ignored by the program. Table 5.1 provides further details about the properties of these surfaces.

Table 5.1: **Properties of the surface finishes used in DETECT2000 (Levin and Moisan, 1996, Knoll *et al.*, 1988)**

Surface Finish	Properties
METAL	This is a smooth surface with a metallic coating. Optical photons are either absorbed or reflected. The reflection coefficient gives the probability of **specular** reflection.
PAINT	This surface is painted with a diffused coating material. Optical photons are either absorbed or reflected. The reflection coefficient gives the probability of **Lambertian** reflection.
POLISH	The normal for each local micro-facet in the surface is parallel to the average surface normal. Optical photons, assumed to have random polarization, are first tested for **specular** reflection with the probability given by Fresnel reflection, R. Transmission is considered with probability of (1-R). If the surface is in contact with vacuum (no other component specified), an external diffuse coating material with a reflection coefficient can be specified to get some of the lost photons back in the medium via **Lambertian** reflection.
GROUND	This is an optically ground or roughened surface. It is treated in exactly the same manner as a POLISH surface. The only difference is that the local micro-facet normal follows a **Lambertian** distribution compared to the average surface normal and the reflection is **Lambertian.**
UNIFIED	This surface is similar to the GROUND surface with a few main differences. Firstly, the angle between the local micro-facets and the average surface normal follows a Gaussian distribution of zero-mean and a user defined standard deviation (SA). Secondly, the refraction index of coating material is used as the Fresnel reflection coefficient. The transmission into coating material follows Snell's law. The transmitted photons may be reflected back into the medium if the reflection coefficient of coating material is specified. If the transmission does not occur in the first place, one of the four types of reflection can occur: specular with respect to local normal, specular with respect to average surface normal, Lambertian and backward.
DETECT	This is the detecting surface. A user-defined, wavelength-dependent quantum efficiency can be specified.

i. Imaging Characteristics of the Detector

a. Septa Material

1. Spatial Resolution

To study the pre-sampling $LSF(x)$ and $MTF(f)$ of the segmented detector, the slanted slit technique (Fujita *et al.*, 1992) as shown in figure 3.7, was used. A narrow slit (10^{-6} cm) beam containing $5x10^6$ *x*-ray photons, and sampled from the 6 MV spectrum shown in figure 5.2, was incident on the x-y surface of the 2D segmented detector at an angle of 1.9° with respect to the y-axis (figure 5.3) and the 2D distribution of the mean deposited energy was calculated using DOSXYZnrc. The 6 MV photon beam spectrum is the same as that is used in our treatment planning system (TMS-Helax, Nucletron). The detector consists of 60 x 60 voxels corresponding to an area of 60 x 60 mm^2. The x and y dimensions of each voxel include 0.85 x 0.85 mm^2 of $CdWO_4$ surrounded on all four sides by 0.075 mm of septa resulting in a fill factor of 72% $(=(0.85mm \times 0.85mm) \div (1mm \times 1mm))$. The detector pitch and the fill factor are based on the dimensions of a commercially available 2D photodiode array (SCA-CA256ES, Semicoa, Costa Mesa, CA) that can be tiled in 2D along a spherical surface to form a focused area detector. Moreover, due to the cleavage plane in $CdWO_4$, it cannot be manufactured with a pitch < 1 mm in 2D (Kinloch *et al.*, 1994). Only the central 30 x 30 voxels were used to analyze the LSF_{pre} and MTF_{pre} of the detector. Crystal heights (H) of 10, 20 and 30 mm were simulated; in each case the crystal was divided into 1 mm thick voxels along the height (z) direction. For each crystal height, two sets of simulations were carried out. In the first set of simulations, tungsten septum was chosen for its high density of 19.3 g/cm^3. In the second set of simulations, polystyrene septum was chosen for its low density of 1.05 g/cm^3. For each case the MV only LSF_{pre} and MTF_{pre} were obtained by summing the energy deposition along the z direction and applying the slanted slit technique (Fujita *et al.*, 1992) to the resulting 2D energy distribution.

In order to include the optical photon transport, the geometry of the $CdWO_4$ cone beam detector as simulated in DETECT2000 is shown in figure 5.3. Figure 5.3 does not explicitly show the virtual voxel boundaries in the z-direction. The division of crystal height into virtual voxels in the z-direction, as mentioned above, was made to study the effect of the depth-dependent fraction of detected optical photons. The segmented crystal array is attached to the photodiode array of the same pitch and fill factor through a sheet of optical glue. The glue has size of 60 mm x 60 mm x 0.075 mm (thickness) with a refractive index of 1.47 (Dow Corning glue, Montecchi and Ingram, 2001). In simulating a cone beam detector in DETECT2000, we assumed very similar optical characteristics to the earlier prototype array of an 8-element detector. The emission spectrum of optical photons for $CdWO_4$ was taken from Kinloch at al. (1994)(see figure 2.7). Optical photon transport in DETECT2000 (Levin and Moisan, 1996; Knoll *et al.*, 1988) considers self-absorption (see figure 2.8) and scattering within crystal bulk, reflection and absorption in septa material, refraction and total-internal reflection at crystal-glue-photodiode interfaces, and the spectral sensitivity of the photodiode array. The refraction indices for $CdWO_4$ (2.1-2.2; Kinloch *et al.*, 1994), and the photodiode (1.54 for epoxy glass window ; Hamamtsu photodiode specification sheets) were taken from the references. Similarly, the sensitivity spectrum (figure 2.10) of a typical silicon photodiode with epoxy glass window was taken from the Hamamatsu photodiode specification sheets. The optical mean free path of $CdWO_4$ varies with wavelength with a value of 238 mm at 450 nm (Kinloch et al., 1994). The surface types of the scintillation crystals, optical glue and photodiode elements are similar to our previous study since a good agreement between measured and modeled signals was obtained using these surface types. The -z face of each crystal (bottom) is a GROUND surface where it is in contact with the optical glue. All the other surfaces of the crystal are simulated as GROUND with a reflection coefficient (RC) of 0.975 for polystyrene, and 0.65 and 0.8 in the two simulations for tungsten. The values for the RC were estimated from *Saint-Globain Ceramics & Plastics* scintillation crystal array and assembly specification data. The optical reflectance of polystyrene was treated

similarly to the Teflon sheet. The RC value of bare tungsten foil was taken as 0.65, a typical value for a metal surface. A value of 0.8 was chosen for the simulations, however, as that would be more typical of polished metal septa plates (Krus *et al.*, 1999). All the surfaces of the optical glue except for the top and bottom are METAL surfaces with RC = 1.0. The +z surface of the photodiode (top) which is in contact with the optical glue is a POLISH surface and the remaining faces are DETECT surfaces with the spectral sensitivity of the photodiode array specified. Since the spectral sensitivity of the photodiode was included in the optical simulation, the output of DETECT2000 corresponds to the relative photodiode current.

Since only mean relative photodiode current is required for the $MTF(f)$ calculations, an arbitrary total of 15 x10^6 optical photons were generated in the detector for each septa, height and RC configuration; the location and number of optical photons generated in each x, y and z voxel was determined by the fraction of the MV energy deposited in that voxel. The relative current produced in the photodiodes, as determined in the optical simulation, was recorded and the complete LSF_{pre} and MTF_{pre} were calculated using the slanted slit method (figure 3.8) for each configuration using the central 30 x 30 voxels.

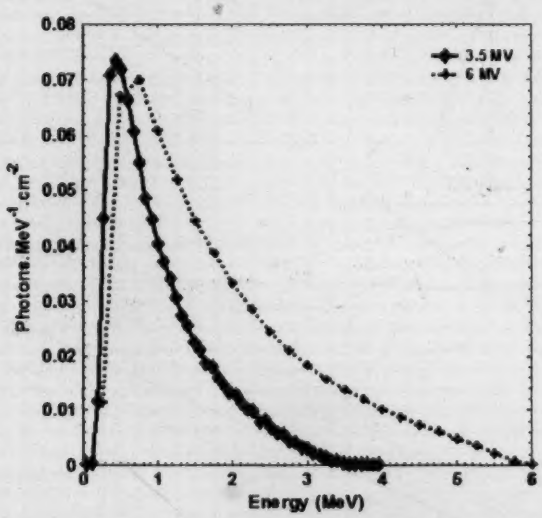

Figure 5.2: The 6 MV and 3.5 MV spectra used in this study.

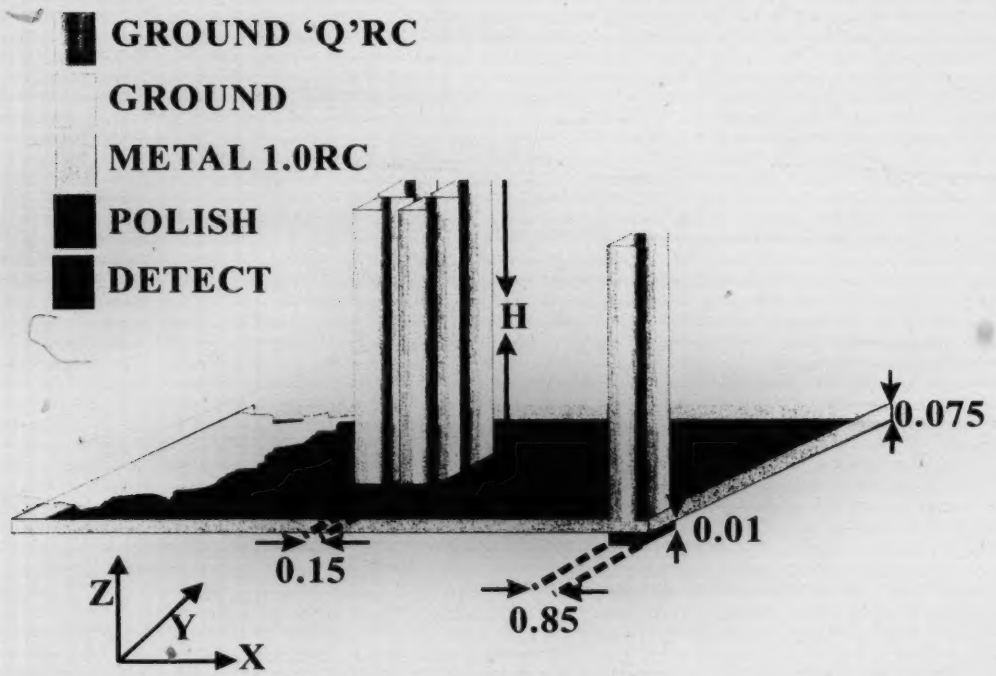

Figure 5.3: The detector geometry for studying the complete *MTF(f)*, *NPS(f)* and *DQE(f)* of the detector for a pitch of 1 mm, varying height in studying the effect of crystal height and septa: The size of each crystal is 0.85 mm x 0.85 mm x K mm. Each crystal is surrounded by 0.075 mm thick septa material on four sides. Only the crystals and septa material are modeled for the x ray energy deposition simulation study while the entire detector (crystals + septa material + optical glue + photodiodes) is simulated to study the optical photon transport properties. In DETECT2000, crystal surfaces except for the -z surface are GROUND (shaded) with 'Q'RC (Q = 0.975 for polystyrene and 0.65 and 0.8 for W in two separate sets of simulations). The -z surface of the crystals as well as the +z surface of the optical glue (white) are GROUND without a reflective coating. The optical glue is a sheet of size 30 mm x 30 mm x 0.075 mm. The -z surface of the optical glue which is in contact with the photodiodes (dark grey) as well as the +z surface of the photodiodes is a POLISH surface. All the other surfaces of the optical glue are METAL (light grey) 1.0RC surface; while all the other surfaces of the photodiodes are DETECT surfaces (black) with the spectral sensitivity of the photodiodes specified. Each crystal is in contact with one photodiode so that each photodiode covers the -z surface of its corresponding crystal entirely.

2. *DQE(0)*

To find the AEDs for each crystal height and septa configuration, a 1 mm x 1 mm beam of 10,000 *x*-ray photons sampled from the 6 MV spectrum in figure 5.2 was incident on the central voxel in a 30 x 30 element array of $CdWO_4$ with the same geometry as shown in figure 5.3. Since detector elements are assumed to be identical, only a 1 x 1 mm^2 beam was simulated. The DOSXYZnrc code was modified slightly to give the energy deposited from each MV photon (i) in the scintillation fraction of each voxel (n, m, k). These functions, $e_i(n,m,k)$, were summed along the x, y and z direction for each photon, and scored in 0.01 MeV bins. The moments of the resulting AED were used to find the MV only $DQE(0)$ for each configuration.

For each MV photon, the functions $e_i(n,m,k)$ were multiplied by the optical yield of $CdWO_4$ (20,000 photons/ MeV; Kinloch *et al.*, 1994) to give the number of optical photons created in each voxel for each MV photon, $S_i(n,m,k)$. Using an average number for creation of optical quanta per MeV energy deposited implies that the noise in creation of optical photons has been ignored in this study. Since the number of optical photons created in each voxel is at least 10 times larger than the number of optical photons detected (Monajemi *et al.*, 2004), this assumption should have a minimal effect on the calculated $DQE(0)$.The optical photons created in each voxel were then followed using DETECT2000 and the optical properties mentioned above, and their fate was recorded. Only the optical photons that were detected in each photodiode element were tallied to calculate the relative photodiode current S_{opt} per each incident *x*-ray photon. $P(S_{opt})$ and the resulting $DQE(0)$ were calculated for each configuration.

The $DQE(0)$ simulations for the septa material W (RC = 0.65) and all three different heights were repeated five times, each time with different random number seeds in both DOSXYZnrc and DETECT2000, to get sample error bars for the simulations. In addition, the effect of the number of incoming *x*-ray photons on $DQE(0)$ was investigated by changing this input from 10,000 to

1,000,000. It was found that the variation in MV-only $DQE(0)$ is less than 1% for an increase of 100 fold in the input number of *x*-ray photons.

The presence of septa material affects the $DQE(0)$ that is inherent to the combination of a certain scintillator material and beam spectrum in two ways. Firstly, a fill factor of less than unity decreases $DQE(0)$. Secondly depending on the septa material, this decrease in $DQE(0)$ may or may not be compensated for or even surpassed due to the secondary electrons generated within the septa material. As part of investigating the effect of septa material on our hypothetical detector, we also found the MV only $DQE(0)$ for a 30 x 30 x H mm^3 crystal of $CdWO_4$ and fill factors of 100% and 72% where the septa material is air.

b. Beam Spectrum

The purpose of this part of the work was to assess if the combination of silicon photodiode arrays and $CdWO_4$ crystals forms a useful detector for MVCT imaging for the fan-beam geometry of the Hi-Art II TomoTherapy™ machine. This motivation comes from the fact that the discrete photodiodes can be mechanically mounted on an arc to form a focussed multi-slice MVCT detector. The 3.5 MV photon spectrum used to study the effect of beam spectrum on the imaging performance of the detector is also shown in figure 5.2. The 3.5 MV photon spectrum was chosen since it is that of the MVCT imaging beam of a Hi-Art II TomoTherapy™ machine. This spectrum was obtained by an in-house simulation of the treatment head of this machine in BEAMnrc (Rogers *et al.*, 1995). The geometry of the various components of the imaging detector is the same as shown in figure 5.3. All the simulation parameters of MV *x*-ray and optical photon transport were also the same as the simulations carried out to study the effect of septa material. Only the 20 mm thick $CdWO_4$ crystal with polystyrene septa (RC = 0.975) was simulated to study the *x*-ray energy spectrum effects on the $MTF(f)$ and $DQE(0)$.

c. Divergence

Thick, segmented scintillation crystals are primarily used to improve the DQE of imaging detectors; however, beam divergence can degrade the detector MTF at off-axis locations. The angle of beam divergence at the corners of a 40 x 40 cm^2 field in a teletherapy unit of 100 cm source to axis distance can be as large as 15.5°. Other investigators (Sawant *et al.*, 2005; Pang and Rowlands, 2002) have anticipated the degradation of detector MTF due to beam divergence and suggested that the detector elements should be focused on the source to reduce this effect. In this section, the effect of beam divergence on the imaging characteristics of the detector was studied. The complete simulations taking both the *x*-ray and optical photon transport into account were performed for 10 mm and 30 mm thick $CdWO_4$ crystals with polystyrene septa (RC = 0.975) by tilting the incident slanted slit beam described in section C.i.a.1. from the normal incidence in the -z direction (figure 5.3) by 5°, 10° and 15° to study the LSF_{pre} and MTF_{pre} of the detector.

ii. $MTF(f)$: Entire System

The effects of detector pitch, system magnification, source size and patient scatter were studied on the entire imaging system resolution. This section is not meant to be a comprehensive study of these effects, but rather an attempt to approximate the magnitude of the effects on the resolution of this system. Therefore, two general simplifications are made. First, the effect of optical photons is ignored; this implies that we are assuming a detector with ideal optical photon transport properties. The most important effect of segmentation is stopping the transport of optical photons from one element to another. Since we are assuming ideal optical transport, the second simplification is that we are also assuming a non-segmented detector.

The slanted slit technique (figure 3.8) is a means of approximating the finely sampled LSF_{pre} in segmented detectors. Since we are no longer using a segmented detector in our simulations, the slanted slit method is not used to find

the LSF_{pre}. We have a pencil beam incident on the detector to find the finely sampled PSF. Integrating the PSF in the y dimension gives the finely sampled LSF as indicated in equation 3.16. Using the moving average of an appropriate number of points from this finely sampled LSF gives an estimate of the presampling LSF.

a. Detector Pitch

The LSF of a typical linear accelerator source is represented by a Gaussian distribution with a full width at half maximum (FWHM) of 1 mm and 2 mm (Munro *et al.*, 1988). The detector is a 3 x 3 x 1 cm^3 sheet of $CdWO_4$ divided into 0.01 mm x (3 x 1 cm^2) voxels, i.e. the energy deposition function was averaged in the y and z directions and resolved in the x-direction alone. A pencil beam of 6 MV photons was incident normally on the detector at the centre. By averaging the deposited energy distribution due to a pencil beam of *x*-rays along the y-direction one calculates the 1-D detector-radiation LSF $(=q(x)$ in step (c) in figure 3.6) along the x-axis. However, the source function needs to be incorporated as per equation 5.5 to estimate a system MTF. Both the source and detector-radiation LSFs were scaled to the object plane with system magnification of 1.4 and then convolved to obtain the system LSF which was Fourier transformed to obtain the system *MTF*. The effect of pixel pitch on the system presampling LSF was calculated at 0.5, 0.7 and 1.0 mm in the x-direction by using the moving average of an appropriate number of 0.01 mm pixels to create larger pixels, (pitch = variable, fill factor = 100%, M=1.4).

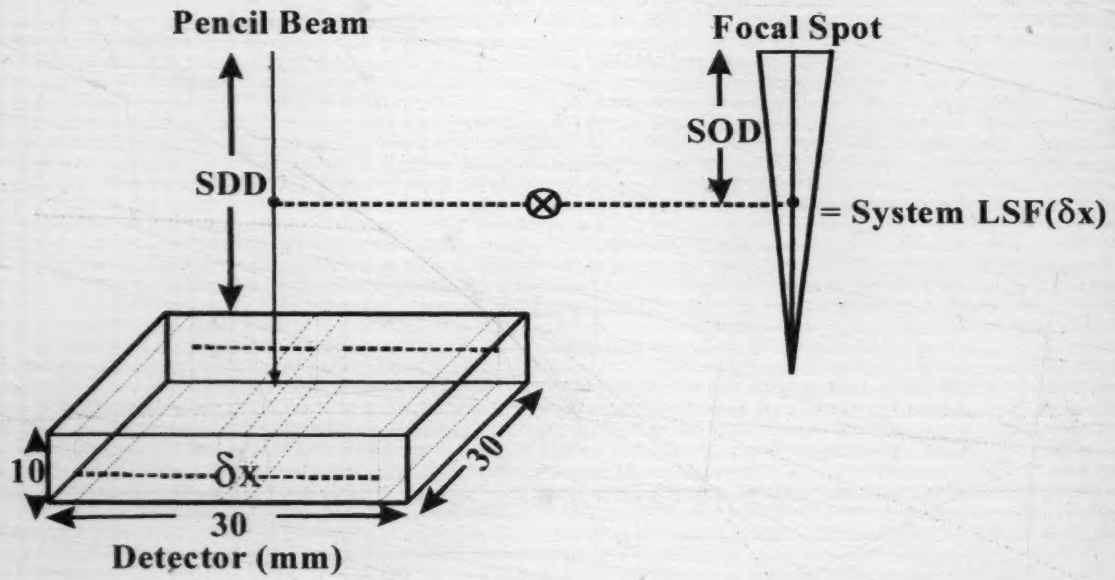

Figure 5.4: The system *LSF* is calculated as a function of detector pitch (δx). The system *LSF* is the convolution of the detector *LSF* and source *LSF* (both scaled to the object plane). The detector *LSF* is first calculated by Monte Carlo simulation of energy deposition in the $CdWO_4$ scintillation crystal for a 6 MV pencil beam using a very small detector pitch (0.01 mm) in x-direction and averaging along y-direction. The focal spot *LSF* is assumed to be a Gaussian function with FWHM of 1 and 2 mm. The system *LSF* calculated for δx = 0.01 mm was converted to larger detector pitches of 0.5, 0.7 and 1.0 mm by using the moving average of an appropriate number of points.

c. Magnification

The effect of changing the magnification of the system on the system $MTF(f)$ was found by keeping SOD constant in figure 5.4 and changing the SDD. The $MTF(f)$ of the system was the Fourier transform of LSF obtained from equation 5.5, for a detector pitch of 1 mm, and magnification values of 1.0, 1.2, 1.4 and 1.6. (pitch = 1 mm, fill factor = 100%, M = variable) The simulations were carried out for two different source sizes (FWHM = 1 and 2 mm).

d. Object Scatter

The effect of scatter from the object on the system $MTF(f)$ was found at two magnification values of 1.2 and 1.4 (figure 5.5). A slab object was simulated by placing solid water blocks of thickness 20 and 40 cm such that the center of the slab along the beam direction was 100 cm away from the source. For the case of water slab thickness of 40 cm and magnification value of 1.2, the simulations were repeated again by placing a 1 mm thick sheet of Cu with the same area as the detector on top of the sheet of $CdWO_4$. The $MTF(f)$ of the system was again determined by Fourier transform of LSF obtained from equation 5.5, (pitch = 1 mm, fill factor= 100%, M= 1.2 and 1.4) It should be noted that the incident beam on the detector in this case contains the primary and laterally scattered photons. Therefore, the calculated detector LSF incorporates the patient scatter subject to the assumption that the laterally scattered photon distribution from the object is a spatially-invariant function.

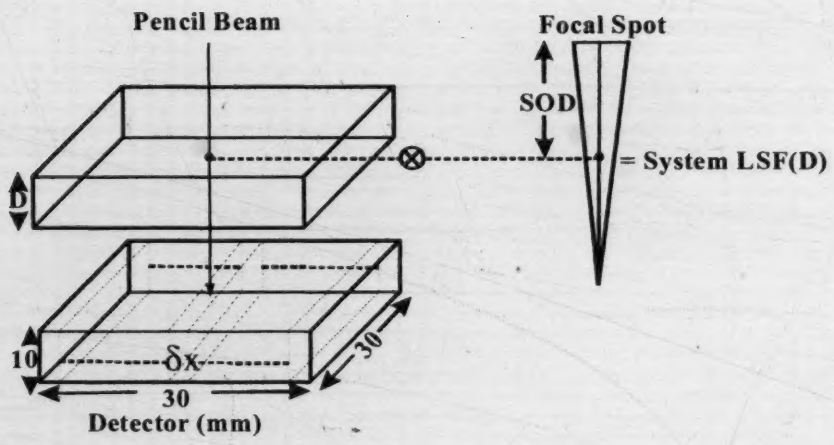

Figure 5.5: The LSF_{sys} is calculated as a function of patient thickness, D. The LSF_{sys} is the convolution of the detector *LSF* and the source *LSF* (both scaled to the object plane). The detector *LSF* is first calculated by Monte Carlo simulation of energy deposition in the $CdWO_4$ scintillation crystal for a 6 MV pencil beam using a very small detector pitch (0.01 mm). The *source LSF* is assumed to be an Gaussian function with a FWHM of 2 mm. D=20 and 40 cm. The system *LSF* calculated for δx = 0.01 mm was then re-sampled to a larger detector pitch of 1.0 mm.

D. Results

i. Imaging Characteristics of the Detector

A. Septa Material

1.Spatial Resolution

Figure 5.6 shows the *LSF* of 10 and 30 mm tall crystals with septa materials of W (RC = 0.80) and polystyrene (RC = 0.975). The results obtained with W; RC = 0.65 are similar to W; RC = 0.80 and are not shown here. The peaks and valleys observed in these *LSF s* have been reported earlier by Sawant *et al.* for CsI(Tl) crystals (2005) without including the effect of optical photons. The reason for the existence of these features as pointed out by the authors is

that the slanted slit method approximates the process of scanning a slit beam across the detector and recording the signal at the central detector element for each position of the slit beam. Where the slit beam is completely incident on the septa walls, the signal recorded in the scintillator element is due to secondary *x*-ray photons and electrons originating in the septa walls. Therefore $LSF\,s$ have downwards jumps when using polystyrene septa and upwards jumps when using tungsten septa since the latter produces a larger fluence of secondary photons and electrons due to its higher atomic number and density compared with $CdWO_4$. In addition, these features are present only very weakly for 30 mm tall $CdWO_4$ crystals in case of tungsten septa because at 30 mm the fraction of energy deposited in the crystal when the beam is incident on the crystal is not lower than the fraction of energy deposited in the crystal when the beam is incident on the septa material. However the valleys are only slightly lower for polystyrene septa when using 30 mm tall compared with 10 mm tall crystals.

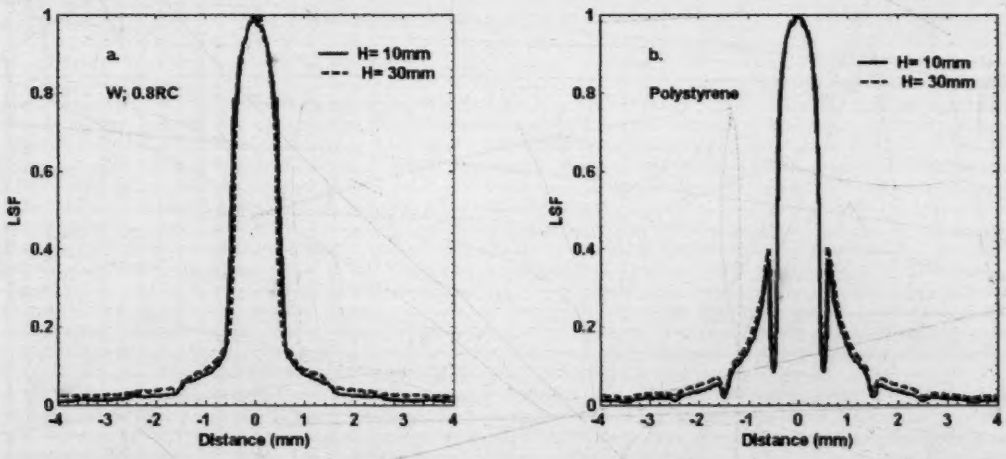

Figure 5.6: LSF of the detector as obtained by the results for energy deposition in DOSXYZnrc with W and polystyrene as the septa material.

Figure 5.7 shows the detector pre-sampling $MTF(f)$ for the three different $CdWO_4$ heights. For each crystal height, the detector $MTF(f)$ with (polystyrene septa with RC = 0.975, tungsten (W) septa with RC = 0.65 and 0.8) and without (MV only) including the optical photon transport is shown. The "MV only" case

uses polystyrene and tungsten septa but considers ideal optical photon transport. The MV case shows that the $MTF(f)$ for tungsten septa is always higher than $MTF(f)$ when polystyrene is used as septa material. For each crystal height (H) when the effect of optical photons is included for the polystyrene septa, the detector $MTF(f)$ is lower than the "MV only" case. At 0.5 cycles/mm this decrease is approximately 9% for polystyrene septa for each crystal height. For polystyrene septa, the relative reduction of $MTF(f)$ compared to the "MV only" case thus appears to be relatively independent of crystal height except in the lower frequency range. The optical photons that are created in the top layers (closer to the beam) will undergo more and more surface reflections as the crystal height is increased; however, these photons do not travel to the neighbouring elements since the septa are simulated as opaque by the "GROUND" surface type. The number of surface reflections increases with crystal height only if the reflection coefficient is very high, or else there is a higher probability of surface absorption. Moreover, due to the reflection being Lambertian, the angular distribution of the reflected optical photons is fairly random and less dependent on crystal height. Thus the nearly crystal-height independent additional (optical) signal spread occurs largely within the optical glue layer that is attached to the bottom of the crystals.

In the case of lower reflection coefficient for the tungsten septa, a larger fraction of the optical photons is absorbed in the septa since the probability of reflection is lower. Therefore, a larger fraction of optical photons exiting the scintillation elements are forward scattered and are unlikely to travel to neighbouring photodiode elements through the thin optical glue sheet. However, as the coating becomes less and less reflective (RC = 0.65 for tungsten), the signal in the central crystal decreases since more of the optical photons in the top layers of the crystal get absorbed due to the even lower probability of reflection. Therefore, while the spread of optical photons to the neighbouring crystals is decreased because even more of the optical photons are forward directed, the signal in the central crystal is also decreased. Thus, the $MTF(f)$ is

not improved any further. This is the reason that the $MTF(f)$ for W 0.65 RC and 0.8 RC are almost the same for all heights.

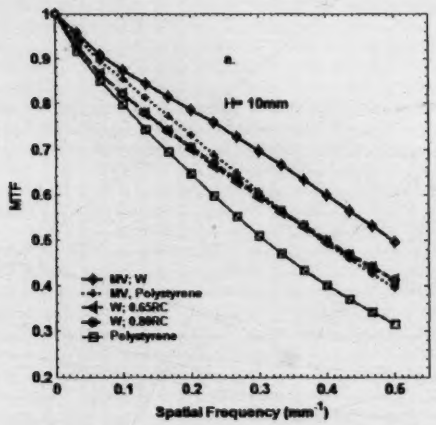

Figure 5.7: The presampling MTF(f) of the detector for different septa wall material, reflection coefficient and height configurations.

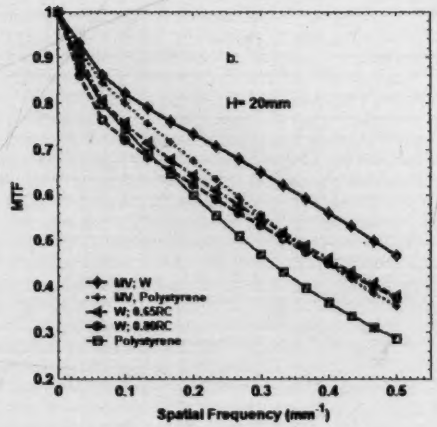

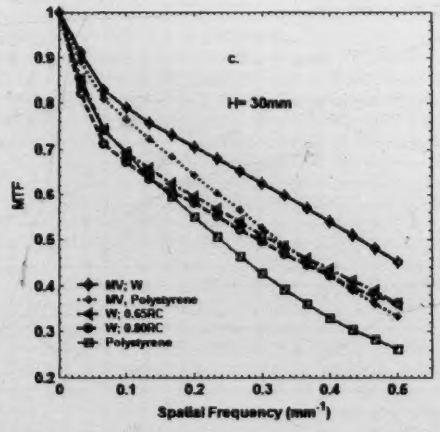

2. *DQE(0)*

Figure 5.8 shows the effect of introducing a fill factor of 72% on the inherent $DQE(0)$ that is possible by using $CdWO_4$ scintillators in a 6 MV beam. The reduction in $DQE(0)$ is approximately 6, 9 and 13% for 10, 20 and 30 mm tall crystals with 72% fill factor and air-septa. It should be noted that the $DQE(0)$ keeps on increasing with increased crystal thickness in both cases since an ideal optical photon transport is assumed in all cases for this figure.

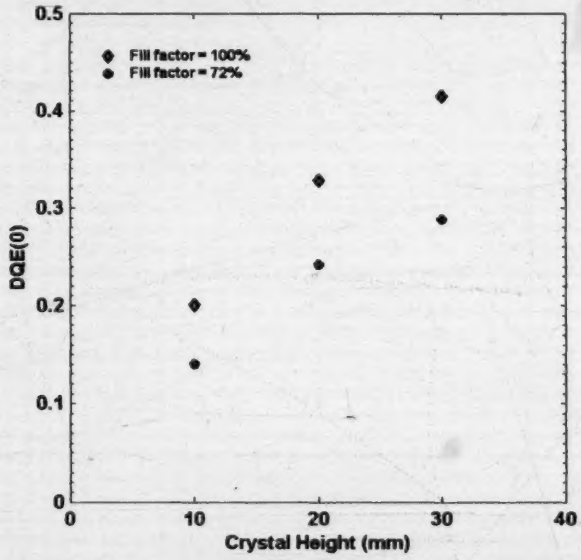

Figure 5.8: The DQE(0) for two different fill factors. The effect of optical photons are ignored. The septa material for fill factor of 72% is assumed to be air.

Figure 5.9 shows the combined effects of crystal height and septa material on the $DQE(0)$ of the detector. The error bars obtained by repeating the $DQE(0)$ calculation for W septa with RC = 0.65 are also shown. As expected, the $DQE(0)$ for the "MV only" case increases as the crystal height is increased. The $DQE(0)$ for the MV case is always higher for W as the septa compared with polystyrene. As the effect of optical photon transport is taken into account, the $DQE(0)$ reduces for each septa and crystal height compared to the "MV only" case. For

polystyrene septa (RC = 0.975) compared to "MV only" case, the reduction in $DQE(0)$ is relatively small (about 5% for 30 mm tall crystals) and there is an overall gain in $DQE(0)$ as the crystal height is increased. For the "W, 0.8 RC" compared to the "MV only" case, the reduction in *DQE(0)* becomes significant; there is only a 2% increase in *DQE(0)* from 10 mm to 20 mm and a 1% decrease from 20 mm to 30 mm. For the "W, 0.65RC" case compared to the "MV only", there appears to be no net gain in $DQE(0)$ as the crystal height is increased; the $DQE(0)$ is the smallest for the 30 mm crystal height. We observe that for a crystal height of 10 mm, the best $DQE(0)$ is obtained with *W* as the septa material even with RC value as low as 0.65. However, for crystal heights of 20 and 30 mm, the best $DQE(0)$ is obtained with polystyrene as the septa material.

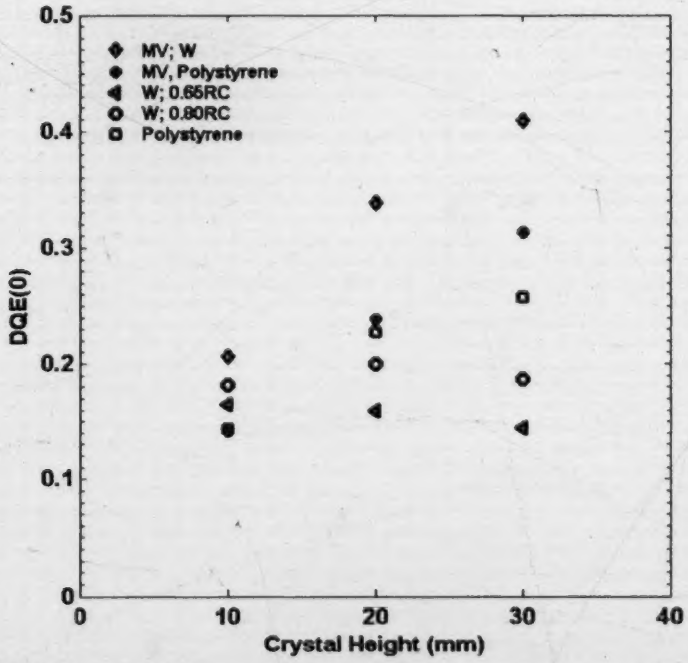

Figure 5.9: The DQE(0) of the detector for different septa wall material, reflection coefficient and height configurations.

b. Beam Spectrum

The comparison between a 6 MV beam with a flattening filter as used in a conventional medical linear accelerator and a 3.5 MV beam without a flattening filter ("Tomo" beam) as used in the TomoTherapy™ (HiArt II, Tomotherapy Inc., Madison, WI) on the $MTF(f)$ (crystal height = 20 mm; polystyrene septa with RC = 0.975) is shown in Figure 5.10. As expected the increase in lower energy photons in the "Tomo" beam improves the spatial resolution. The $MTF(f)$ improves since the *x*-ray photons are less energetic and hence the resulting charged particles are more likely to deposit their energy locally. The $DQE(0)$ improvement from 23% to 32% is possible by using the tomotherapy beam instead of the 6 MV beam for a 20 mm tall crystal with highly reflective septa (RC = 0.975).

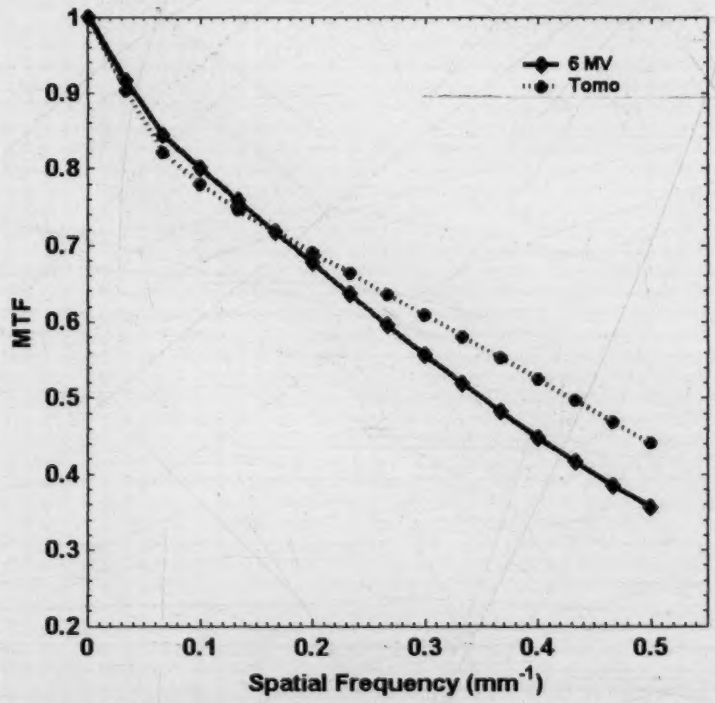

Figure 5.10: The *MTF(f)* of 20 mm tall crystal with polystyrene septa in both 6 MV and 3.5 MV beams shown in Figure 5.2.

c. Divergence

Figure 5.11 shows the effect of beam divergence on the detector LSF. The septa material for all the simulations in this section is polystyrene (RC= 0.975). Figures 5.11(a) and (b) show this effect on the LSF for 10 and 30 mm tall crystals when the effect of optical photon transport is not considered. As expected, when the angle of beam incidence increases the primary photons are able to travel to more segments in the detector, and thus the LSF becomes wider. Figures 5.11(c) and 5.11(d) show the effect of beam divergence on the LSF including the spread of optical photons. The interesting result here is that as the effect of optical photons is included, the shape of the LSF changes. This is most obvious in the 30 mm tall crystal. Near the slit beam entrance into the detector, the *x*-ray photons deposit energy in the top layer of the crystal. As the pencil diverges into the neighbouring segments, the energy is deposited in the relatively lower layers of the crystal. This makes the *LSF* in Figure 5.11(b) wider (see 15° case) with a slow decrease in magnitude away from the pencil beam entrance. The optical gain for the photons created in the top layers of the crystals is smaller than for those in the bottom layers. Thus the corresponding LSF in Figure 5.11(d) is wider but the magnitude slowly increases away from the pencil beam entrance. Therefore the shape of the LSF is reversed compared to the corresponding MV-only result.

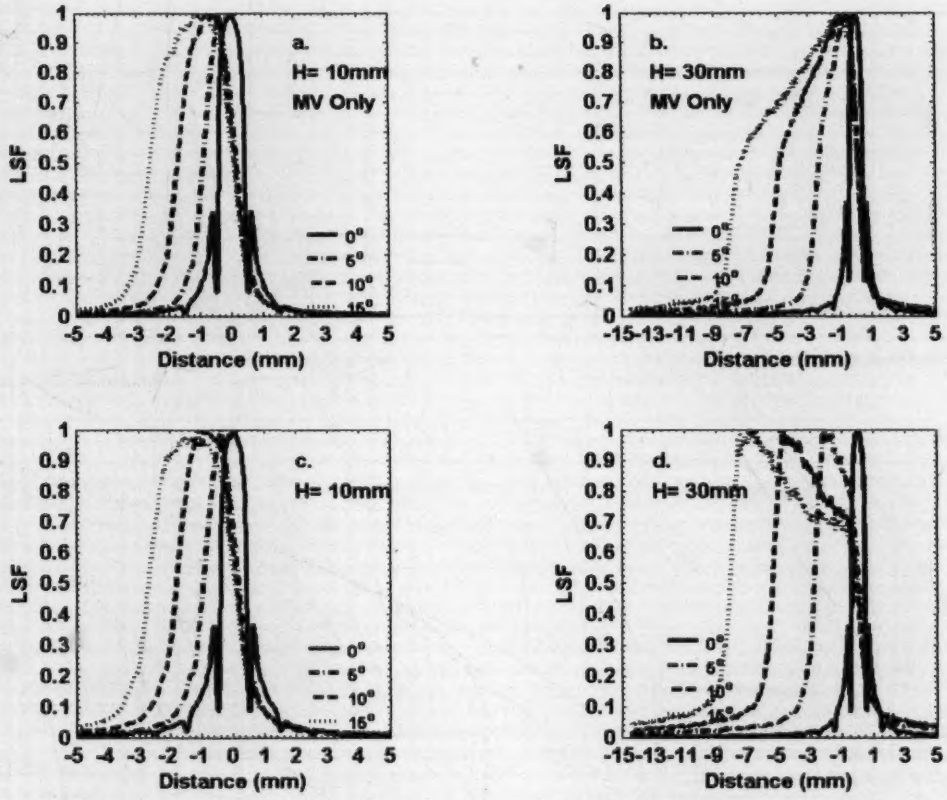

Figure 5.11: The effect of beam divergence on the *LSF* of the detector. In (a) and (b), an ideal optical photon transport is considered. In (c) and (d) the optical photon transport is considered for different crystal heights and polystyrene septa.

Figure 5.12 shows the effect of beam divergence on the $MTF(f)$ of the detector. It is seen that even a divergence of 5° can degrade the $MTF(f)$ of a 30 mm tall crystal by as much as 30% at 0.4 cycles/mm. Due to the longer path length of photons in the detector, the effect of divergence is again more readily observed on the taller crystals. The severe effect of beam divergence is not evident on the $DQE(0)$ and is not included here. Our experience with simulating imaging characteristics of non-segmented detectors shows that the $DQE(f)$ decreases in approximately the same manner.

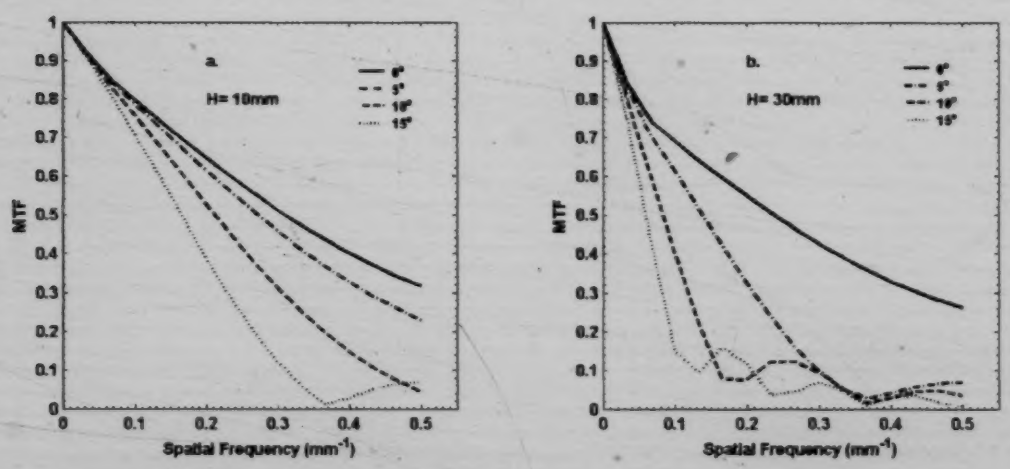

Figure 5.12: The effect of beam divergence on the presampling *MTF* of the detector. Polystyrene is the septa material.

ii. $MTF(f)$: Entire System

a. Detector Pitch

The effect of detector pitch is shown in figure 5.13. Figure 5.13 a shows the detector $MTF(f)$ alone for detector pitches of 0.01, 0.5, 0.7 and 1 mm by assuming an ideal optical photon transport. Figure 15.13(b) shows the system $MTF(f)$ resulting from the convolutions of Figure 15.13(a) and the LSF of the

source, as per equation 5.5. The system $MTF(f)$ curves for different pitch values are divided into two different sets, each set representing one source size, denoted as 'a' in this figure. As seen, including a realistic focal spot of 2 mm decreases the $MTF(f)$ by 40% at about 1.5 mm^{-1}, while this decrease is about 20% for a 1 mm source. Therefore, it is important to include the effect of focal spot un-sharpness in any study of the overall $MTF(f)$ of a system. Increasing detector pitch has a two fold degradation on the system $MTF(f)$: the Nyquist frequency is reduced and the $MTF(f)$ becomes more and more aliased. The aliasing is more pronounced for smaller focal spots. Frequencies of 1.31, 0.93, 0.65 mm^{-1} in the object plane correspond to the Nyquist frequencies of 0.5, 0.07 and 1 mm detector pitches respectively (M = 1.4).

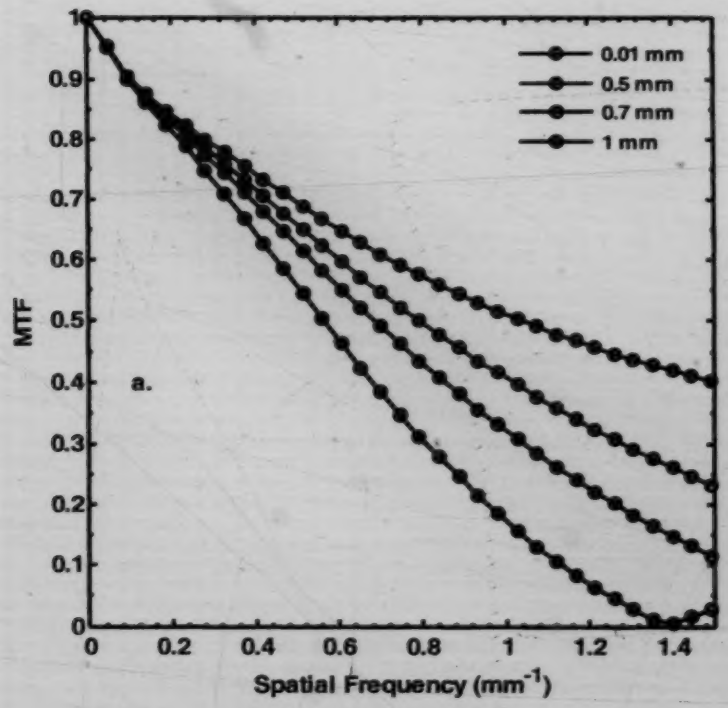

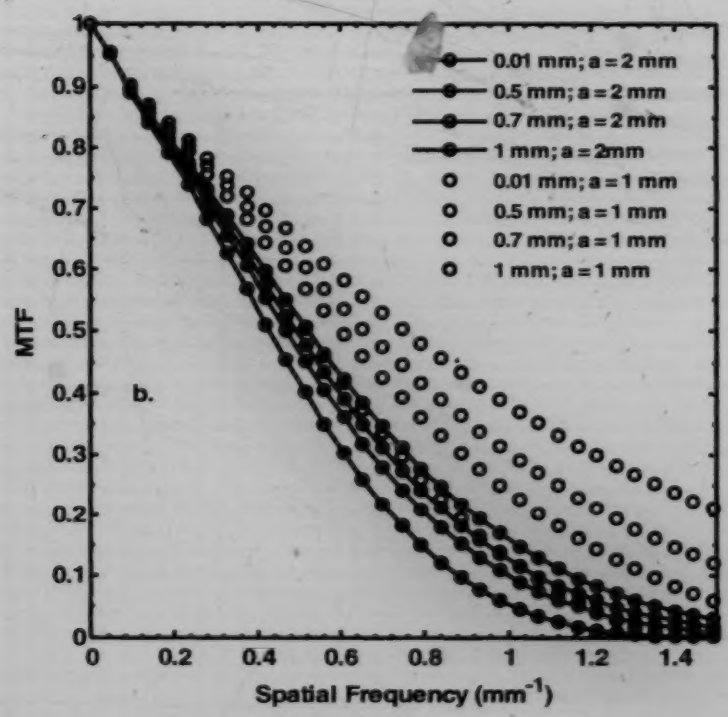

Figure 5.13: The *MTF(f)* of detector, and the overall system *MTF(f)*. *(a):* Detector *MTF(f)* in the object plane: 1 cm height; pitches = 0.01, 0.5, 0.7 and 1 mm; no optical transport. *(b)*: The system *MTF(f)* in the object plane with a magnification of 1.4 .

b. Magnification

Figure 5.14 shows the effect of magnification on the spatial resolution of the system for source sizes of 1 and 2 mm. The $MTF(f)$ s are shown in the plane of the object. As expected as M increases, the Nyquist frequency in the plane of the object increases. The higher the system magnification, the lesser is the de-magnification of the focal spot in the object plane. Thus the effect of focal spot size on the system $MTF(f)$ increases as system magnification increases, while the effect of detector blurring decreases with increasing magnification. Therefore in figure 5.14(a) where FWHM = 1 mm, there is an increase in $MTF(f)$ from M = 1.2 to M = 1.6 due to the fact that the detector blurring is decreasing with increasing M. If the focal spot is too large then the effect of the focal spot dominates the change in the system $MTF(f)$ as the system magnification increases. Therefore in figure 5.14(b) there is a decrease in $MTF(f)$ as the system magnification increases due to the blurring from the source size.

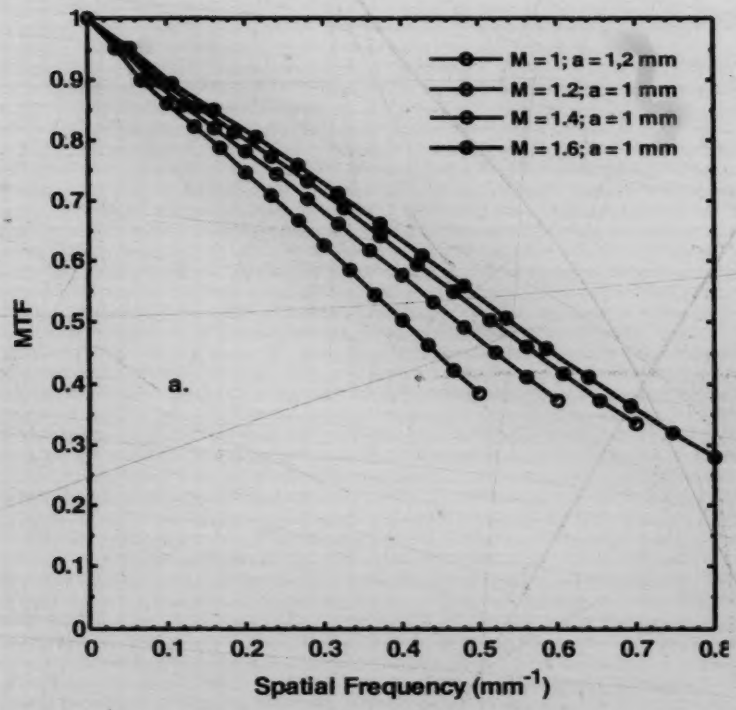

Figure 5.14: The effect of increasing the system magnification (M) on the overall system $MTF(f)$ for realistic focal spot sizes of Gaussian shape with FWHMs of 1 mm and 2 mm with ideal optical photon transport. Crystal height = 1 cm, pitch = 1 mm.

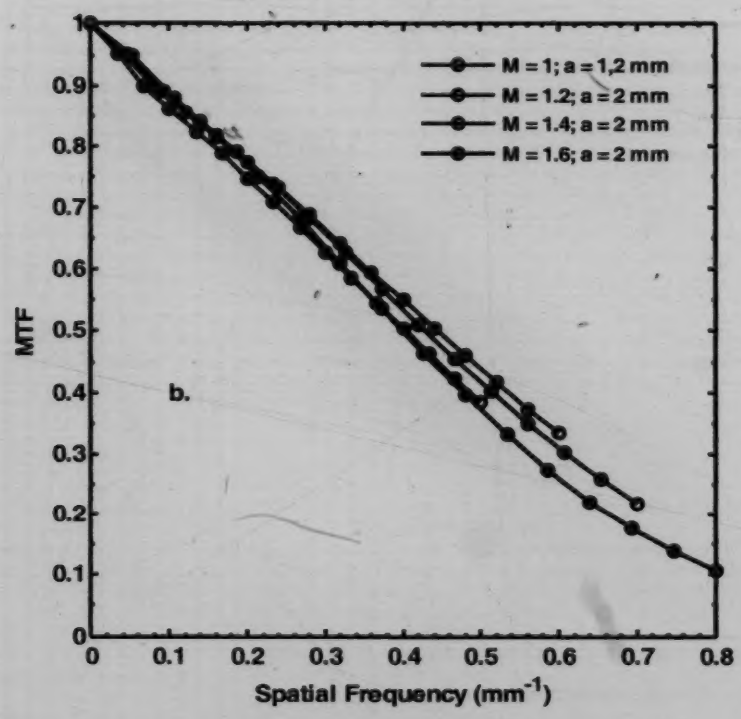

c. Object Scatter

Figure 5.15 shows the effect of object scatter on the system $MTF(f)$, for two different system magnifications of 1.2 and 1.4. It should be noted that except for the case of phantom thickness D = 20 cm, and M = 1.4, the "object scatter" might also include the charged particles that are created in the phantom and travel to the detector since no attempt was made to remove the charged particles by using a copper plate as is usually done in MV detectors (Lachaine and Fallone, 1998). At a system magnification of 1.2 and phantom thickness of 40 cm, the detector touches the exit surface of the phantom. Thus, this case shows the largest effect of the "object scatter" over the entire spatial frequency range. It is shown that employing a 1 mm thick Cu plate does not improve the system $MTF(f)$ for D = 40 cm and M = 1.2. As one decreases the phantom thickness, there is less scatter created in the thinner phantom and there exists an air-gap between the exit surface of the phantom and detector. Thus the relative effect of patient scatter, including charged particles, is reduced for an object thickness of 20 cm. In case of system magnification of 1.4, there is always an air-gap and the charged-particle fluence may become more diffused due to the scatter within the air. Thus the graphs for M = 1.4 only show the effect of photons scattered from the phantom. It should be noted that the usually employed copper plate in the MV detectors has a more important function: to create a build-up effect for very thin converter thickness. Thick-segmented scintillators may not benefit from such an effect.

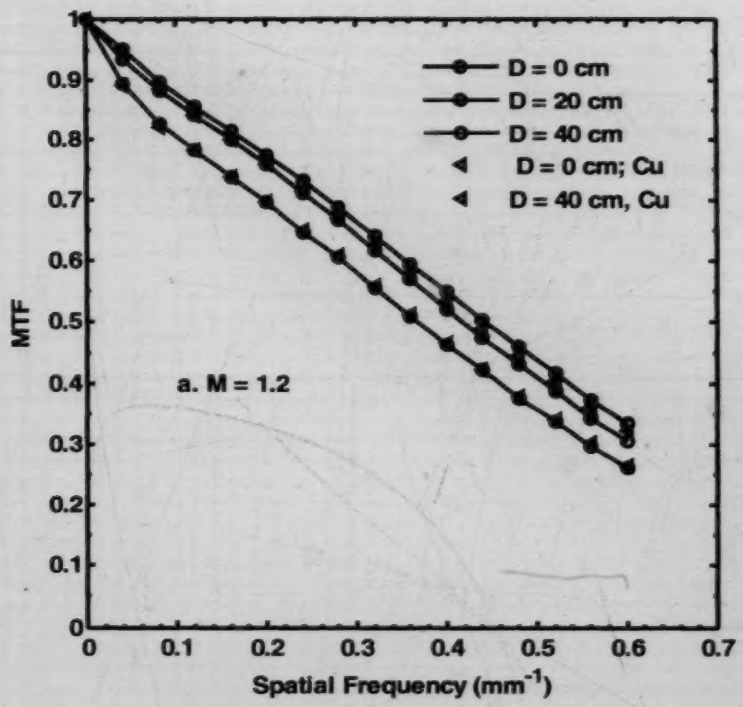

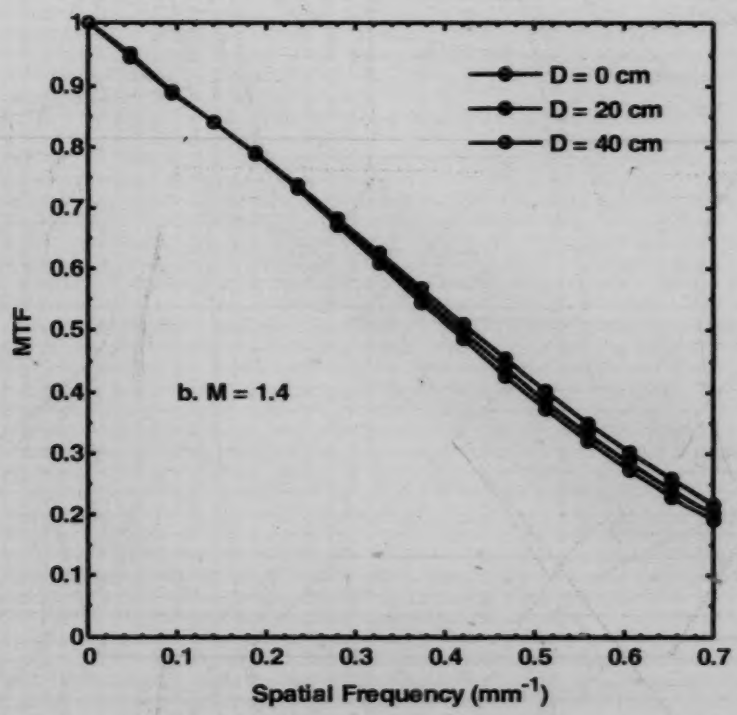

Figure 5.15: The effect of the object scatter and system magnification (M) on the overall system *MTF(f)*. D = phantom thickness and pitch = 1mm. The two extra curves in (a) were obtained using a 1 mm thick Cu plate on top of the crystal.

E. Discussion

i. Imaging characteristics of the Detector

Highly reflective and opaque septa materials are desirable to keep the optical signal loss and spread to a minimum in thick, segmented scintillation detectors. While it is always desirable to have the highest possible fill factor, i.e. the thinnest possible septa material, there is sometimes a trade off between the secondary charged particles created in the septa material and the spread of signal (both MV and optical photons) to the neighbouring crystals. At least one other group (Sawant et al., 2005) has looked into the effect of different septa materials on the imaging performance of thick segmented scintillators, namely *CsI(Tl)* and *BGO*. In their study the effect of optical photon transport was ignored. In the study presented here, the effects of using septa materials polystyrene and *W* with 0.65 *RC* and 0.8 *RC* on 10, 20 and 30 mm tall $CdWO_4$ crystals at a pitch of 1 mm and a fill factor of 72% were studied. The pre-sampling *LSF(x)*, *MTF(f)* and *DQE(0)* were determined. The "MV only" detector *MTF(f)* shows a similar decrease as a function of increasing crystal height to that noted by Sawant *et al.* (2005) between 1 and 4 cm tall CsI(Tl) and BGO scintillators. For a height of 10 mm the best *MTF(f)* is achieved when using tungsten and the worst when using polystyrene as septa materials; a similar result was obtained by Sawant *et al.*(2005) even in the absence of optical photon transport. The reduction in the *MTF(f)*, compared to the "MV only" case, after incorporating the optical transport using polystyrene septa seems to be independent of crystal height. The *MTF(f)* for tungsten septa appears to be better than for polystyrene septa even though the simulated reflection coefficient for tungsten is smaller. This is because all the septa materials considered in this study are opaque.

The *DQE(0)* keeps on increasing with the crystal height for the "MV only" case which was also demonstrated by Sawant *et al.* (2005) Compared to the "MV only" case, the *DQE(0)* decreases when optical photons are considered due to the optical Swank noise. The Swank noise factors were calculated by the ratio of

the *DQE(0)* with and without optical photon simulation for each crystal height and various types of septa (table 5.2.). In a very recent investigation, Sawant *et al.* (2006) estimated the Swank noise factor for a 40 mm tall CsI(Tl) crystal array with polymer septa as a ratio of the measured and Monte Carlo calculated *DQE(0)* to be 0.8. This value is very close to that obtained for polystyrene septa (RC = 0.975) and a 30 mm tall $CdWO_4$ crystal array.

For highly reflective septa such as polystyrene, the *DQE(0)* also keeps on improving with increasing crystal height, although the improvement between 10 mm to 20 mm is significantly larger than that between 20 mm to 30 mm. When using less reflective septa such as *W* with RC = 0.8, there is some gain in *DQE(f)* from 10 to 20 mm crystal height but none beyond 20 mm. With very poorly reflective septa such as W with RC = 0.65, there is no gain in *DQE(0)* with increasing crystal height. It should be noted that we used typical RC values (Krus *et al.*, 1999) for metal septa materials for tungsten to highlight the fact that gain in MV-only *DQE(0)* does not necessarily translate to gain in *DQE* when the effect of optical photons are considered. If one could find tungsten septa materials with very high RC value coatings , i.e. comparable to that of polystyrene, then the highest value *DQE*(0) would be obtained for tungsten septa at all crystal heights.

The *DQE(0)* calculation in the "Tomo" beam suggests that the choice of beam spectrum has a significant effect on *DQE(f)*. This result suggests that the proposed configuration would make a feasible and useful detector for MVCT imaging on the TomoTherapy™ system. For thick segmented crystals the *DQE* is high enough (e.g *DQE(0)* = 23% for $CdWO_4$ at H = 20 mm, pitch =1 mm, septa material = polystyrene with RC = 0.975 , fill factor = 72%) that the images obtained by using the 6MV beam from linacs are clinically useful. Some improvement in the *DQE(0)* can be obtained by removing the flattening filter while performing imaging using the treatment beam. Therefore, the implementation of a specialized imaging beam that does not use a flattening filter and delivers an order of magnitude less dose per pulse will greatly benefit the MVCT imaging on a conventional linear accelerator.

The severe effects of beam divergence on the imaging properties of the detector are evident. The *LSF* with divergence illustrates that objects may appear spatially shifted in the image. These effects worsen as the crystal height is increased. These results strongly suggest that area detectors used in MVCT must be focused on the source.

Table 5.2: Optical Swank noise factors as determined from Monte Carlo simulation

	$CdWO_4$ Height		
Septa Material	H = 1 cm	H = 2 cm	H = 3 cm
Polystyrene, RC = 0.975	0.99	0.92	0.81
Tungsten, RC = 0.8	0.93	0.64	0.45
Tungsten, RC = 0.65	0.85	0.52	0.36

ii. $MTF(f)$: Entire System

The graphs of detector pitch show that including a realistic focal spot of 2 mm FWHM decreases the imaging system *MTF(f)* by 40% at about 1.5 mm^{-1}. Below the spatial frequency of 0.6 mm^{-1} there are small differences among 0.5, 0.7, and 1.0 mm detector pitches. The *MTF*s for detector pitches of 0.7 and 1.0 mm appear to be slightly aliased compared to the 0.01 mm pitch, however, further degradation in the detector alone *MTF(f)* due to optical photon transport shown in figure 5.7 and in system *MTF(f)* due to object scatter shown in figure 5.15 will lessen the effect of aliasing. This simple analysis suggests a detector pitch of 0.5 mm. Unfortunately, a detector pitch of lower than 1.0 mm in 2-D cannot be fabricated using $CdWO_4$ because of the cleavage plane (Kinloch *et al.*, 1994). Based on this simplistic analysis, this may appear to be a serious limitation but it may not be so in practice. The detector pitch in diagnostic CT systems is rarely smaller than 1 mm (e.g. 1.4 mm in Brilliance Big Bore CT, Phillips Medical Systems) in the imaging plane since the majority of CT studies hinge on low contrast detectability rather than fine spatial resolution. The strength of $CdWO_4$ lies in its ability to provide significantly higher *DQE(f)* in the lower frequency range and the limitation on detector pitch may be insignificant for MVCT images used for verification imaging. One can argue that the spatial resolution in the EPID images may be poor at 1 mm pitch, although comparison

of EPID images is usually made against digitally reconstructed radiographs that are characterized by significantly poor spatial resolution than other general radiography imaging systems.

For a focal spot with FWHM of 2 mm, the size of the focal spot dominated the *MTF(f)* of the system. Therefore, as the magnification is increased, the *MTF(f)* of the system is decreased. A magnification of 1.4 appears to be good enough for decreasing the deleterious effects of scatter from a 40 cm thick patient.

F. Conclusions

i. Imaging Characteristics of the Detector

This section of the study focuses on the effects of different system parameters: the scintillation crystal height, septa material, beam spectrum, and beam divergence, on the imaging characteristics of a hypothetical area detector. It is assumed that the detector is made of tall $CdWO_4$ crystals with a pitch of 1mm and fill factor of 72%. A two step Monte Carlo simulation was employed to study the combined effects of crystal height and septa material, beam divergence and beam spectrum on the intrinsic imaging characteristics of the detector. It is concluded that when using poorly reflective septa material such as tungsten with reflection coefficients of 0.65 and 0.8, there is little advantage in increasing the crystal height more than 10 mm. However, when using highly reflective septa such as polystyrene, one can increase the detector height up to 30 mm to achieve higher *DQE(0)* values. It is also shown that employing a 3.5 MV beam without a flattening filter increases the *DQE(0)* for a 20 mm tall crystal by 9% compared to a typical 6 MV beam with a flattening filter. The severe effects of beam divergence are quantified and they strongly suggest the use of focused detectors in MV imaging.

ii. $MTF(f)$: Entire System

The system *MTF(f)*, which is defined in the object plane and considers both the intrinsic detector *MTF(f)* and the size of the focal spot, was simulated to study the effects of detector pitch, patient scatter and system magnification on the spatial resolution of the system. It is shown that the relatively large size of the focal spot in a linear accelerator (2 mm) dominates the *MTF(f)* of the system in the patient plane. A system magnification of 1.4 appears to be adequate for reducing the effect of scatter from a 40 cm thick object.

G. References

H. Fujita, D. Y. Tsai, T. Itoh, *et al.*, "A simple method for determining the modulation transfer function in digital radiography," IEEE Trans. on Medical Imaging **11**, 34-39 (1992).

D. A. Jaffray, J. J. Battista, A. Fenster, and P. Munro, " Monte Carlo studies of x ray energy absorption and quantum noise in megavoltage transmission radiography," Med. Phys. **22**, 1077-1088 (1995).

I. Kawrakow and D.W.O. Rogers, "The EGSnrc code system: Monte Carlo simulation of electron and photon transport," NRCC Report PIRS-701 (2002).

D. R. Kinloch, W. Novak, P. Raby, and I. Toepke, "New developments in cadmium tungstate", IEEE Trans. Nucl. Sci. **41**, 752-754 (1994).

G. F. Knoll, T. F. Knoll, and T. M. Henderson, "Light collection in scintillation detector composites for neutron detection," IEEE Trans. Nucl. Sci. **35**, 872-875 (1988).

D. J. Krus, W. P. Novak, L. Perna, "Precision linear and two-dimensional crystal arrays for x-ray and gamma-ray imaging applications", Proc. SPIE **3768**, 183-194 (1999).

M. Lachaîne and B. G. Fallone, "Monte Carlo detective quantum efficiency and scatter studies of a metal/a-Se portal detector," Med. Phys. **25**, 1186-1194 (1998).

J. Levin and C. Moisan, "A more physical approach to model the surface treatment of scintillation counters and its implementation into DETECT," IEEE Trans. Nucl. Sci. Symposium of Anaheim, 702-706 (1996).

T.T. Monajemi, S. Steciw, B.G. Fallone and S. Rathee., "Modeling scintillator-photodiodes as detectors for megavoltage CT," Med. Phys. **31**, 1225-1234 (2004).

T.T. Monajemi, D. Tu, S. Rathee and B.G. Fallone, "A bench-top megavoltage fan-beam CT using $CdWO_4$-photodiode detectors: II- Image performance evaluation," Med. Phys. **33**, 1090-1100 (2006).

T.T. Monajemi, "Modelling scintillator-photodiodes as detectors for megavoltage CT", MSc thesis, 2004.

M. Montecchi and Q. Ingram, "Study of some optical glues for the Compact Muon Solenoid at the large hadron collider of CERN", Nucl. Instrum. Meth. in Phys Res. A **465**, 329-345 (2001).

M. A. Mosleh-Shirazi, W. Swindell, and P. M. Evans, "Optimization of the scintillation detector in a combined 3D megavoltage CT scanner and portal imager," Med. Phys. **25**, 1880-1890 (1998).

P. Munro, J. A. Rawlinson and A. Fenster, "Therapy imaging: source sizes of radiotherapy beams" Med. Phys. **15**, 517 (1988).

S. Rathee., D. Tu, T.T. Monajemi, D. Rickey and B. G. Fallone, "A bench-top megavoltage fan-beam CT using $CdWO_4$-photodiode detectors: I- System description and detector characterization," Med. Phys. **33**, 1078-1089 (2006).

D. W. O. Rogers, B. A. Faddegon, G. X. Ding, *et al.*, "BEAM: A Monte Carlo code to simulate radiotherapy treatment units," Med. Phys. **22**, 503–524 (1995).

A. Sawant, L.E. Antonuk, Y. El-Mohri, Y. Li, Z. Su, Y. Wang, J. Yamamoto, Q. Zhao, H. Du, J. Daniel and R. Street, "Segmented phosphors: MEMS-based high quantum efficiency detectors for megavoltage x-ray imaging," Med. Phys. **32**, 553-565 (2005).

A. Sawant, L.E. Antonuk, Y. El-Mohri, Q. Zhao, Y Li, Z. Su, Y. Wang, J. Yamamoto, H. Du, I. Cunningham, M. Klugerman and K. Shah , "Segmented crystalline scintillators: An initial investigation of high quantum efficiency detectors for megavoltage x-ray imaging.," Med Phys. **32**, 3067-3083 (2005).

A. Sawant, L. E. Antonuk, Y. El-Mohri, Q. Zhao, Y. Wang and L. Perna, "Segmented crystalline scintillators: Empirical and theoretical investigation of a high quantum efficiency EPID based on initial engineering prototype CsI(Tl) detector," Med. Phys. **33**, 1053-1066 (2006).

R. K. Swank, " Absorption and noise in x-ray phosphors," J. Appl. Phys. **44**, 4199-4203 (1973).

R. K. Swank, "Measurement of absorption and noise in an x ray image intensifier, " J. Appl. Phys. **45**, 3673-3678 (1974).

W. Swindell, E. J. Morton, P. M. Evans, and D. G. Lewis, "The design of megavoltage projection imaging systems: some theoretical aspects," Med. Phys. **18**, 855-866(1991).

"Photodiode Technical Information" available from http://sales.hamamatsu.com/

G. Pang and J.A. Rowlands, "Development of high quantum efficiency flat panel detectors for portal imaging: intrinsic spatial resolution," Med. Phys. **29**, 2274-2288 (2002).

www.detectors.saint-gobain.com

Chapter 6

Summary and Future Directions

The general goal of this project is to investigate the use of segmented scintillation crystals in contact with photodiodes in MVCT for the purposes of day to day patient set-up verification and tumour imaging during fractionated radiotherapy. Accomplishment of these purposes requires that the MVCT images are obtained using low radiation dose, and are able to visualize contrast details of lower than 2% difference from the background. High density scintillation materials as the imaging detectors promise to fulfill these requirements because of the increased *DQE*. Therefore, we are working with $CdWO_4$ crystals, which are chosen for their high density, high atomic number and reasonable optical properties.

The first part of the project was the topic of the author's MSc project (Monajemi, 2004; Monajemi et al., 2004) and hence is not presented in this thesis. In the first step, the use of $CdWO_4$ and cesium iodide (CsI(Tl)) scintillation detectors was studied in MVCT. A model describing the signal acquired from a scintillation detector was developed which contains two steps: (1) the calculation of the energy deposited in the crystal due to MeV photons using the EGS*nrc* Monte Carlo code; and (2) the transport of the optical photons generated in the crystal voxels to photodiodes using the optical Monte Carlo code *DETECT2000*. The measured detector signals in single $CdWO_4$ and CsI(Tl) scintillation crystals of base 0.275 x 0.8 cm^2 and heights 0.4, 1, 1.2, 1.6 and 2 cm were, generally, in good agreement with the signals calculated with the model. A prototype detector array which contains eight $CdWO_4$ crystals each 0.275 x 0.8 x 1 cm^3 in contact with a 16-element array of photodiodes was built. The frequency dependent *MTF*, *NPS*, and *DQE* were measured for Co^{60} with beam energy of 1.25 MeV.

For 6 MV photons, only the $MTF(f)$ was measured from a linear accelerator, as large pulse-to-pulse fluctuations in the output of the linear accelerator did not allow the measurement of the $NPS(f)$ and $DQE(f)$. A two-step Monte Carlo simulation adapted from a paper written by Kausch et al. (1999) was used to model the detector's $MTF(f), NPS(f)$ and $DQE(f)$. The $DQE(0)$ of the detector array was found to be ~26% and ~19% for 1.25 MeV and 6 MV photons, respectively. The discrepancies between our modeled and measurement values were generally around 2%.

In the second part of the project, the eight element detector array was expanded to an eighty element detector. It was placed on an arc with a radius of 110 cm. A rotary stage was coupled to the detector on which a phantom can be placed and rotated. In this way a bench-top third generation CT scanner was developed. A complete description of the components of this scanner including the detector array, timing control, and multiplexer is presented in another student's MSc thesis (Tu, 2005). The detectors show a linear response to dose (dose rate was varied by changing the source to detector distance) with a correlation coefficient (R^2) nearly unity with the standard deviation of signal at each dose being less than 0.25%. The attenuation of a 6 MV beam by solid water measured by this detector array indicates a small, yet significant spectral hardening that needs to be corrected before image reconstruction. The pre-sampled *MTF* is strongly affected by the detector's large pitch and a large improvement can be obtained by reducing the detector pitch. The measured *DQE* at zero spatial frequency is 18.8 % for 6 MV photons, which will reduce the dose to the patient in MVCT applications compared with a detector with a lower *DQE*. The detector shows a less than 2% reduction in response for a large dose of 24.5 Gy accumulated in 2 hours; however, the lost response is recovered on the following day. A complete recovery can be assumed within the experimental uncertainty (standard deviation < 0.5%); however, any smaller permanent damage could not be assessed. These corresponding measurements are presented in chapter 3.

The third part of this project is presented in chapter 4 and focuses on the use of the previously developed 80 element array as a MVCT scanner. The imaging experiments were carried out mainly in a Co^{60} teletherapy unit, while the beam hardening characteristics of the system were also presented for a 6 MV beam. During image evaluation, persistent ring artifacts, caused by air gaps at the ends of the 8-element detector blocks, were removed by using a calibration procedure. The measured contrast of a low contrast target with a 20 mm diameter was determined to be independent of dose, between 2.1 and 17 cGy. The measured LCR of a target with a nominal contrast of 2.8% was reduced from 2.3% to 1.2% when the contrast target diameter was reduced from 15 mm to 5 mm, using 17 cGy dose for imaging. The SNR in the images obtained from this system is shown to be proportional to the square root of radiation dose. Most importantly, a low contrast target with a diameter of 6 mm and a nominal contrast level of 1.5% (2.1% measured) is spatially resolved with a radiation dose of 2.1 cGy in the Co^{60} beam. The spatial resolution in the Co^{60} beam is limited to 1 line pair per cm mainly due to the size of the Co^{60} source.

The ultimate goal of this project is to develop a MV area detector. The focus of chapter 5 is on using the model - that was developed in the first step of this project- to predict an optimal design for such an area detector. This part of the study uses both *x*-ray and optical photon transport Monte Carlo simulations to analyse the effects of scintillation crystal height, septa material, beam divergence and beam spectrum on the *MTF* and *DQE(0)* of a hypothetical area detector. The hypothetical detector is comprised of tall, segmented $CdWO_4$ crystals and two dimensional photodiode arrays with a pitch of 1 mm and a fill factor of 72%. Increasing the crystal height above 10 mm does not result in an improvement in the *DQE(0)* if the reflection coefficient of the septa is less than 0.8. For a reflection coefficient of 0.975 for the septa, there is a continual gain in the *DQE(0)* up to 30 mm tall crystals. Similar calculations show that employing a 3.5 MV beam without a flattening filter increases the *DQE(0)* for 20 mm tall crystals by 9% compared to a typical 6 MV beam with a flattening filter. This is the first work in which the severe degradations due to the beam divergence on *MTF(f)*

are quantified, that reinforces the suggestion made by several other investigators regarding the use of focused detectors in MV imaging. It is found that when the effect of optical photons is considered the presence of divergence can appear as a shift in the spatial location of the imaged object.

Future Directions

The final part in this project is to manufacture an area detector using segmented $CdWO_4$ crystals and 2D photodiode arrays, so that imaging more than one slice of the patient per rotation becomes feasible. Based on what we have learned from the Monte Carlo simulations in Chapter 5, such a detector will use a tall crystal in each detecting element, and the neighbouring elements will be optically isolated by using highly reflective and opaque septa material. More importantly, the detector as a whole must be focused to the x-ray source. At first glance, an active matrix flat panel imager employing a photodiode, an analog switch and a storage capacitor in each element, similar to those used in the state-of-the-art electronic portal imaging devices, may appear to be a suitable choice for MVCT, but this approach has serious limitations. Firstly, current active matrix flat panel imagers use amorphous silicon technology on a flat, rigid glass substrate. This precludes mechanical bending to obtain the curvature required to focus the tall scintillation crystals to the x-ray source. Some investigators (Sawant *et al.*, 2005, Pang and Rowlands, 2002) have suggested that the focusing can be obtained by segmenting a tall, flat sheet of crystal into individual elements with focused septa. The technology of cutting diverging septa in a thick sheet of scintillation material is not yet commercially available (Saint Gobain, personal communication). A more promising approach that may become available to the research community in the near future is the use of flexible substrate technology to grow active matrix photodiode arrays for the purpose of creating 2D focused detectors for MV imaging. The remaining important questions that need to be answered before flexible substrate technology can be used in conjunction with tall segmented scintillation detectors are the optical spectral match between the scintillator and

photodiodes and optical saturation. It should be noted that active matrix technology, due to the presence of a storage capacitor and an analog switch in each element, greatly simplifies the data acquisition electronic sub-system by sharing the gate and data lines. The general approach in passive 2D photodiode arrays is to provide signal amplification to each detector element and the amplified signals are then multiplexed. The electronic data acquisition system (DAS) for this approach is thus both more complex and expensive. Therefore, a full-size MV cone beam CT detector fabricated by tiling individual 2D photodiode arrays with appropriate septa material (to minimize optical leakage between crystals-discussed in chapter 5) and focused to the source (to minimize the adverse effects of divergence-discussed in chapter 5) would incur significant expense in a research environment. Therefore, we propose to design a multi-row, focused detector and explore the MVCBCT issues in an experimental imaging geometry. It should be noted that a single-row detector is not suitable for this investigation. The evaluation of intrinsic detector blur in 2-D requires a multi-row detector of adequate longitudinal extent to measure the blur due to Compton scattering and other factors within the detector array. Moreover, the collection of cone beam data using a single row detector would be experimentally cumbersome.

Our proposed imaging geometry is shown in figure 6.1. A 16-row detector containing 320-elements per row is arranged on an arc focused on the source at a distance of 120 cm. The objects to be imaged will be placed at a distance of 80 cm from the source and rotated by a precision rotary stage (200RT, Daedal Division, Parker Hannifin Corp, Irwin, PA and stepper motor control ZETA57-83, Compumotor Division, Parker Hannifin Corp, Rohnet Park, CA). The resulting axial scanned field of view is 21.3 cm and the z-coverage per rotation is 1.1 cm. However, the multi-row detector will be placed on its own 1-D linear stage capable of moving the entire detector array along an arc in the z-direction, see the side view of figure 6.1. The 1-D linear stage is a simple device that will move the detector array. The device will be manually operated and based on a simple move and lock in position mechanism ensuring accurate detector z-position at

discrete steps. The basic drawing for the device has been prepared in the machine shop at our facility, thus the device will be manufactured in-house. After completing a single rotation of the precision stage with the detector at the z = 0 position, the entire detector array will be translated to several different z-locations and an additional rotation of the precision stage will be used for every z-location. The source collimation will correspond to a cone-beam during the entire imaging experiment such that the image degradation due to scattered radiation from the object to detector is evaluated.

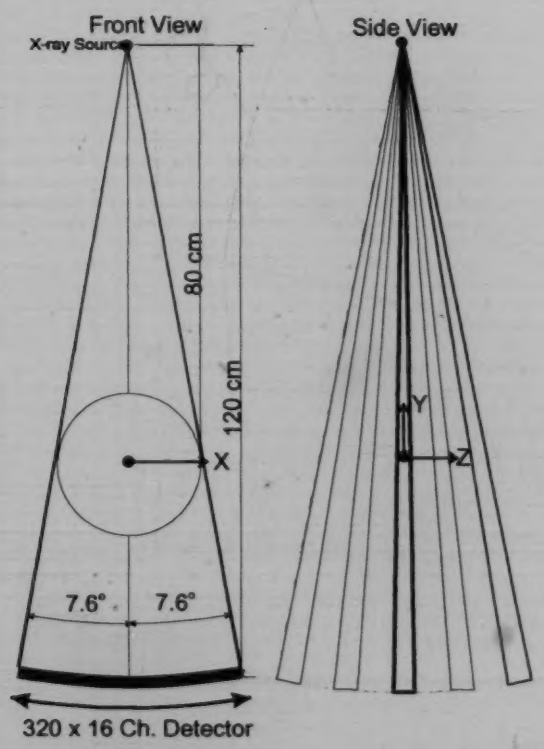

Figure 6.1: The imaging geometry for MVCBCT investigation. Side view shows the multi-row detector at z = 0 (bolded) and several other z-locations.

The fundamental building block of the detector is a back-illuminated, 2-D photodiode array tile-able in 2-D (SCA-CA256ES, Semicoa, Costa Mesa, CA). This is a 16 x 16 element array with a square pixel pitch of 1 mm and a geometric fill factor of 72%. The opto-electric specifications of this photodiode array are similar to the 16-element linear photodiode array (S5668-02, Hamamatsu, Japan) used in this thesis. Therefore, a similar or a slightly better match between the emission spectrum of $CdWO_4$ is expected with the sensitivity spectrum of the photodiodes. The $CdWO_4$ array will be constructed with a square pixel pitch of 1 mm and crystal thickness of 10 mm. The Monte Carlo simulation in the previous chapter suggested that taller crystals with highly reflective septa provide large *DQE*(0). The taller crystals are simply too expensive for this project. The 10 mm tall crystal will be adequate for the experimental validation of the some of the results of the Monte Carlo simulation. A fraction of the area of each pixel will be filled up by a reflective coating material (TiO_2 or MgO) that reduces the optical cross-talk. Semicoa has supplied 20 such building blocks, including the mounted crystal arrays, forming 320 x 16 elements that are tiled into an arc detector as shown in figure 6.2. The designed reflection coefficient of the lower density septa material is 0.97. The rest of the system hardware is depicted in block diagram in figure 6.3. Analogic Corporation has supplied the DAS for this detector. In particular, the DAS has 22 identical boards each processing 256 detector channels and a control module. In the DAS supplied by Analogic, each of the 256-channel board contains 128 DDC112 (Texas Instruments, Dallas, TX) chips. Each DDC112 chip contains four analogue signal processing channels. Each channel consists of a dual switched integrator and a 16-bit A-to-D converter. The digital data of the four channels is time-multiplexed into a single line. The time-multiplexing continues from chip-to-chip on a single converter board and then from board-to-board. The DAS produces serial data, containing time multiplexed data for all detector elements, on an optical fiber cable. The data is converted into parallel format by the Analogic DAS interface module. The parallel digital data is acquired into a host computer via two parallel input-output modules from National Instruments (NI, Austin, TX). The host computer is a cone

beam reconstruction server that provides a hardware implementation of the single orbit cone beam reconstruction algorithm (Feldkamp *et al.*, 1984). The timing and control system has been designed and synchronized with the radiation producing pulses in a manner similar to what is shown in chapter 3.. The Analogic DAS interface receives the trigger signal in response to the linac pulses after being processed by the timing and control system. It also receives the home signal from the precision rotary stage which in turn is controlled via the National Instrument board (NIPCI 6601). The Analogic DAS interface module houses programmable read only memory (PROM) that contains the firmware for the timing control mechanism of the DAS. Currently, we have two such PROM designed for lower and higher energy linacs that operate in the range of 180 Hz and 360 Hz respectively. This will allow us to perform an experiment on any linear accelerator at our facility.

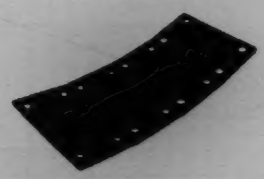

Figure 6.2: Photograph of 4 photo-diode arrays tiled together. Each photo-diode is a 16 x 16 array with a pixel pitch of 1 mm.

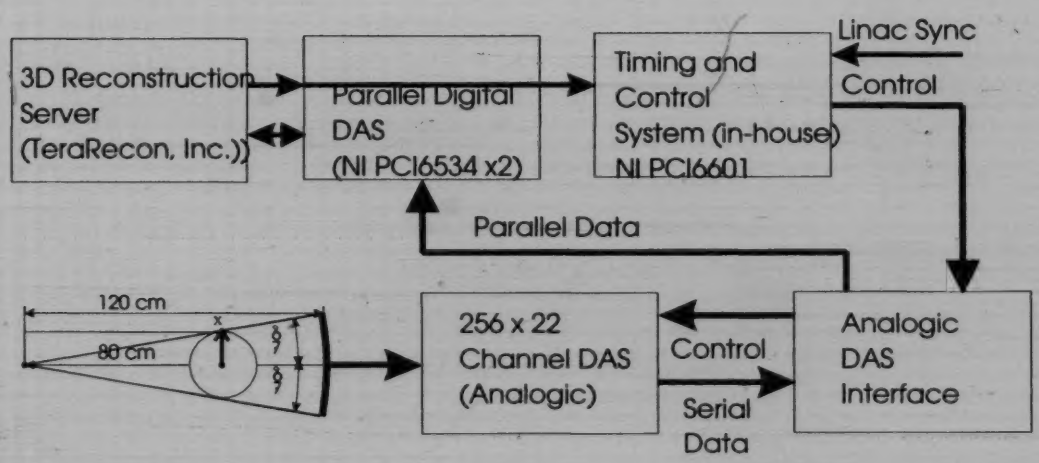

Figure 6.3: Block diagram of the proposed system of cone beam data collection and image reconstruction. The detector system and analogic DAS are inside and rest of the hardware is outside the treatment room.

All experiments will be carried out using a 6 MV photon beam from a teletherapy unit (600C, Varian Associates, Palo Alto, CA). Due to the tiling of detector blocks and z-relocation of the entire mutli-row detector in a multi-rotational scanning geometry, geometric calibration to measure the spacing between detector elements, especially the radial spacing among detector blocks, and to ensure the accuracy of the z-position of the detector, must be performed. The accurate measurement of the spacing and z-position is required to establish the fan and cone angle positions of the detector elements. A readily available radiographic film (Kodak XV) will be cut into a 32 x 4 cm^2 strip and tightly packed into a light-tight envelope. The strip containing the film will be snuggly taped at the back of the detector arc and exposed to obtain a radiograph of detector elements. The spacing between the detector blocks will be measured by digitizing and establishing the geometric calibration of the film. Since the longitudinal couch positioning accuracy of the teletherapy unit is no better than 1 mm, the scout (pilot) scan on a diagnostic CT scanner (PQ5000, Philips Medical Systems) will be used to establish the z-positioning accuracy of the linear stage. A long lead wire will be attached to the carriage of the linear stage and aligned in the transverse plane of the CT scanner using the lasers. The position of the wire in terms of the absolute longitudinal position of the couch will be measured from the scout scan. The wire will be positioned at several z-positions using the linear stage and pilot scans will be obtained at each position. The z-positions established with the linear stage will be compared with the z-positions of the wire obtained from the pilot scans. The rotational precision of the rotary stage has already been established in this thesis.

We plan to characterize the signal acquired from this detector by measuring the $MTF(f)$, $NPS(f)$ and $DQE(f)$ of the detector in a similar manner to measurements performed in chapter 3. The measured values will be compared

with the simulations performed in the previous chapter in order to further validate the calculation models. Pulse to pulse fluctuations in the output of the teletherapy unit may cause ring artifacts in the reconstructed images. The detector elements in the open part of the beam will be used to provide a correction for the pulse to pulse fluctuation in the teletherapy beam output. Spectral hardening calibration and correction will be performed. The Feldkamp algorithm (1984) of image reconstruction from cone beam projections will be used to reconstruct the images. Image reconstruction will be performed on a specialized hardware reconstruction engine [Cone Beam CT Reconstruction Server, TeraRecon, Inc.). The present implementation of the cone beam reconstruction considers the user specific geometry including the non-uniform spacing between detector elements if that happens to result from our measurements. A cylindrical detector, instead of a planar one, is also considered in the algorithm. The final part in the project will be evaluating the imaging performance of the detector by using the different CATPHAN modules as described in chapter 5.

A. References

L. A. Feldkamp, L. C. Davis and J. W. Kress, "Practical cone-beam algorithm," J. Opt. Soc. Am. A, 1,612-619, (1984).

T.T. Monajemi, *Modeling Scintillator-Photodiodes as Detectors for Megavoltage Computed Tomography*, MSc Thesis, University of Alberta (2004).

T. T. Monajemi, S. Steciw, B. G. Fallone, and S. Rathee, "Modeling scintillator-photodiodes as detectors for megavoltage CT," Med Phys. **31**, 1225-34 (2004).

G. Pang and J. A. Rowlands, "Development of high quantum efficiency flat panel detector: Intrinsic spatial resolution," Med. Phys. **29**, 2274–2285 (2002).

A. Sawant, L. E. Antonuk, Y. El-Mohri, *et al.*," Segmented crystalline scintillators: an initial investigation of high quantum efficiency detectors for megavoltage x-ray imaging." Med. Phys. **32**, 3067-83 (2005).

D. Tu, *Bench-top Megavoltage Computed Tomography Scanner with Cadmium Tungstate-Photodiode Detectors*, MSc. Thesis, University of Alberta (2005).

Bibliography

H. Alasti, M. P. Petric, C. N. Catton and P.R. Warde, "Portal imaging for evaluation of daily on-line setup errors and off-line organ motion during conformal irradiation of carcinoma of the prostate," Int. J. Radiat. Oncol. Biol. Phys. **49**, 869–884 (2001).....6

L. E. Antonuk, "Electronic portal imaging devices: a review and historical perspective of contemporary technologies and research," Phys. Med. Biol. **47**, R31-65 (2002).....4,5,12

J. M. Balter, G. T. Chen, C. A. Pelizzari, *et al.*, "Online repositioning during treatment of the prostate: A study of potential limits and gains," Int. J. Radiat. Oncol. Biol. Phys. **27**,137–143 (1993).....6

J. M. Balter, R.K. Ten Haken, T. S. Lawrence, *et al.*, "Uncertainties in CT-based radiation therapy treatment planning associated with patient breathing," Int. J. Radiat. Oncol. biol. Phys. **36**, 167-174 (1996).....4

H. H. Barrett, S. K. Gordon and R. S. Hershel, "Statistical limitations in transaxial tomography," Comput. Biol. Med. **6**, 307-323 (1976).....109

P. Bergstrom, P. O. Lofroth and A. Widmark, "High-precision conformal radiotherapy (HPCRT) of prostate cancer—a new technique for exact positioning of the prostate at the time of treatment," Int. J. Radiat. Oncol. Biol. Phys. **42**, 305–311 (1998).....6

A. Berndt, S. Rathee, D. W. Rickey and J. Bews, "An 8-channel Detector for an ^{192}Ir brachytherapy source-based computed tomograhpy scanner", IEEE Trans. Nucl. Sc. **47**, 1261-1267 (2000).....47

J. T. Bushberg, J. A. Seibert, E. M. Leidholdt and J. M. Boone, *The Essential Physics of Medical Imaging*, (Lippincott Williams & Wilkins, Philadelphia, 2002).....13

M. P. Carol, " Peacock™: a system for planning and rotational delivery of intensity modulated fields," Int. J. Img. Sys. Tech. **6**, 56-61 (1995).....3

M. Chirila, *The influence of point defects on the optical properties of cadmium tungstate*, West Virginia University, MSc thesis (2000).....28,29

C. Constantinou, J. C. Harrington and L. A. DeWerd, "An electron density calibration phantom for CT-based treatment planning computers," Med. Phys. **19**, 325-327 (1992).....8

I. A. Cunningham, "Applied Linear Systems Theory", *in Handbook of Medical*

Imaging, edited by R. L. Van Metter (SPIE, Bellingham, WA, 2000) Ch. 2.....52-54

J. C. Dainty, and R. Shaw, *Image Science,* Academic Press, 1974.....62-65

L. A. Dawson, D. W. Litzenberg, K. K. Brock, *et al.*, " A comparison of ventilatory prostate movement in four treatment position," Int. J. Radiat. Oncol. Biol. Phys. **48**, 319-323 (2000).....4

W. DeNeve, C. DeWagter, K. DeJaeger, *et al.* "Planning and delivering high doses to targets surrounding the spinal cord at the lower neck and upper mediastinal levels: static beam segmentation technique executed with a multileaf collimator," Radiother. and Oncol. **40**, 271–279 (1996).....3

S. E. Derenzo, M. J. Weber, W. E. Bourret-Courchesne and M. K. Klintenberg, "The quest for the ideal inorganic scintillator," Nuclear Instruments and Methods in Physics Research Section A: Accelerators, Spectrometers, Detectors and Associated Equipment, **505**, 111-117 (2003).....26

A. Eisbruch A, L. H. Marsh, M. K. Martel, *et al.* "Comprehensive irradiation of head and neck cancer using conformal multi segmental fields: Assessment of target coverage and noninvolved tissue sparing," Int. J. Radiat. Oncol. Biol. Phys. **41**, 559–568 (1998).....3

M. Endo, T. Tsunoo, N. Nakamori, and K. Yoshida, "Effect of scattered radiation on image noise in cone beam CT," Med. Phys. **28**, 469-474 (2001).....8

E. C. Ford, J. Chang, K. Mueller, *et al.*, "Cone-beam CT with megavoltage beams and an amorphous silicon electronic portal imaging device: Potential for verification of radiotherapy of lung cancer," Med. Phy. **29**, 2913-2924 (2002).....1,8,11

H. Fujita, K. Ueda, J. Morishita, *et al.*, "Basic imaging properties of a computed radiographic system with photostimulable phosphors," Med. Phys. **16** , 52-59 (1989).....5

H. Fujita, D. Y. Tsai, T. Itoh, *et al.*, "A simple method for determining the modulation transfer function in digital radiography," IEEE Trans. on Medical Imaging **11**, 34-39 (1992).....59, 61, 69, 129, 134

M. Goitein, M. Abrams, D. Rowell, *et al.*, "Multidimensional treatment planning: II. Beam's-eye-view, back projection, and projection through CT sections," Int. J. Radiat. Oncol. Biol.Phys. **9**, 789–797 (1983).....6

B. A. Groh, J. H. Siewerdson, D. G. Drke, *et al.*, "A performance comparison of flat-panel imager-based MV and kV cone-beam CT," Med. Phys. **29**, 967-975 (2002).....8, 11, 12

H. Guan and Y. Zhu, "Feasibility of megavoltage portal CT using an electron portal imaging device (EPID) and multi-level scheme algebraic reconstruction technique (MLS-ART)," Phys. Med. Biol. **43**, 2925-2937 (1998).....1, 8, 11

M. G. Herman, J. M. Balter, D. A. Jaffray, *et al.*, "Clinical use of electronic portal imaging: Report of AAPM radiation therapy committee task group 58," med. Phys. **28**, 712- 737 (2001).....12

B. M. Hesse, L. Spies, and B. A. Groh, "Tomotherapeutic portal imaging for radiation treatment verification," Phys. Med. Biol. **43**, 3607-3616 (1998).....8, 10

D. C. Hornick, D. W. Litzenberg, K. L. Kam, *et al.*, "A tilt and roll device for automated correction of rotational setup errors," Med. Phys. **25**, 1739–1740 (1998).....6

T.S. Hong, W. A. Tome, R. J. Champell, *et al.*, "The impact of daily setup variations on head-and-neck intensity-modulated radiation therapy," Int. J. Radiat. Oncol. Biol. Phys. **61**, 779-788(2005).....3

J. Hsieh, *Computed Tomography: Principles, Design, Artifacts, and Recent Advances* ,SPIE Press, 2003.....93

ICRU, "Specification of high-activity gamma-ray sources," ICRU Report 18, ICRU, Washington, D.C. (1971).....104

M. Ishii and M. Kobayashi, "Single crystals for radiation detectors," Prog. Crystal Growth and Charact. Mater. **23**, 245-311 (1991).....24, 28, 36, 37

D. A. Jaffray, J. H. Siewerdsen, J. W. Wong, and A. A. Martinez, "Flat panel cone-beam computed tomography for image guided radiation therapy," Int. J. Radiat. Oncol. Biol. Phys. **53**, 1337-1349 (2002).....7

D. A. Jaffray, J. J. Battista, A. Fenster, and P. Munro, " Monte Carlo studies of x ray energy absorption and quantum noise in megavoltage transmission radiography," Med. Phys. **22**, 1077-1088 (1995).....129

H. E. Johns and J. R. Cunningham, *The Physics of Radiology*, 4th ed. (Thomas, Springfield, IL, 1983).....30-32, 34

P. M. Joseph and R. D. Spital, "A method for correcting bone induced artifacts in computed tomography scanners," J. Comput. Assist. Tomogr. **2**, 100-108, (1978).....104

A. C. Kak and M. Slaney, *Principles of Computerized Tomographic Imaging*, Society of Industrial and Applied Mathematics, 2001.....98, 100

I. Kawrakow and D.W.O. Rogers, "The EGSnrc code system: Monte Carlo simulation of electron and photon transport," NRCC Report PIRS-701 (2002).....34, 71, 132

H. Keller, M. Glass, R. Hinderer, *et al.*, "Monte Carlo study of a highly efficient gas ionization detector for megavoltage imaging and image-guided radiotherapy," Med. Phys. **29**, 165-175 (2002).....13, 76, 86

D. R. Kinloch, W. Novak, P. Raby, and I. Toepke, "New developments in Cadmium Tungstate", IEEE Trans. Nucl. Sci., **41**, 752-754 (1994).....37-39, 125, 127, 134, 135, 138

F. M. Khan, *The physics of radiation therapy*, Lippincott Williams & Wilkins, third edition, 2003.....30, 31, 34

M. Kobayashi, M. Ishii, Y. Usuki and H. Yahagi, "Cadmium tungstate scintillators with excellent radiation hardness and low background", Nucl. Instrum. Meth. Phys. Reasearch. A **349**, 407-411, (1994).....38, 77, 78, 84, 88

P. Kozma, R. Bajgar, and P. Kozma Jr., "Radiation resistivity of large tungstate crystals", Rad. Phys. Chem., **59**, 377-380, (2000).....38, 77, 84

G. F. Knoll, *Radiation detection and measurement*, Willey, second edition, 1989.....24, 25, 27

G. F. Knoll, T. F. Knoll, and T. M. Henderson, "Light collection in scintillation detector composites for neutron detection," IEEE Trans. Nucl. Sci. **35**, 872-875 (1988).....132, 133, 135

F. A. Kroger , *Some Aspects of the Luminescence of Solids*, Elsevier Publ. Co., Amsterdam,1948.....28

D. J. Krus, W. P. Novak, L. Perna, "Precision linear and two-dimensional crystal arrays for x-ray and gamma-ray imaging applications," Proc. SPIE **3768**, 183-194 (1999).....136

K. Kuriyama, H. Onishi, N. Sano, T. Komiyama, *et al.*, "A new irradiation unit constructed of self-moving gantry-CT and linac," Int. J. Radiat. Oncol. Biol. Phys. **55**, 428-435 (2003).....7

L. C. Kwan, J. M. Boone, and N. Shah, "Evaluation of x-ray scatter properties in a dedicated cone-beam breast CT scanner," Med. Phys. **32**, 2967-2975 (2005).....8

M. Lachaîne and B. G. Fallone, "Monte Carlo detective quantum efficiency and scatter studies of a metal/a-Se portal detector," Med. Phys. **25**, 1186-1194 (1998).....158

M. Lachaine, E. Fourkal and B.G. Fallone, "Detective quantum efficiency of a direct-detection active matrix flat panel imager at megavoltage energies," Med. Phys. **28**, 1364-1372 (2001).....72, 75, 76

M. J. J. Lammers, G. Blasse and D. S. Robertson, "The luminescence of cadmium tungstate," Phys. Stat. Sol. A- Appl. Research **63**, 569-572 (1981).....28

A. J. Lattanzi, S. McNeeley, W. Pinover, *et al.*, "A comparison of daily CT localization to a daily ultrasound-based system in prostate cancer," Int. J. Radiat. Oncol. Biol. Phys. **43**, 719–725 (1999).....7

A. Levin and C. Moisan, "A more physical approach to model the surface treatment of scintillation counters and its implementation into DETECT," IEEE Trans. Nucl. Sci. Symposium of Anaheim, 702-706 (1996).....14, 132, 133, 135

D. G. Lewis, W. Swindell, E. J. Morton, *et al.*, "A megavoltage CT scanner for radiotherapy verification," Phys. Med. Biol. **37**, 1985-1999 (1992).....8, 10, 92, 105

T. R. Mackie, T. Holmes, S. Swerdloff, *et al.*, "Tomotherapy: a new concept for the delivery of dynamic conformal radiotherapy," Med. Phys. **20**, 1709-1719 (1993).....3

T. R. Mackie, J. Kapatoes, K. Ruchala , *et al.*," Image guidance for precise conformal radiotherapy," Int. J. Radiat. Oncol. Biol. Phys. **56**, 89-105 (2003).....7

S. Midgley, R. M. Miller, and J. Dudson, "A feasibility study for megavoltage cone beam CT using a commercial EPID," Phys. Med. Biol. **43**, 155-169 (1998).....10

T.T. Monajemi, *Modeling Scintillator-Photodiodes as Detectors for Megavoltage Computed Tomography*, MSc Thesis, University of Alberta (2004).....70, 72, 73, 84, 86, 89, 124, 167

T. T. Monajemi, S. Steciw, B. G. Fallone, and S. Rathee, "Modeling scintillator-photodiodes as detectors for megavoltage CT," Med Phys. **31**, 1225-1234 (2004).....13, 14, 36, 46, 47, 70, 72, 73, 84, 86, 89, 136, 167
T.T. Monajemi, D. Tu, S. Rathee and B.G. Fallone, "A bench-top megavoltage fan-beam CT using $CdWO_4$-photodiode detectors: II- Image performance evaluation," Med. Phys. **33**, 1090-1100 (2006).....1, 124

M. Montecchi and Q. Ingram, "Study of some optical glues for the Compact Muon Solenoid at the large hadron collider of CERN", Nucl. Instrum. Meth. in Phys Res. A **465**, 329-345 (2001).....135

O. Morin, A. Gillis, J. Chen, *et al.*, "Megavoltage cone-beam CT: system description and clinical applications," Med. Dosim. **31**, 51-61 (2006).....8, 11

D. J. Morell, J. S. Cantrell., and L.L. Y. Chang, "Phase-relations and crystal structure of Zn and Cd tungstates," J. American Ceramic Society **63**, 261-264 (1980).....28

E.J. Morton, W. Swindell, D.G. Lewis, and P. M. Evans," A linear array, scintillation crystal-photodiode detector for megavoltage imaging," Med. Phys. **18**, 681-691 (1991).....1

M. A. Mosleh-Shirazi, P. M. Evans, W. Swindell, *et al.*, "A cone-beam megavoltage CT scanner for treatment verification in conformal radiotherapy," Radiotherapy and Oncology **48**, 319-328 (1998).....1, 8

M. A. Mosleh-Shirazi, W. Swindell, and P. M. Evans, "Optimization of the scintillation detector in a combined 3D megavoltage CT scanner and portal imager," Med. Phys. **25**, 1880-1890 (1998).....126

J. Moy, "Signal-to-noise ratio and spatial resolution in x-ray electronic imagers: is the MTF a relevant parameter?" Med. Phys. **27**, 86-93 (2000).....87, 88

C. D. Mubata, A. M. Bidmead, L. M. Ellingham, *et al.*, "Portal imaging protocol for radical dose-escalated radiotherapy treatment of prostate cancer," Int. J. Radiat. Oncol. Biol. Phys. **40**, 221–231 (1998).....6

P. Munro, J. A. Rawlinson and A. Fenster, "Therapy imaging: source sizes of radiotherapy beam," Med. Phys. **15**, 517-524 (1988).....12, 87, 141

P. Munro and D. C. Bouius, "X-ray quantum limited portal imaging using amorphous silicon flat-panel arrays," Med. Phys. **25**, 689–702 (1998).....6

P. Munro, "Megavoltage radiation for treatment verification", in *The Modern Technology of Radiation Oncology* , edited by Van Dyke J. (Medical Physics Publishing, Madison, WI, 1999), 481-508.....5

K. Nakagawa, Y. Aoki, A Akanuma, *et al.*, "Technical features and clinical feasibility of megavoltage CT scanning", Euro. Radiol. **2**, 184-189 (1992).....1, 8, 10

R. Ning, X. Tang, and D. Conover, "X-ray scatter correction algorithm for cone beam CT imaging," Med. Phys. **31**, 1195-1202 (2004).....5

G. H. Olivera, D. M. Shepard, K. Ruchala, *et al.*, "Tomotherapy", in *The Modern Technology of Radiation Oncology* , edited by Van Dyke J. (Medical Physics Publishing, Madison, WI, 1999), 521-588.....3

O.Z Ostapiak, P. F. O'Brien and B. A. Faddegon, "Megavoltage imaging with low Z targets: implementation and characterization of an inverstigational system," Med. Phys. **25**, 1910-1918 (1998).....14

M. Partridge, P. M. Evans, and M. A. Mosleh-Shirazi, "Linear accelerator output variations and their consequences for megavoltage imaging," Med. Phys. **25**, 1443-1452 (1998).....98

M. Partridge, M Ebert, and B-M. Hesse, "IMRT verification by three-dimensional dose reconstruction from portal beam measurements," Med. Phys. **29**, 1847-1858 (2002).....8

G. Pang G, D. J. Beachey, P. F. O'Brien, *et al.*, "Imaging of 1.0-mm-diameter radio-opaque markers with megavoltage x-rays: An improved online imaging system," Int. J. Radiat. Oncol. Biol. Phys. **52**, 532–537 (2002).....6

G. Pang and J. A. Rowlands, "Development of high quantum efficiency flat panel detector: Intrinsic spatial resolution," Med. Phys. **29**, 2274–2285 (2002).....13, 88, 127, 140, 170

G. Pang and J. A. Rowlands, "Development of high quantum efficiency, flat panel, thick detectors for megavoltage x-ray imaging: A novel direct-conversion design and its feasibility," Med. Phys. **31**, 3004-3016 (2004).....13, 88

A. Pirzkall, M. Carol, F. Lohr , *et al.*, "Comparison of intensity modulated radiotherapy with conventional conformal radiotherapy for complex shaped tumours," Int. J. Radiat. Oncol. Biol. Phys. **48**, 1371-1380 (2000).....2

J. Pouliot, A. Bani-Hashemi, J. Chen, *et al.*, "Low dose megavoltage cone beam CT for radiotherapy", Int. J. Radiat. Oncol. Biol. Phys. **61**, 552-560 (2005).....8, 11, 14, 103

S. Rathee, D. Tu, T.T. Monajemi, *et al.*, "A bench-top megavoltage fan-beam CT using $CdWO_4$-photodiode detectors: I- System description and detector characterization," Med. Phys. **33**, 1078-1089 (2006).....124

P. Remeijer, E. Geerlof, L. Ploeger, *et al.*, "3-D portal image analysis in clinical practice: An evaluation of 2-D and 3-D analysis techniques as applied to 30 prostate cancer patients," Int. J. Radiat. Oncol. Biol. Phys. **46**, 1281–1290 (2000).....6

E. Rietzel, S. J. Rosenthal, D. P. Gierga, et al., "Moving targets: detection and tracking of internal organ motion for treatment planning and patient setup," Radiother. Oncol. **73** Suppl 2:S68-72 (2004).....4

G. Rizzoni, *Principles and Applications of Electrical Engineering*, 3rd Ed. (McGraw-Hill, 2000).....41

D. W. O. Rogers, B. A. Faddegon, G. X. Ding, *et al.*, "BEAM: A Monte Carlo code to simulate radiotherapy treatment units," Med. Phys. **22**, 503–524 (1995).....139

D. W. O. Rogers, "Fluence to dose equivalent conversion factors calculated with EGS3 for electrons from 100 keV to 20 GeV and photons from 11 keV and 20 GeV," Health Phys. **46**, 891-914 (1984).....76, 77

J. A. Rowlands, "The physics of computed radiography," Physics in Medicine and Biology **47**, R123-R166 (2002).....5

K. J. Ruchala, G. H. Olivera, E. A. Schloesser and T. R. Mackie, "Megavoltage CT on a tomotherapy system," Phys. Med. Biol. **44**, 2597-2621 (1999).....1, 8, 10, 12, 116

K. J. Ruchala, G. H. Olivera, E. A. Schloesser, *et al.*, "Calibration of tomotherapeutic MVCT system," Phys. Med. Biol. **45**, N27-N36 (2000).....8, 12

A. Sawant, L.E. Antonuk, Y. El-Mohri, *et al.*, "Segmented phosphors: MEMS-based high quantum efficiency detectors for megavoltage x-ray imaging," Med. Phys. **32**, 553-565 (2005).....13, 126

A. Sawant, L. E. Antonuk, Y. El-Mohri, *et al.*," Segmented crystalline scintillators: An initial investigation of high quantum efficiency detectors for megavoltage x-ray imaging." Med. Phys. **32**, 3067-83 (2005).....
.....13, 58, 88, 126, 127, 129, 140, 144,160

A. Sawant, L. E. Antonuk, Y. El-Mohri, *et al.*, "Segmented crystalline scintillators: Empirical and theoretical investigation of a high quantum efficiency EPID based on initial engineering prototype CsI(Tl) detector," Med. Phys. **33**, 1053-1066 (2006).....13, 160

E. J. Seppi, P. Munro, S. W. Johnsen, *et al.*,"Megavoltage cone-beam computed tomography using a high-efficiency image receptor," Int. J. Radiat. Oncol. Biol. Phys. **55**, 793-803 (2003).....1, 8, 11, 92, 107, 116

G. Sherouse, K. L. Novins, E. L. Chaney, "Computation of digitally reconstructed radiographs for use in radiotherapy treatment design," Int. J. Radiat. Oncol. Biol. Phys.**18**, 651–658 (1990).....6

C. Schroeder, T. Stanescu, S. Rathee, B. G. Fallone, "Lag measurement in a-Se active matrix flat panel imager," Med. Phys. **31**, 1203-1209 (2004).....88

L. A. Shepp and B. F. Logan, "The Fourier reconstruction of a head section," IEEE Trans. Nucl. Sci. **21**, 21-43 (1974).....100, 101

R. G. Simpson, C. T. Chen, E. A. Grubbs, and W. Swindell, "A 4-MV CT scanner for radiation therapy: The prototype system," Med. Phys. **9**, 574-579 (1982).....1, 8, 9, 92

R. A. C. Siochi, "Minimizing static intensity modulation delivery time using an intensity solid paradigm," Int. J. Radiat. Oncol. Biol. Phys. **43**,671– 679 (1999)...3

J. H. Siewerdsen and D. A. Jaffray, "Optimization of x-ray imaging geometry (with specific application to flat-panel cone-beam computed tomography)," Med. Phys. **27**, 1093-1914 (2000).....87

J. H. Siewerdsen and D. A. Jaffray, "A ghost story: spatio-temporal response characteristics of an indirect-detection flat panel imager," Med. Phys. **26**, 1624-1641 (1999).....88

J. H. Siewerdsen and D. A. Jaffray, "Cone-beam computed tomography with a flat panel imager: Effect of image lag," Med. Phys. **26**, 2635-2647 (1999).....88

J. Sonke, L. Zijb, P. Remeijer, and M. Van Herk, "Respitory correlated cone beam CT," Med. Phys. **32**, 1176-1186 (2005).....8

M. Sonoda, M. Takano, J. Miyahara, and H. Kato, "Computed radiography utilizing scanning laser stimulated luminescence," Radiology **148**, 833-838 (1983).....5

S. V. Spirou and C. S. Chui, "A gradient inverse planning algorithm with dose-volume constraints," Med. Phys. **25**, 321-333 (1998).....3

J. Stein, T. Bortfeld, B. Dorschel, *et al.*,"Dynamic X-ray compensation for conformal radiotherapy by means of multi-leaf collimation," Radiother. Oncol. **32**,163–173 (1994).....3

J. C. Stroom, M. J. J. Olofsen-van Acht, S. Quint, *et al.*,"On-line setup corrections during radiotherapy of patients with gynecologic tumors," Int. J. Radiat. Oncol. Biol. Phys. **46**, 499–506 (2000).....6

H. D. Suit, "Local control and patient survival," Int. J. Radiat. Oncol. Biol. Phys. **23**, 653– 660 (1992).....2

W. Swindell, E. J. Morton, P. M. Evans, and D. G. Lewis, "The design of megavoltage projection imaging systems: some theoretical aspects," Med. Phys. **18**, 855-866(1991).....131

W. Swindell, R. G. Simpson, and J. R. Oleson, *et al.*, "Computed Tomography with a linear accelerator with radiotherapy applications," Med. Phys. **10**, 416-420 (1983).....8, 10

R. K. Swank, "Absorption and noise in x-ray phosphors", J. Appl. Phys., **44**, 4199-4203, (1973).....77, 129

R. K. Swank, "Measurement of absorption and noise in an x ray image intensifier, " J. Appl. Phys. **45**, 3673-3678 (1974).....129

D. Tu, *Bench-top Megavoltage Computed Tomography Scanner with Cadmium Tungstate-Photodiode Detectors*, MSc. Thesis, University of Alberta (2005).....1, 15, 168

J. Van de Steene, F. Van den Heuvel, A. Bel, *et al.*, "Electronic portal imaging with on-line correction of setup error in thoracic irradiation: Clinical evaluation," Int. J. Radiat. Oncol. Biol. Phys. **40**, 967–976 (1998).....6

Van den Heuvel, T. Powell, E. Seppi, *et al.*, "Independent verification of ultrasound based image-guided radiation treatment, using electronic portal imaging and implanted gold markers," Med. Phys. **30**, 2878-2887 (2003).....7

E. Vigneault, J. Pouliot, J. Laverdiere, *et al.*, "Electronic portal imaging device detection of radio-opaque markers for the evaluation of prostate position during megavoltage irradiation—a clinical study," Int. J. Radiat. Oncol. Biol. Phys. **37**, 205–212 (1997).....6

M. B. Williams, P. A. Mangiafico, and P. U. Simoni, "Noise power spectra of images from digital mammography detectors", Med. Phys. **26**, 1279-1293 (1999).....63-67, 73, 74

http://sales.hamamatsu.com/; "Photodiode Technical Information."..... .....43, 48, 135, 173

www.detectors.saint-gobain.com; "Scintillator Information".....36, 38, 85

www.nist.gov/ PhysRefData; "The national instate of standards and technology website".....31, 32

L. Xing, Z. Lin, S. S. Donaldson, *et al.*, "Dosimetric effects of patient displacement and collimator and gantry angle misalignment on intensity modulated radiation therapy," Radiation Oncol. **56**, 97-108 (2000).....3

M. Yazdia, L. Gingras and L. Beaulieu, "An adaptive approach to metal artifact reduction in helical computer tomography for radiation treatment planning:experimental and clinical studies", Int. J. Rad. Onc. Biol. Phys. **62**, 1224-1231 (2005).....8

W. Zhao, C. DeCrescenzo, and J. A. Rowlands, "Investigation of lag and ghosting in amorphous selenium flat-panel x-ray detector", Proc. SPIE 4682, 9-20 (2002).....88

R-y Zhu, D-a Ma and H. Newman, "Scintillating Crystals in a Radiation environment," Nuclear physics B(Proc. Supp) **44**, 547-556 (1995).....38